UNIVERSITY OF SOUTHAMPTON

FACULTY OF ENGINEERING, SCIENCE AND MATHEMATICS

Optoelectronics Research Centre

Polarization Sensitive Ultrafast Laser Material Processing

by

Jingyu Zhang

Thesis for the degree of Doctor of Philosophy

2016

UNIVERSITY OF SOUTHAMPTON

ABSTRACT

FACULTY OF ENGINEERING, SCIENCE AND MATHEMATICS

Optoelectronics Research Centre

Thesis for the degree of Doctor of Philosophy

POLARIZATION SENSITIVE ULTRAFAST LASER MATERIAL PROCESSING

Jingyu Zhang

In this thesis, I will concentrate on ultrafast laser interactions with various materials such as fused silica, crystalline silicon, amorphous silicon and nonlinear crystal.

The first polarization sensitive ultrafast laser material interaction to be illustrated was second harmonic generation in lithium niobate by tightly focused cylindrical vector beams. The generated second harmonic patterns were experimentally demonstrated and theoretically explained. Existence of the longitudinal component of the fundamental light field was proven. The same beams were used for modifying fused silica glass. Distribution of the electric field in the focal region was visualized by the presence of self-assembled nanogratings. Also in this experiment, crystalline and amorphous silicon were modified by the focused cylindrical vector beams. The generated modifications matched well with the theoretical simulations.

Polarization dependent structure was not observed under single pulse irradiation above the silicon surface. The generated isotropic crater structures with their smooth surface can be implemented as a wavefront sensor. Unexpectedly, an entirely different modification was observed after the double pulse laser irradiation. The size and orientation of the structure can be independently manipulated by the energy of the first pulse and polarization of the second pulse.

Theoretical analysis was conducted and the formation mechanism of the polarization dependent structures was explained. This structure on silicon surface can be used for the polarization-multiplexed optical memory.

One type of polarization sensitive ultrafast laser modification in fused silica is nanogratings. This modification exhibits form birefringence and therefore can be implemented for multi-dimensional optical data storage. Optimized data recording parameters were determined by sets of experiments. Stress-induced birefringence was observed and explained by material expansion at different conditions.

Finally, the multilevel encoding of polarization and intensity states of light with self-assembled nanostructures was illustrated. A new writing setup was designed and involved a spatial light modulator, a half-wave plate matrix and a 4F optical system. The data recording rate was increased by 2 orders of magnitude compared to conventional laser direct writing setup using polarization optics. The recording and readout of digital information was experimental demonstrated. We successfully recorded across three layers a digital copy of a 310KB file. The benefits of 5D optical data storage, such as long lifetime and high capacity were illustrated. In addition, the theoretical limitations of the current writing system and readout system were discussed and several upgraded systems were proposed.

Table of Contents

List of tables

List of figures

DECLARATION OF AUTHORSHIP

I, Jingyu Zhang, declare that this thesis and the work presented in it are my own and has been generated by me as the result of my own original research.

Polarization sensitive optical elements by ultrafast laser nanostructuring of glass

I confirm that:

1. This work was done wholly or mainly while in candidature for a research degree at this University;
2. Where any part of this thesis has previously been submitted for a degree or any other qualification at this University or any other institution, this has been clearly stated;
3. Where I have consulted the published work of others, this is always clearly attributed;
4. Where I have quoted from the work of others, the source is always given. With the exception of such quotations, this thesis is entirely my own work;
5. I have acknowledged all main sources of help;
6. Where the thesis is based on work done by myself jointly with others, I have made clear exactly what was done by others and what I have contributed myself;
7. Parts of this work have been published as:

R. Drevinskas, **J. Zhang**, M. Beresna, M. Gecevičius, A. G. Kazanskii, Y.P. Svirko, P. G. Kazansky
Laser Material Processing with Tightly Focused Cylindrical Vector Beams
Applied Physics Letters, 108 (22), 221107, (2016)

J. Zhang, R. Drevinskas, M. Beresna, P. G. Kazansky
Polarization sensitive anisotropic structuring of silicon by ultrashort light pulses
Applied Physics Letters, 107 (4), 041114, (2015)

J. Zhang, M. Gecevičius, M. Beresna, P. G. Kazansky
Seemingly unlimited lifetime data storage in nanostructured glass
Physical review letters, 112 (3), 033901,(2014)

Signed:.....

Date:.....

Acknowledgements

I would like to express my gratitude to the numerous individuals whose help and support assisted my professional growth during my recent years.

Firstly, I want to thank to my PhD supervisor Peter Kazansky for leading my doctoral project and attracting great public and academic attention to my research work.

I acknowledge all the help and support from our research group members, Costa, Martynas, Mindaugas, Rokas, Aabid and Ausra. Especially I want to thank to Rokas for the help he brought in times of trouble.

I am grateful to my wife Hanwei Zhou who pushed me so hard to write my thesis. It is hard to imagine having made it to this point without her. I would like to thank my parents for their support and understanding.

My last gratefulness belongs to the Engineering and Physical Sciences Research Council (EPSRC) who gave me the chance to study in the ORC by supporting my PhD financially.

Definitions and Abbreviations

λ	Wavelength of light
AFM	Atomic force microscopy
AWFFT-IA	Adaptive weighted FFT-based iterative algorithm
BPF	Band-pass filter
BS	Beam splitters
CCD	Coupled charge device
DL	Delay line
E	Electric field
EASLM	Electrically addressed spatial light modulator
FDTD	Finite difference time-domain
FFT	Fast Fourier transform
FL	Fourier lens
FSL	Femtosecond laser
GSW	Weighted Gerchberg-Saxton Algorithm
GSW-DIA	Weighted Gerchberg Saxton double iterative algorithm
HDD	Hard disc drive
HPM	Half-wave plate matrix
IFFT	Fast inverse Fourier transform
LC	Liquid crystal
LIPSS	Laser-induced periodic surface structure
NA	Numerical aperture

PM	Phase mask
PMMA	Polymethyl methacrylate
RMSE	Root-mean-square error
SEM	Scanning electron microscope
SH	Second harmonic
SHG	Second harmonic generation
SLM	Spatial light modulator
SPIN	Super-resolution photoinduction-inhibition nanolithography
SSD	Solid-state drives
VC	Visual C++
WIO	Water immersion objective

Chapter 1: Introduction

1.1 Motivation and aims

Since the invention of the laser in 1960 [1], it has attracted significant interest due to its wide range of applications in science, medicine and industry such as spectroscopy, laser surgery and laser cutting. Differing from other sources of light, laser emits light coherently, which means the light could be focused to a tight spot with unprecedented intensities. Therefore, the laser is widely applied for contactless material processing.

The ultrashort laser was firstly demonstrated in the early 1970s, but lacked power and stability. The evolution of the ultrashort laser took place in the 1990s when Kerr-lens mode locking [2] and semiconductor saturable absorber mirrors [3] were invented. After that, the ultrashort laser system was broadly adopted in micro-machining [4], femtochemistry [5], fluorescence microscope [6], laser surgery [7], and terahertz radiation [8].

There is a rapidly growing interest to material processing with ultrashort lasers. Tightly focused ultrashort laser pulses can produce localized structural change with the precision of tens of nanometers. The femtosecond laser processing in the bulk of transparent materials was first demonstrated by K. Davis *et al.* [4]. In their experiments, permanent refractive-index increase after laser irradiation was observed in the fused silica.

A new laser induced modification known as nanogratings was discovered also in fused silica in a regime with higher pulse energies in 2003 [9]. Since then, many groups tried to investigate its properties and attempted to explain its formation mechanism. However, there is still no complete explanation. The self-assembled nanostructure behaves as a uniaxial optical crystal with negative birefringence. The phase retardance and azimuth of the slow axis of the form birefringent modification can be independently manipulated by the intensity and polarization of the incident beam. Therefore, numerous applications based on laser-induced birefringence in fused silica can be created.

In this thesis, I will show polarization sensitive ultrafast laser material processing and high density optical data storage by femtosecond laser induced modifications. Many experimental results such as focused cylindrical vector beams, polarization and intensity dependent structures on silicon and eventually 5D optical data storage based on nanogratings will be discussed.

1.2 Thesis overview

Chapter 2:

In this chapter, the experimental setup and analysis tools for the ultrafast laser material processing are described. The working principle of CRi Abrio birefringence measurement system is explained.

Chapter 3:

The Fourier transform and Fourier propagation are introduced. The weighted Gerchberg-Saxton algorithm and its adapted algorithm for computer generated hologram are illustrated. The adapted algorithm can be implemented for 5D optical data storage.

Chapter 4:

A radially polarized field can be focused to spot size much smaller than for linearly polarized. Therefore, it can be implemented for high density optical data storage application. S-waveplate and electrically addressed spatial light modulator (EASLM) are applied for generating cylindrical vector beams with annular shaped intensity distribution. Strong longitudinal electric field can be obtained by tightly focusing a radially polarized beam with such intensity distribution. The existence of the longitudinal electric field in the focal volume is verified by set of experiments in the z-cut lithium niobate crystal and fused silica. However, the experiments on a-Si:H film and crystalline silicon indicate that the refractive index mismatch at the interface can strongly affect the light field that oscillates perpendicular to the surface.

Chapter 5:

A polarization sensitive structuring on a silicon surface by the linearly polarized femtosecond double pulses is experimentally demonstrated. The distribution of electric near-field becomes asymmetric and polarization dependent when the second pulse propagates through a circular crater structure produced by the first pulse. The formation of such structure is speculated to be caused by surface-wave modes and the field coupling to the waveguided modes of the

aperture. The wavelength-sized polarization sensitive structures on silicon surface may find applications for the polarization-multiplexed optical memory.

Chapter 6:

The principal of femtosecond laser induced modification in transparent material is introduced. The formation mechanism and properties of nanogratings are illustrated. Influence on modification on laser fabrication parameters such as objective lens, laser power, number of pulses and pulse duration is investigated. The optimized laser writing parameters for 5D optical data storage recording are obtained. Stress-induced birefringence is observed during the experiment, and its formation mechanism is speculated.

Chapter 7:

History of data storage is briefly reviewed. The advanced multiplexed optical data storage technique enables the high capacity data archiving in a limited volume. The experimental setup, data writing and readout process for 5D optical data storage are illustrated. The write and read system is optimized in order to reduce error rate and eventually increase the capacity of the memory. The ultimate objective and future work of 5D optical data storage technique are discussed.

Chapter 2: Experimental setup and analysis tools

2.1 Direct-writing setup

The experiments were performed with a Yb:KGW based femtosecond laser system (Pharos, Light Conversion Ltd.) operating at 1030nm. The system emitted beam with 280 fs pulses, which could be stretched up to 10ps. The repetition rate varied ranging from 10 kHz to 500 kHz. The maximum average power was 6W.

The power control was implemented by a half-wave plate (HW1) and a linear Glan polarizer (P) (Figure 2.1). The polarization of the writing beam was manipulated by a half-wave plate (HW2) located before the focusing optics in order to get rid of unwanted polarization introduced by other optics. Both half-wave plates were mounted on rotational stages, which could be controlled through program. The sample was positioned onto a XYZ air-bearing translation stage (Aerotech Ltd.). The whole power, polarization and movement control were commanded by an Aerotech A3200 system and SCA software (Altechna Ltd.)

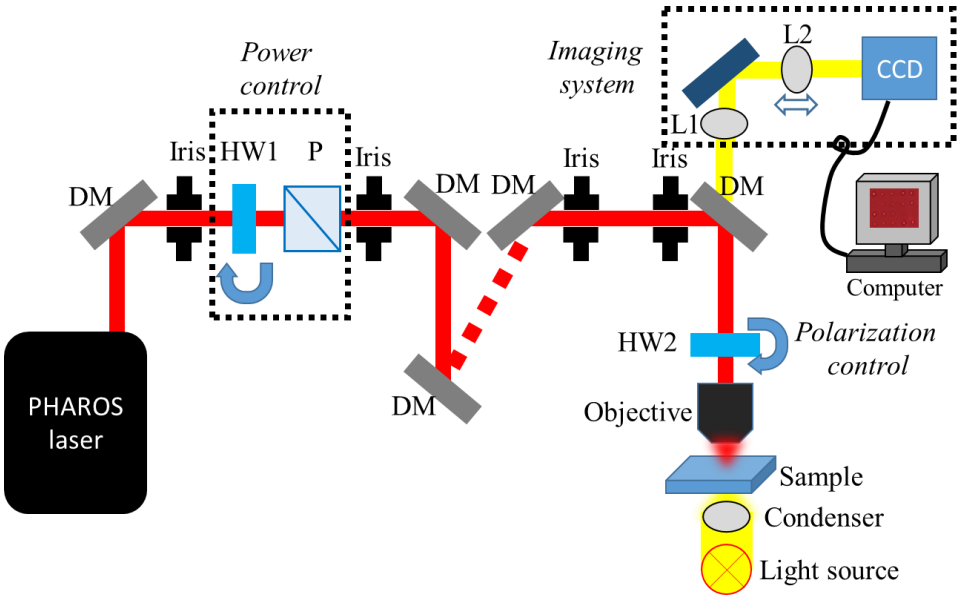

Figure 2.1 Schematic of Femtosecond laser direct writing setup. DM: dichroic mirror, HW: half-wave plate, P: linear Glan polarizer, L: lens.

The transmission imaging system was also assembled into the whole setup (Figure 2.1). The back illumination was achieved by a fiber light source and a condenser. The light was collected by lens (L1) after the objective. L2 was employed in order to alter the imaging plane to where the beam was focused. The real-time imaging was captured with a CCD camera (Retiga 2000, QImaging) and displayed on a computer screen.

This imaging system worked well for transparent material. However, if an opaque sample such as silicon was required to be modified, then the light source and condenser were positioned before the last dichroic mirror and illuminated the sample with a slight angle.

2.2 Setup for the birefringence measurements

The qualitative investigation of the birefringence structures can be achieved by a crossed-polarizers based set-up (Figure 2.2(a)). Only birefringent modification can be observed through two crossed polarizers (Figure 2.2(b)). However, for comprehensive birefringence measurements, it requires a more specific system such as the CRi Abrio imaging system integrated into the Olympus BX51 optical microscope (Figure 2.2(c)).

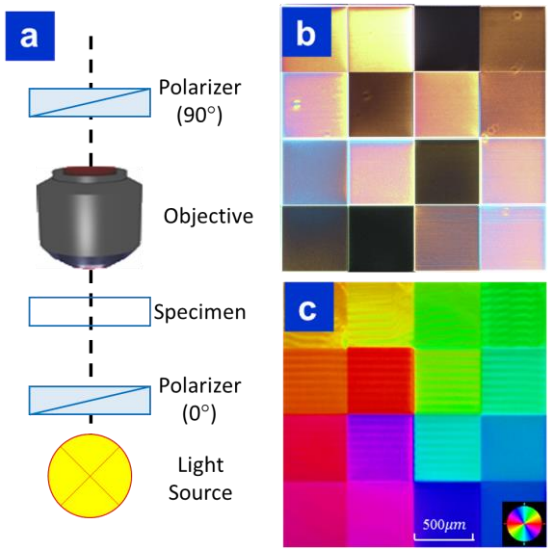

Figure 2.2 (a) Schematic of crossed polarized microscope setup. (b) Crossed polarized microscope image of femtosecond laser written half-wave plate matrix in fused silica glass. (c) The same matrix measured with Abrio system. The colours in (c) indicate the orientation of birefringence slow axis (see legend).

The quantitative characterization of the sample is based on the PolScope microscope system proposed by M. Shribak and R. Oldenbourg [10]. Such a system requires monochromatic circularly polarized light in order to measure all polarizations quantitatively. Therefore, the source light is passed through a BPF functioning at 546nm first then a circular polarizer, which contains a linear polarizer and a quarter-wave plate (Figure 2.3). An elliptical analyser is placed in the imaging path after the specimen and objective. Such an analyser is built from a pair of liquid-crystal retarder plates (LCA and LCB) and a linear polarizer (A)

(Figure 2.3). The retardance of both retarders is manipulated by applying electric field across the liquid crystals.

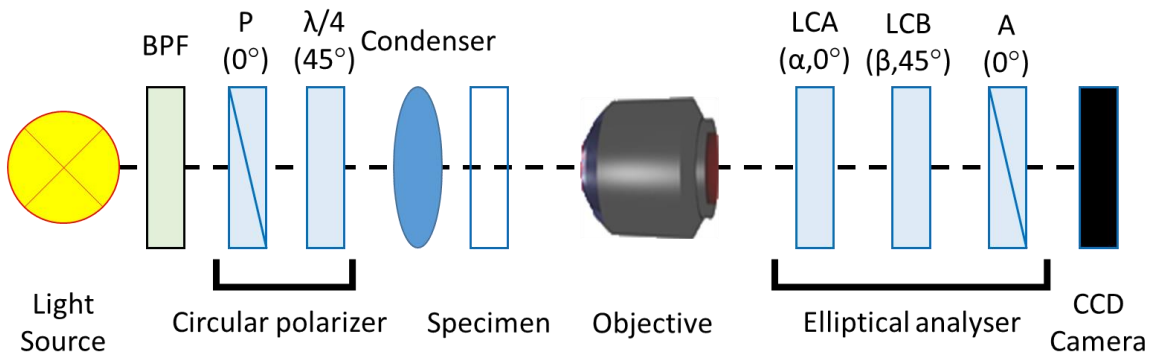

Figure 2.3 Schematic of PolScope birefringence characterization system. BPF, band-pass filter for 546nm; P, linear polarizer; A, analyser. Source: M. Shribak and R. Oldenbourg [10].

Particularly when the second retarder plate (LCB) has quarter-wave retardance (136.5nm), the elliptical analyser functions as a linear polarizer with variable azimuthal [11]. The direction of the azimuthal equals half of the retardance, in degrees, to which the first retarder (LCA) is set.

Assuming the specimen has the distributions of retardance and slow axis orientation of $R(x,y)$ and $\theta(x,y)$ ($\theta(x,y) \in (0,180]$), then the intensity distribution $I(\alpha,\beta,x,y)$ captured by the CCD camera is [10]:

$$\begin{aligned} I(\alpha,\beta,x,y) = \frac{1}{2}\tau(x,y)I_{max}(x,y)[1 \\ + \cos\alpha \sin\beta \cos R(x,y) \\ - \sin\alpha \sin\beta \cos 2\theta(x,y) \sin R(x,y) \\ + \cos\beta \sin 2\theta(x,y) \sin R(x,y)] \\ + I_{min}(x,y). \end{aligned} \qquad \text{Equation 2-1}$$

where $\tau(x,y)$ is the distribution of the isotropic specimen transparency, $I_{max}(x,y)$ and $I_{min}(x,y)$ are the intensity distribution of the illumination on the specimen and depolarized background. α,β are retardance values of LCA and LCB retarders. The distributions of retardance ($R(x,y)$) and slow axis orientation ($\theta(x,y)$) can be retrieved by measuring a set of intensity profiles

A series of intensity profiles $(I_1, I_2, I_3, I_4, I_5)$ are captured by CCD camera while adding a swing value χ to the retarders, the chosen swing value χ is defined by the retardance value of the prevailing specimen [10]:

1: $$I_1 = I(\alpha = \frac{\lambda}{2}; \beta = \frac{\lambda}{4})$$

2: $$I_2 = I(\alpha = \frac{\lambda}{2}; \beta = \frac{\lambda}{4} - \chi)$$

3: $$I_3 = I(\alpha = \frac{\lambda}{2}; \beta = \frac{\lambda}{4} + \chi)$$

4: $$I_4 = I(\alpha = \frac{\lambda}{2} - \chi; \beta = \frac{\lambda}{4})$$

5: $$I_5 = I(\alpha = \frac{\lambda}{2} + \chi; \beta = \frac{\lambda}{4})$$

The λ is the wavelength set by the BPF in Figure 2.3, therefore it is 546nm. Then two parameters, A and B, can be calculated by the measured intensities $(I_1, I_2, I_3, I_4, I_5)$ derived from Equation 2-1:

$$A = \frac{I_2 - I_3}{I_2 + I_3 - 2I_1} \tan(\frac{\chi}{2}) = \sin(2\theta) tanR \qquad \text{Equation 2-2}$$

$$B = \frac{I_5 - I_4}{I_5 + I_4 - 2I_1} \tan(\frac{\chi}{2}) = \cos(2\theta) tanR \qquad \text{Equation 2-3}$$

At last, the retardance can be calculated from:

$$when\ I_2 + I_3 - 2I_1 \geq 0, \quad R = \frac{\lambda}{2\pi}\ arctan\sqrt{A^2 + B^2} \qquad \text{Equation 2-4}$$

$$when\ I_2 + I_3 - 2I_1 < 0, \quad R = \frac{\lambda}{2\pi}(\pi - arctan\sqrt{A^2 + B^2}) \qquad \text{Equation 2-5}$$

and the slow axis orientation:

$$when\ I_2 - I_3 \geq 0, \qquad \theta = -\frac{1}{2}\mathrm{arccot}\left(\frac{A}{B}\right) + 45° \qquad \text{Equation 2-6}$$

$$when\ I_2 - I_3 < 0, \qquad \theta = -\frac{1}{2}\mathrm{arccot}\left(\frac{A}{B}\right) + 135° \qquad \text{Equation 2-7}$$

The PolScope system enables the measurement of the retardance strength up to λ/2, which is 273nm in our case. The slow axis orientation can be measured in a full range from 0˚ to 180˚.

Chapter 3: Computer generated hologram

Spatial light modulators are widely implemented in optical microscopy, aberration correction, optical trapping and arbitrary vector beams generation [12–14]. SLM generated Bessel beams have shown advantages in extending depth of focus, self-reconstruction and high tilt tolerance [15]. Due to the fact that two SLMs can generate an almost arbitrary complex field distribution [16], it can be employed for many kinds of polarization modulation and amplitude modulation. For instance, a SLM based polarization-only modulation has been demonstrated by H. Chen *et al.* [14]. SLMs also enable the simultaneous independent manipulation of multiple optical traps [13]. If applying further power control, the positions of trapped particles can also be manipulated [17].

The electrically addressed spatial light modulator (Model number: LCOS SLM x10468) employed in our laser writing system is based on nematic liquid crystal. The nematic liquid crystal behaves anisotropically due to its geometric structure. It can be considered as a uniaxial crystal with ordinary refraction index n_o along its short molecular axis, and extraordinary refraction index n_e along its long molecular axis (Figure 3.1). The applied voltage on the LC surface tilts the LC molecules, and simultaneously manipulates the phase delay.

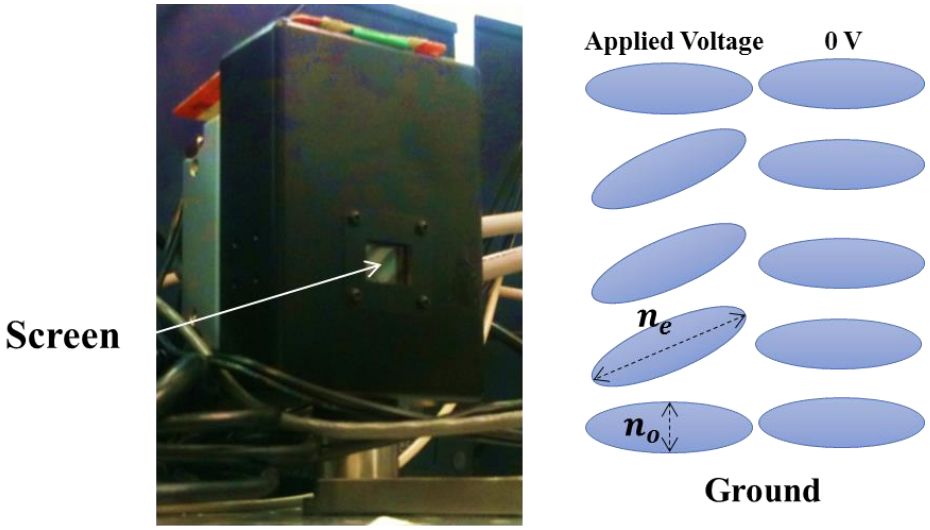

Figure 3.1 The EASLM in our lab (left) and schematic demonstration of its working principals (right).

3.1 Fourier transform and Fourier propagation

According to Fourier optics, the electric field in the back focal plane is the Fourier transform of the field in the front focal plane:

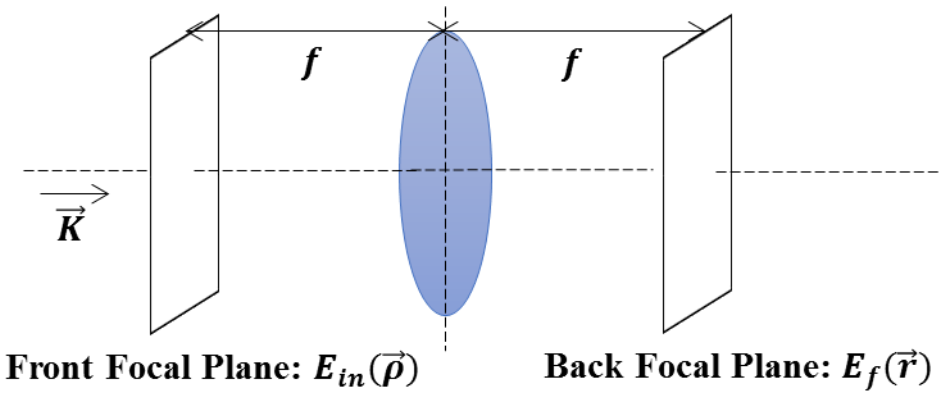

Figure 3.2 Schematic diagram of Fourier transform.

$$E_f(\vec{r}) = \mathcal{F}\{E_{in}(\vec{\rho})\} \qquad \text{Equation3-1}$$

However, sometimes not only the Fourier lens is involved in the beam delivery system. The application may require a certain intensity profile in the front focal plane. The phase and intensity distributions of the beam in an isotropic homogeneous free-space follow a 2D Fourier propagation function:

$$\mathrm{E(x,y,z)} = F_{x,y}^{-1}\left[F_{x,y}[E(x,0)]e^{-jk_z(k,k_x,k_y)z}\right] \qquad \text{Equation3-2}$$

Where

$$k_z(k,k_x,k_y) = -j\sqrt{k_x^2+k_y^2-k^2} \qquad \text{Equation3-3}$$

and $$k = \frac{2\pi}{\lambda} \qquad \text{Equation3-4}$$

λ is the wavelength, z is the beam propagation distance, k_x *and* k_y are variables related to pixel size. The MATLAB code for both Fourier transform and Fourier propagation can be found in the Appendix A. With the equations above, an algorithm is introduced in the next section to obtain the hologram for EASLM.

3.2 Weighted Gerchberg-Saxton algorithm and adapted weighted Gerchberg-Saxton algorithm

Due to the fact that the laser source is a beam with a Gaussian distribution whose intensity is not uniformly distributed, a hologram calculation algorithm should be introduced in order to get the target intensity distribution in the back focal plane. There are many algorithms such as Generalized Adaptive Addictive, Direct Search, Superposition, Random Superposition, Gerchberg-Saxton algorithm and weighted Gerchberg-Saxton algorithm (GSW) [18]. The weighted Gerchberg-Saxton algorithm outweighs the others in computer generated hologram due to its optimal performances in both efficiency and uniformity [18]. This iterative algorithm gives the phase distribution of a pair of lights in the front and back focal planes of a Fourier lens when their intensities are given.

$$u_k = \sqrt{I}\exp(i\phi_{k-1}) \qquad \text{Equation3-5}$$

$$\Phi_k = \arg[FFT\ (u_k)] \qquad \text{Equation3-6}$$

$$U_k = w_k * \sqrt{I_T}\exp(i\Phi_k) \qquad \text{Equation3-7}$$

$$w_{k+1} = w_k\sqrt{(I_T/|U_k|^2)} \qquad \text{Equation3-8}$$

$$\phi_k = \arg[IFFT\ (U_k)] \qquad \text{Equation3-9}$$

$$RMSE = \sqrt{\sum_{i=1}^{N}(|FFT(u_k)|^2 - I_T)^2 / \sum_{i=1}^{N} I_T^2} \qquad \text{Equation3-10}$$

$$e = (\sum_{i=1}^{N}|FFT(u_k)|^2)/P \qquad \text{Equation3-11}$$

where u and U are the light fields in the front and back focal plane, I and I_T are the incident laser beam intensity profile (Gaussian distribution in our case) and target intensity profile, ϕ and Φ are the spatial phase distribution in the front and back focal plane, w is the weighting factor, k is the iteration number, FFT and $IFFT$ represent fast Fourier transform and fast inverse Fourier transform, $RMSE$ and e are the root mean square error and efficiency.

In the 5D optical memory recording procedure, groups of birefringent dots were simultaneously imprinted at the designated position. Each group, containing from 1 to 100 dots, was generated with a liquid crystal based spatial light modulator and 4f optical system. The holograms for the EASLM were generated with an adapted weighted Gerchberg-Saxton algorithm, which enabled discretized multi-level intensity control [18].The discretized multi-level intensity control enabled data multiplexing via retardance.

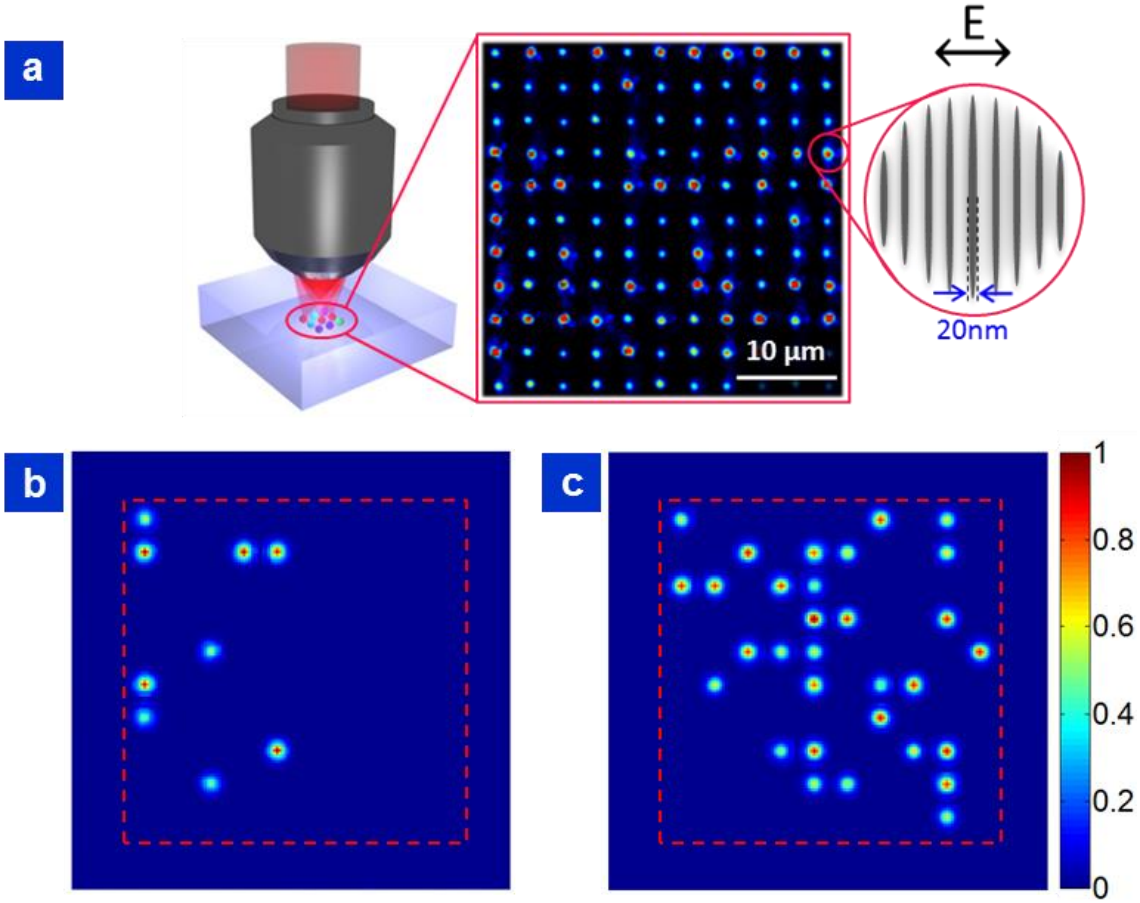

Figure 3.3 Beam Array Multiple-Level Intensity Control. (a) Schematic illustration of modification induced by a femtosecond laser. The colored dots indicate nanogratings induced by different intensity levels. (b-c) Two normalized intensity distributions calculated for two holograms from the adapted GSW algorithm. The area inside the red square is the modification region. The intensity distribution in (c) has more than three times number of the multiple-level spots as compared to in (b).

By using the adapted GSW algorithm, several discrete levels of intensity could be achieved with a single hologram. However, the algorithm controls only the

relative ratio of different intensity levels. The intensity of the source Gaussian beam is fixed, but the targeted dots distribution varies from one hologram to another. Thus, the corresponding intensity levels generated by different holograms are different. Such intensity fluctuations could influence the retardance value from one hologram to another. This problem is resolved by introducing a feedback loop into the algorithm, which redistributes the surplus of energy out of the modification region, fixing each intensity level generated by all holograms to the certain value (Figure 3.3).

The adapted weighted Gerchberg-Saxton algorithm is designed to convert the initial Gaussian intensity distribution I incident on the EASLM into a target intensity distribution with *n* discrete levels I_T^n. The intensity transformation is accomplished via phase manipulation ϕ_k on the EASLM which results into Φ_k phase distribution in the target plane (subscript k indicates the number of iteration). For each iteration, from the combination of phase and intensity, we can construct two complex variables $u_k$and $\mathrm{U_k}$, which represent total light fields on the EASLM and target plane respectively. The discretization of intensity is accomplished by defining weighting factors for each intensity level w_k^n. With increasing number of iterations the calculated intensity distribution is converging towards the target intensity $(I_T^1 + I_T^2 + \cdots + I_T^n)$. An additional feedback loop is employed to fix the intensity levels changing from one hologram to another. In this feedback loop a surplus intensity I_T^b is removed out from the modification region and blocked by the apertures. The algorithm is iterating from Equation7-1 to Equation3-17 until the satisfactory result is achieved. The best results are obtained after approximately 200 iterations. Each hologram takes about one second to generate when using a Dell Precision T7600 computer.

$$u_k = \sqrt{I}\exp(i\phi_{k-1}) \qquad \text{Equation3-12}$$

$$\Phi_k = \arg[FFT\ (u_k)] \qquad \text{Equation3-13}$$

$$U_k^1 = w_k^1\sqrt{I_T^1}\exp(i\Phi_k)$$
$$\vdots\vdots\vdots$$
$$U_k^n = w_k^n\sqrt{I_T^n}\exp(i\Phi_k) \qquad \text{Equation3-14}$$
$$U_k^b = w_k^b\sqrt{I_T^b}\exp(i\Phi_k)$$
$$U_k = U_k^1 + \cdots + U_k^n + U_k^b$$

$$w_{k+1}^1 = w_k^1\sqrt{I_T^1/|U_k^1|}$$
$$\vdots\vdots\vdots \qquad \text{Equation3-15}$$
$$w_{k+1}^n = w_k^n\sqrt{I_T^n/\left|U_k^n\right|^2}$$

$$w_{k+1}^b = w_k^b(\max(mean(|U_k^1|^2)/I_T^1, 0.5)) \qquad \text{Equation3-16}$$

$$\phi_k = \arg[IFFT\ (U_k)] \qquad \text{Equation3-17}$$

The MATLAB code for adapted weighted Gerchberg-Saxton algorithm can be found in the Appendix A. The generated holograms were examined by a self-written program in Visual C++. The interface of the program is shown below.

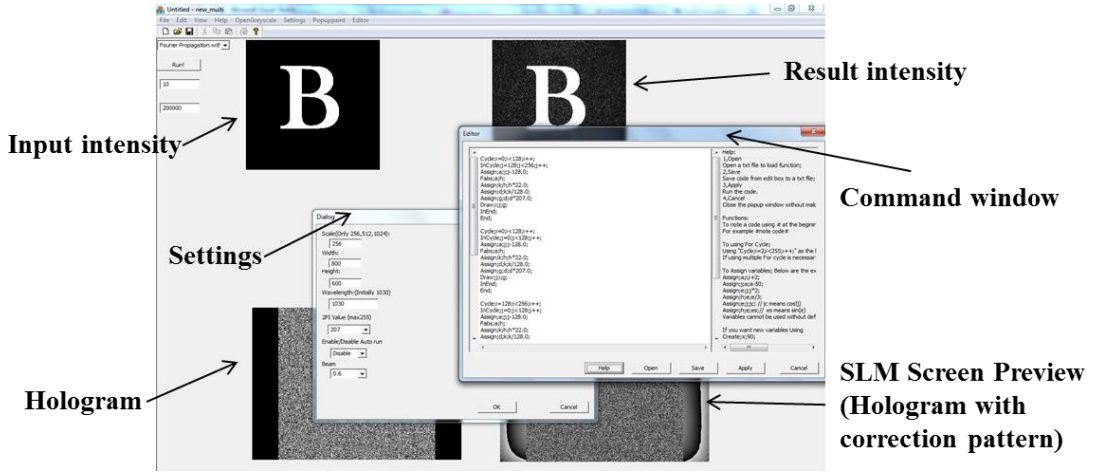

Figure 3.4 Screenshot of the VC program

Chapter 4: Longitudinal electric field

Tight focusing of radially polarized beams generates a longitudinal electric field component oriented parallel to the direction of beam propagation [19–23]. The longitudinal electric field is attractive for many applications, including particle acceleration [24], high capacity optical recording [19,20], near-field microscopy [21], material processing [22,23], metallic particles optical trapping [25] and second-harmonic generation [26]. Although a lot of effort is put into modelling and measurement of the intensity profile of the focused cylindrical vector beams [27–33], little is known about how materials interact with such a strong and localized field.

The electric field of the tightly focused radially polarized beams in the focal region can be decomposed into longitudinally and transversely polarized electric fields. The longitudinally polarized electric field is localized along z axis in the focal plane. Whereas the transversely polarized electric field is distributed in the off-axis area. However, normal beams with a Laguerre-Gaussian amplitude function reduce the total intensity of longitudinal field in the focal region [34]. For the purpose of enhancing the longitudinal electric field, shading masks [34] and annular apertures [27,29,35] are applied into the setup to block the inner part of the beam where low NA is applied. However, the shortcoming of this arrangement is that the main part of laser intensity is lost. To overcome this, we propose a new method that a beam with an annular shape intensity distribution can be manipulated by involving an EASLM into the system. By putting a special generated hologram, the beam with Gaussian distribution can turn into an annular shape. Around 15% of the total intensity is reduced after the phase modulation. The width and radius of the annular shape can be controlled by changing specific holograms.

After the EASLM, the beam passed through a 4F optical system in order to fill the pupil size of the objective lens (Figure 4.1). The radial polarization converter (S-waveplate) was fabricated in fused silica with laser-induced self-assembled nanogratings. The S-waveplate was a linear polarization to radial or azimuthal converter with high damage threshold, 100% polarization conversion, up to 10mm aperture and 55-90% transmission depending on wavelength. The polarization states of the beam after the S-waveplate was changed between

radially and azimuthally polarized beams by rotating the half-wave plate before the S-waveplate.

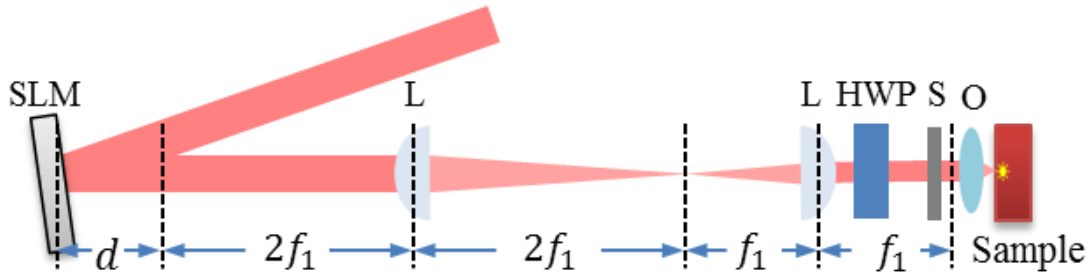

Figure 4.1 Setup for femtosecond laser direct writing. SLM, Spatial light modulator; L, lens; λ/2, half-wave plate; S, S-waveplate; O, objective. d is the distance for beam to propagate after SLM.

The three-dimensional electric field of the focused cylindrically polarized beam was simulated based on the equations below, proposed by Youngworth *et al.* [36]:

Radial:

$$E_{transverse}(r,z) = A\int_{\beta}^{\alpha} cos^{\frac{1}{2}}\theta \sin(2\theta)\,\ell(\theta)J_1(krsin\theta)e^{ikzcos\theta}d\theta, \quad \text{Equation4-1}$$

$$E_{longitudinal}(r,z) = 2iA\int_{\beta}^{\alpha} cos^{\frac{1}{2}}\theta \sin^2(\theta)\,\ell(\theta)J_0(krsin\theta)e^{ikzcos\theta}d\theta, \quad \text{Equation4-2}$$

Azimuthal:

$$E_{transverse}(r,z) = 2A\int_{\beta}^{\alpha} cos^{\frac{1}{2}}\theta \sin\theta\,\ell(\theta)J_1(krsin\theta)e^{ikzcos\theta}d\theta. \quad \text{Equation4-3}$$

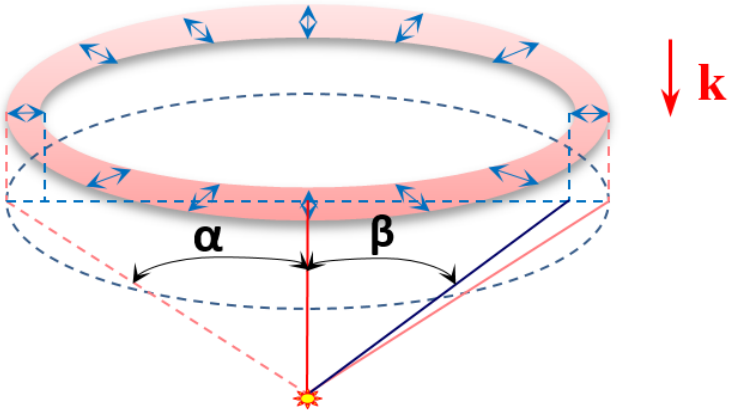

Figure 4.2 Schematic graph for the radially polarized annular beam focused by an objective lens.

In Equation4-1 to Equation4-3, *A* is the coefficient of power (is set to 1), *k* is the wavenumber, *α* and *β* are the maximum and minimum angles of the focus derived from the parameters of the annular beams (radius, width), NA and refractive index. $\ell(\theta)$ is the intensity profile function of the beam. Based on these equations, the intensity distribution of transverse and longitudinal components of a focused radially polarized beam could be modeled. The MATLAB code for electric field of the focused cylindrically polarized beam can be found in the Appendix B.

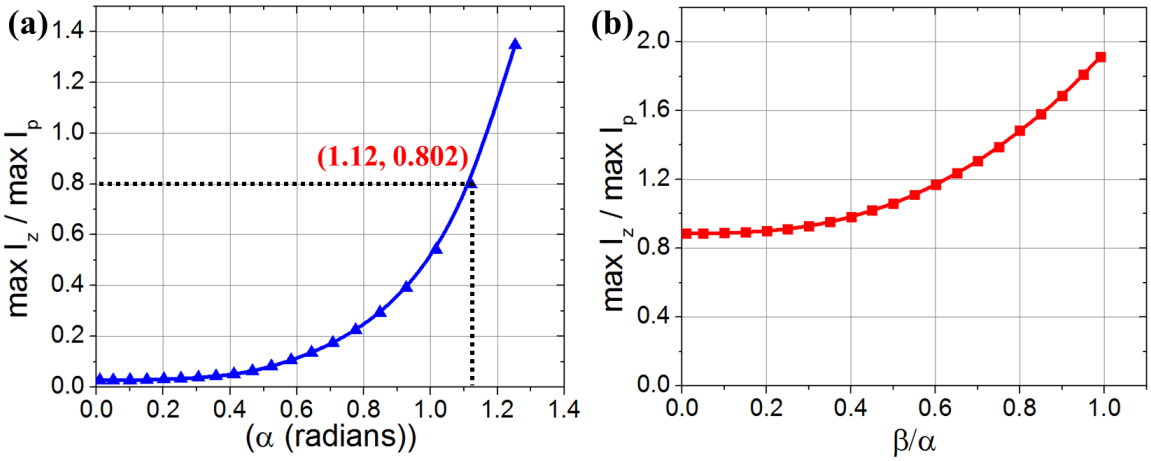

Figure 4.3 The ratio of the maximum intensities of the longitudinal (max I_z) and transverse (max I_ρ) electric fields versus (a) the focusing angle (α) in radians and (b) the ratio of the width of the annular beam (β/α).

The trend of longitudinal versus transverse fields while increasing the focusing angle of a beam with Gaussian intensity distribution can be seen in Figure 4.3 (a). The longitudinal field becomes the dominating field when α is over 1.17 radians (NA = 0.92 for air). At focusing angle equals to 1.12 (when using the 1.2 NA water immersion objective we have), the maximum longitudinal intensity is around 80% of the maximum transverse intensity. However, if we implement such water immersion objective with a radially polarized beam with annular shape, the longitudinal electric field can be even enhanced (Figure 4.3 (b)). As the β/α approaches to one, the ratio of two fields keeps increasing to almost twice. Therefore, the annular shape beam scheme can effectively increase the longitudinal field and be an alternative solution of high NA objective.

However, refractive index mismatch at the interface can strongly affect the light field that oscillates perpendicular to the surface [32,37]. Specifically, the field is suppressed when the beam propagates from a low refractive index into a high refractive index medium. This implies that it may be difficult to employ the field component perpendicular to the surface in the laser processing of materials with high refractive indices.

Successful ablation experiments of borosilicate glass by the single or multi-pulse irradiation [38], and modification of silicon with relatively high-index by the multi-pulse irradiation with the pronounced longitudinal field were reported [39]. Furthermore, enhanced modification by an electric field component perpendicular to the surface via a resonant absorption mechanism [40] was suggested to explain the results of the laser-induced nickel ablation [41]. Nevertheless, the direct experimental evidence confirming that the normal field component could produce stronger surface ablation was not demonstrated.

In this chapter, using amorphous silicon (a-Si:H) we demonstrate that the longitudinal component of the single pulse tightly focused radially polarized beam is inefficient for modification of flat surface. On the other hand, double pulse experiments indicate that the same vector beams exhibit an improved micromachining performance when employed for processing of pillar-like nanostructures on a crystalline silicon surface. The interaction of tightly focused radially and azimuthally polarized beams at the interfaces with different index-contrast is experimentally analysed for both bulk and thin film materials

including silica glass, crystalline silicon and amorphous silicon. The experimental results agree well with the analytical and numerical simulations. In addition, to verify the presence of a strong longitudinal field, the total field of tightly focused radially and azimuthally polarized beams is indirectly visualized by second harmonic patterns generated in a z-cut lithium niobate ($LiNbO_3$) crystal. Moreover, the longitudinal electric field of the focused radially polarized light beam is revealed by the characterization of the self-assembled nanogratings inside silica glass.

4.1 Experimental results

4.1.1 Beam profile

The phase of the narrow ring was designed to be flat along the intensity distribution in order to ensure the whole beam has the same arrival time in the modification region (Figure 4.4(a)). A linearly polarized beam with such intensity distribution (Figure 4.4(b)) was focused underneath a fused silica sample for inspection. A 1.2 NA water immersion objective was applied, elongated structures could be seen under optical microscope due to the longer Rayleigh range of the focused annular shaped beam (Figure 4.4(c) (d)).

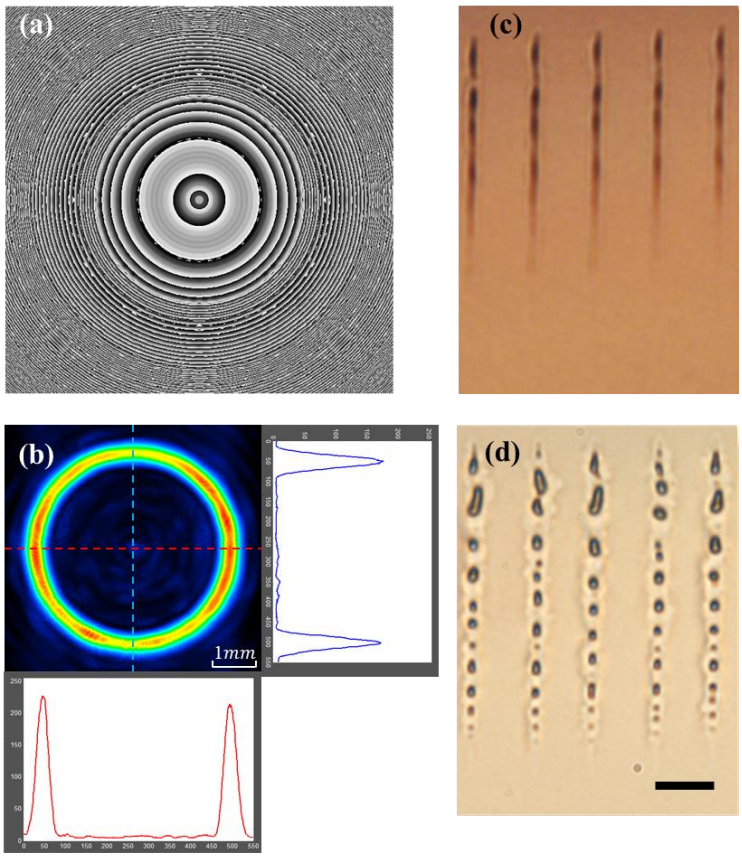

Figure 4.4 (a) The example hologram for generating ring-shaped beam. (b) The intensity distribution measured by CCD. Side view microscope images of structures fabricated by an annular linear polarized laser pulse in silica glass with (c) single pulse and (d) 50 pulses. The scale bar is 5 μm.

A long void parallel to the direction of the incident beam is created by focused annular shaped linearly polarized laser single pulse (Figure 4.4 (c)). The long void breaks into multiple spherical micro-voids when the number of pulses increases (Figure 4.4 (d)).

From above, a decent linearly polarized annular shaped beam was created by a specially generated hologram on EASLM. After passing such modified beam through an S-waveplate (Figure 4.1), the radially and azimuthally polarized beam with annular intensity distribution were obtained (Figure 4.5(a)).

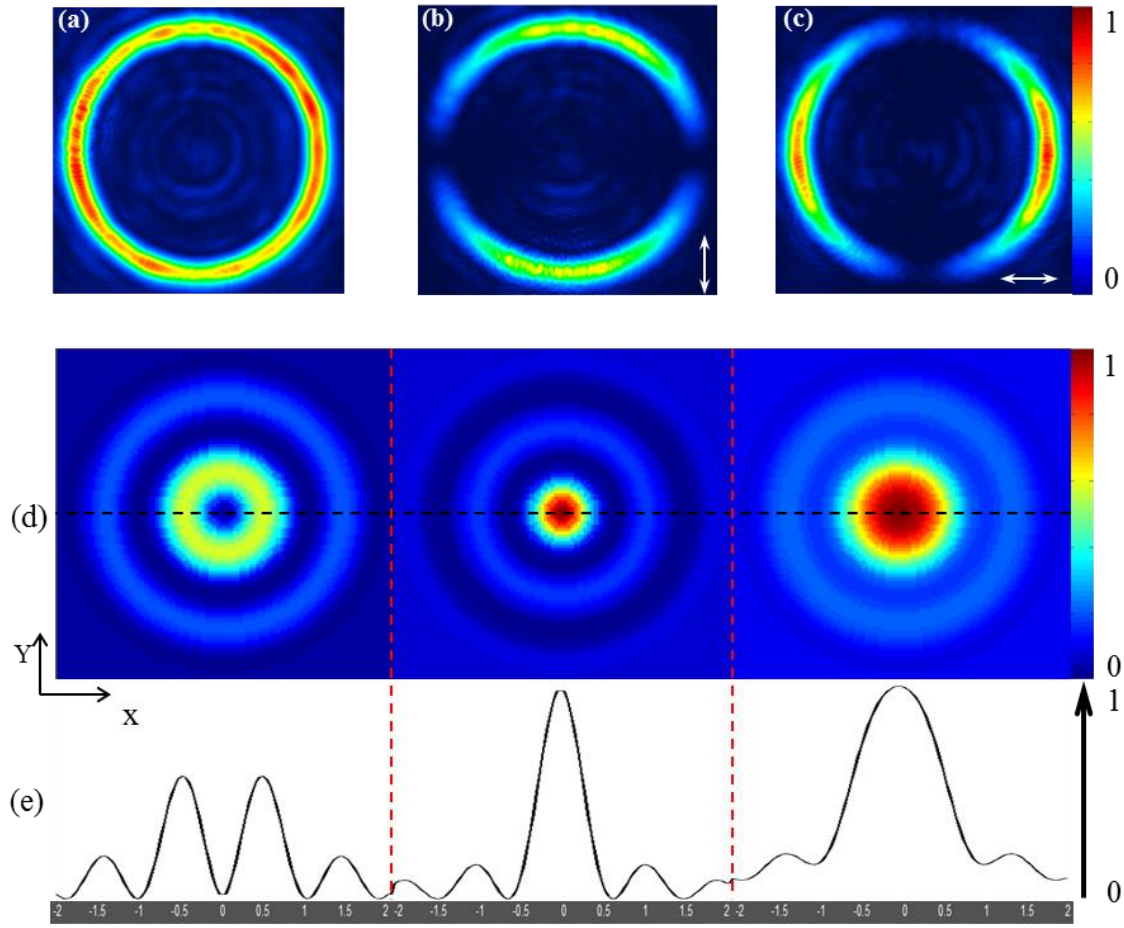

Figure 4.5 (a) The radially polarized ring-shape beam, (b) and (c) is the intensity distributions through linear polarizers measured by CCD. The arrays indicate the transmission axis of the polarizer. (d,e) Normalized intensity profiles of the transverse, longitudinal and total field at focus of the beam. (e) are the corresponding cross section of intensity profiles in (d). The units of x,y are in wavelengths.

The normalized intensity distributions of the transverse, longitudinal and total field at the focal plane could be modeled based on Equation4-1 to Equation4-3 assuming a high NA (1.2) water immersion objective was applied (Figure 4.5(d)). The contribution of the transverse component towards the total intensity of the field was only around 50% (Figure 4.5(e)). The peak intensity of the total field came from the dominant longitudinal electric field (Figure 4.5(e))

Therefore, we already demonstrated the generation of a specific designed cylindrical vector beams with annular intensity distribution. Simulation results indicated that focused such modified radially polarized beams could generate strong longitudinal electric field in the focal region (Figure 4.5).

4.1.2 Second harmonic generation in lithium niobate

A focused radially polarized beam can produce strong longitudinal electric field at focus. However, a focused azimuthally polarized beam has a hollow intensity distribution with only transverse electric field. Longitudinal field does not propagate and is confined to the focal region making its observation very difficult. However, longitudinal component can be visualized via a second harmonic generation in nonlinear crystal. The second harmonic (SH) patterns generated by radially and azimuthally polarized beams can be obtained using the following second-order polarization P(2ω) generated in the z-cut $LiNbO_3$ crystal [42]:

$$\begin{pmatrix} P_x(2\omega) \\ P_y(2\omega) \\ P_z(2\omega) \end{pmatrix} = \begin{pmatrix} 0 & 0 & 0 & 0 & d_{31} & -d_{22} \\ -d_{22} & d_{22} & 0 & d_{31} & 0 & 0 \\ d_{31} & d_{31} & d_{33} & 0 & 0 & 0 \end{pmatrix} \begin{pmatrix} E_x^2 \\ E_y^2 \\ E_z^2 \\ 2E_yE_z \\ 2E_xE_z \\ 2E_xE_y \end{pmatrix}, \quad \text{Equation4-4}$$

for azimuthal:

$$P_x(2\omega) = -2d_{22}E_xE_y,$$
$$P_y(2\omega) = -d_{22}E_x^2 + d_{22}E_y^2,$$

and for radial:

$$P_x(2\omega) = -2d_{22}E_xE_y + 2d_{31}E_xE_z,$$
$$P_y(2\omega) = -d_{22}E_x^2 + d_{22}E_y^2 + 2d_{31}E_yE_z,$$

where Ex,Ey,Ez are Cartesian components of the electric field of the fundamental beam introduced in Eqs. (1-3), and d_{22} = 2.1 pm/V, d_{31}=4.3 pm/V and d_{33}= 27 pm/V are the components of nonlinear susceptibility tensor [43].

In order to verify the existence of the longitudinal field, the cylindrical vector beams were focused inside a z-cut lithium niobate crystal via a 0.65 NA microscope objective 100 μm beneath the surface. The generated SH was collected with a 1.2 NA water immersion objective after the sample, imaging the focal plane and far-field intensity distributions of the focusing lens. The SH patterns were observed for both cylindrical radially and azimuthally polarized beams, while the pronounced longitudinal component in the radially polarized beam results in ~70% higher SH power (at 1.5 TW/cm^2 pump intensities) in comparison with that produced by the azimuthally polarized beam. The SH power increase is caused by the $2d_{31}$ExEz and $2d_{31}$EyEz components of the second-order polarization produced by the non-zero longitudinal (Ez) component of the field at the fundamental frequency (Equation4-4). When the longitudinal field is enhanced, e.g. the ratio with transverse field is 0.58, the contribution of these terms in SH generation increases. The MATLAB code for second harmonic generated by the focused cylindrically polarized beam in $LiNbO_3$ can be found in the Appendix B.

The focal plane SH pattern has the shape of an annular ring for both radial and azimuthal polarizations (see Figure 4.6 (b) (iii), (d) (iii)), while in the far-field SH beam profile becomes polarization dependent. Specifically, if the fundamental beam is azimuthally polarized, the far-field SH beam remains ring-shaped (Figure 4.6 (b) (vi)), while the radially polarized fundamental beam in the far-field evolves into a three-lobed pattern (Figure 4.6 (d) (vi)), which is determined by the orientation of the X and Y axes in the z-cut lithium niobate crystal. These experimental observations agree very well with the results of numerical simulation shown in Figure 4.6 (a), (c), where the polarization component $P_z(2\omega) = d_{31}\left(E_x^2 + E_y^2\right) + d_{33}E_z^2$ is not considered because it does not contribute to the transversal SH field measured in our experiments. One can conclude that the difference in the transverse SH patterns generated by the focused radially and azimuthally polarized beams originate from the longitudinal component of the fundamental light field.

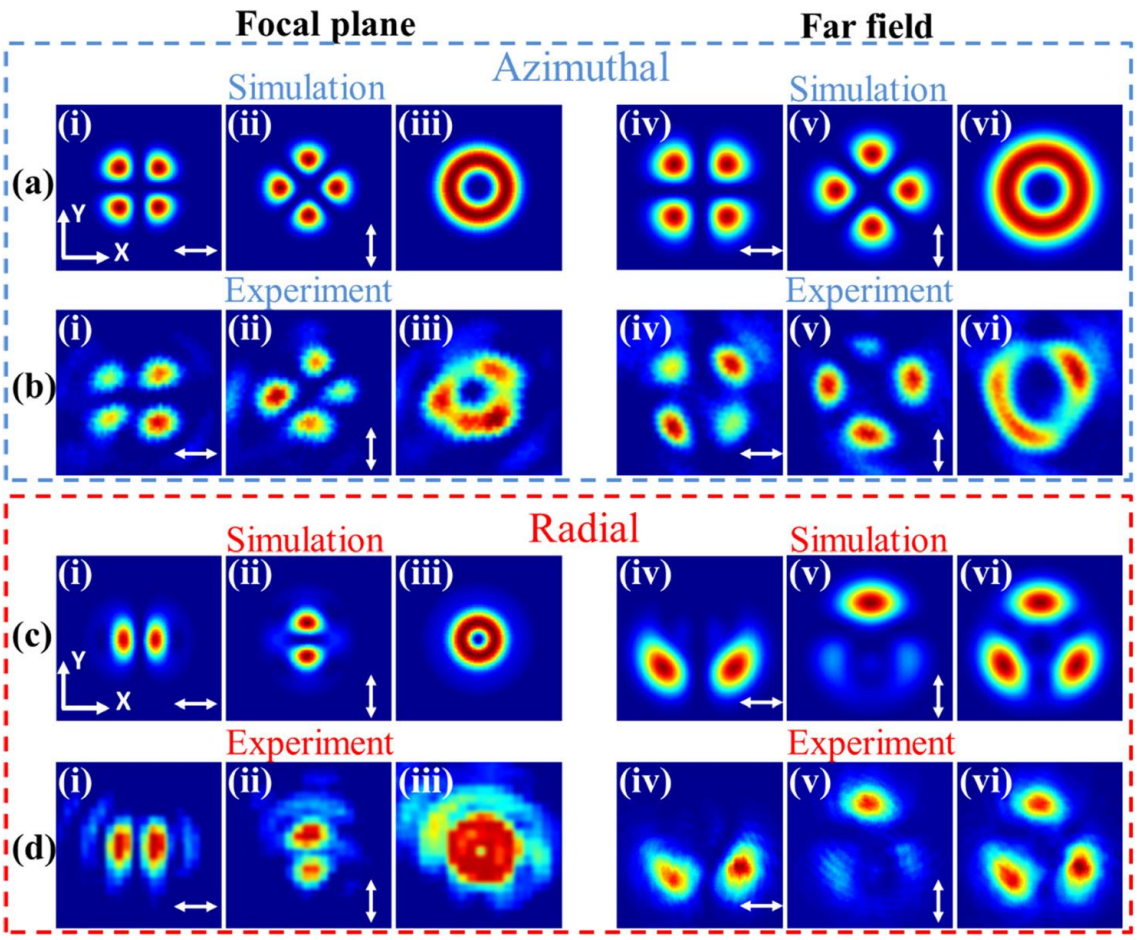

Figure 4.6 Second-harmonic patterns generated by focusing (a, b) azimuthally and (c, d) radially polarized laser beams, (i, ii, iii) imaged focal plane and (iv, v, vi) the far-field of the focusing lens. In simulations only the transverse component is shown. White arrows indicate the polarization state of light after the linear analyser. The x and y axis show the crystal orientation. All intensities are normalized.

4.1.3 Formed birefringence in fused silica

The vectorial distribution of the electric field could be visualized via self-assembled nanogratings, which are always aligned perpendicular to the electric field of the incident beam [9,38,44,45]. Tailored optical vector beams including radially and azimuthally polarized could be also exploited for complex surface structuring with ultrashort light pulses [46].

In further experiments, single dots were imprinted inside silica glass to visualize the vectorial distribution of electric field in the focus. A train of 2000 pulses with

250 nJ pulse energy was focused via a 0.65 NA objective, 120 µm beneath the substrate surface. Under these conditions, the self-assembled nanogratings are induced. The nanostructures with the sub-wavelength periodicity behave as a uniaxial birefringent material where the slow axis is oriented perpendicular to the beam polarization. The slow axis orientation with corresponding vectorial distribution of electric field was mapped using quantitative birefringence measurement system (Figure 4.7).

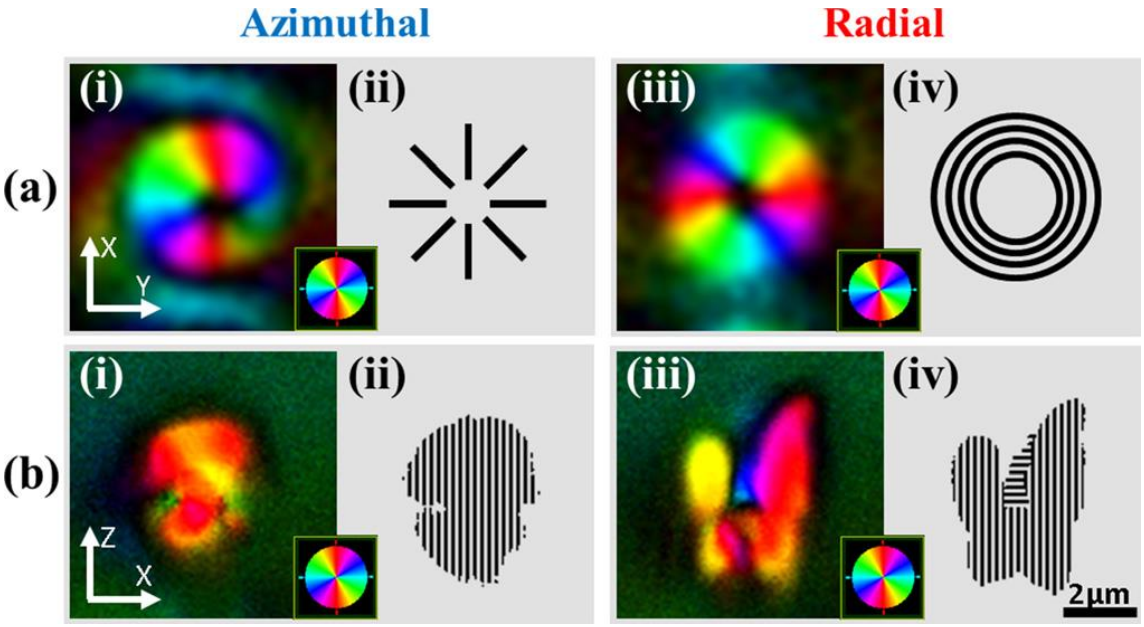

Figure 4.7 Slow axis characterization of the birefringent structures inside silica glass induced by azimuthally (left) and radially (right) polarized laser beams. (a) (i, iii) Top view and (b) (i, iii) side view of the slow axis orientation, with (a) (ii, iv), (b) (ii, iv) their corresponding schematics of the possible nanogratings distribution. Pseudo color indicates the direction of slow axis (insets).

The birefringence cannot be observed if the optical axis is oriented perpendicular to the image plane (Figure 4.7 (a)(iii)). Thus the slow axis induced by the longitudinal field can be visualized only from the side of the structure. One can observe from Figure 4.7 (b)(iii) that the center of the light-induced modification is occupied by an anisotropic structure (light beam) having a slow axis (polarization) oriented perpendicular (parallel) to the beam propagation direction. However, on the sides of the modified region the nanogratings with orthogonal orientation are induced, which reveals the transverse component of

the light polarization (Figure 4.7 (b)(iv)). In contrast, after irradiation with the azimuthally polarized light the anisotropy associated with longitudinal component is not observed (Figure 4.7 (b)(i)). As the structures were generated by focused cylindrical vector beams, there is no particular viewing axis from sides.

4.1.4 Surface modification on dielectrics

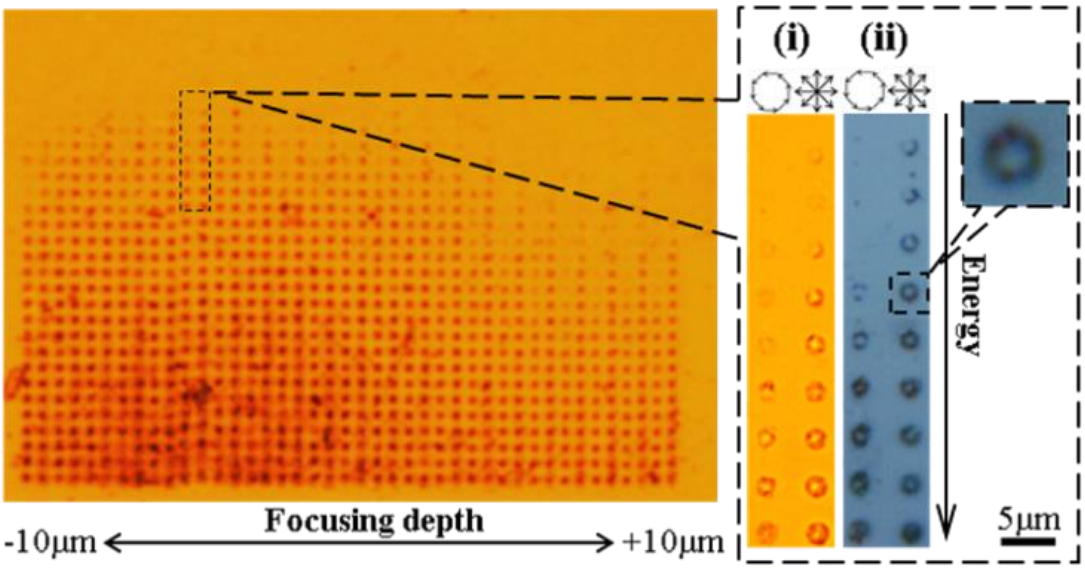

Figure 4.8 Optical transmission images of structures imprinted by annular-shape of radially and azimuthally polarized beams in amorphous silicon film at different focus planes, where in the inset the same structures are compared in transmission (i) and reflection (ii) modes. The pulse energy in the inset (right images) varies from 30 nJ to 70nJ.

Further, to directly imprint the intensity distribution of the tightly focused annular cylindrically polarized beams in high-index material, we carried out the experiments on irradiation of 300 nm thick a-Si:H film. The water immersion microscope objective of 1.2 NA was used for focusing of the beam. The irradiation with pulse energies below 150 nJ were ensured to induce the nanocrystalline type of modification without ablation in amorphous silicon [47,48]. In total the 21 sets of dots were imprinted by a single pulse irradiation of radially or azimuthally polarized beams at different focusing

depths ranging from -10 μm to 10 μm, relative to the substrate surface (Figure 4.8).

Weak dependence of the modification on the focus depth was observed indicating a Bessel-like long Rayleigh length, typical for cylindrically polarized beams (Figure 4.8). The threshold energy of modification was more than 40% lower for radially polarized than for azimuthally polarized beams, 30 nJ versus 50 nJ, respectively. This phenomenon could be explained by the lower Fresnel reflection and different material transformation dynamics for p-polarization compared to s-polarizations at the interface of modified region. The azimuthally polarized beam is everywhere s-polarized, whereas, the radially polarized beam is p-polarized in the off-axis area. Since the transmission coefficient of p-polarized beam is higher than s-polarized beam, the radially polarized beams require less energy to induce modification compared to the azimuthally polarized one. However, in both cases only the ring-shaped patterns were produced. The modification in the center of annulus, where the strong longitudinal field is present, was not observed. The surface of the film remains flat in the conditions of irradiation below the ablation threshold. Consequently, if the second pulse is fired, modification of the film qualitatively will be the same as by the first pulse and will not reveal the presence of longitudinal component.

Finally, we performed experiments on ablation of p-type crystalline silicon (111). The radially and azimuthally polarized beams with pulse energy of 150 nJ were focused on the surface via a 1.2 NA water immersion objective. The irradiation by the single pulse radially polarized beam resulted in a ring-shaped modification with nanopillar structure in the center (Figure 4.9 (top-left)). Specifically, the molten silicon was pushed away from the modification region by the rarefaction (shock) wave [49], then, re-solidified and formed the rim of the crater structures. The excess material pushed to the center of the crater forms the nanopillar structure. The structure showed a height of around 400nm above the crater's surface from the side view of SEM profile. In the case of azimuthal polarization, the nanopillar structure is not formed due to the lack of deposited energy and possibly the different material dynamics after irradiation. The deposited energy is suppressed by the higher Fresnel reflection for s-polarization compared to p-polarization at the interface. (Figure 4.9 (top-left)).

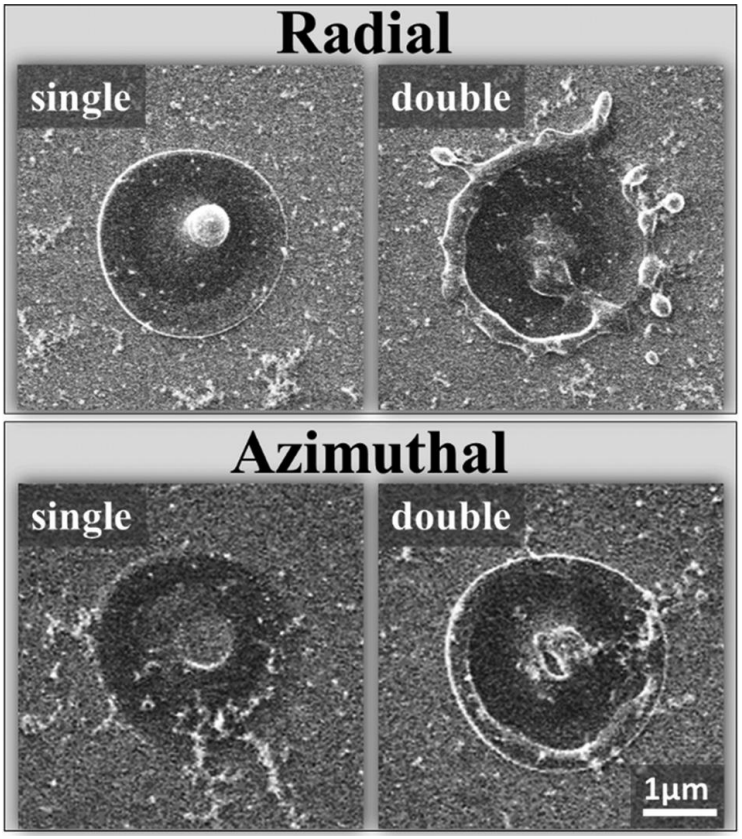

Figure 4.9 SEM images of the laser processed crystalline silicon surface. Each spot was irradiated with single (left) and double (right) pulse radially (top) and azimuthally (bottom) polarized beams with energies of 150 nJ.

The laser-induced nanopillar, which was emerged along the beam propagation direction, was subsequently ablated during the second pulse irradiation due to the enhanced transmission of the longitudinal field along the distorted interface (Figure 4.9 (top-right)). The re-solidified silicon droplets could be found both inside and outside the crater. The irradiation by double pulse azimuthally polarized beam kept the center untouched (Figure 4.9 (bottom)). This observation indicates that the needle shaped surface structures aligned along the beam propagation direction are necessary for interaction with the longitudinal field.

4.2 Discussions and conclusions

Numerical simulations of focused vector beams were performed to understand why the strong effect of longitudinal field did not produce modification in amorphous and crystalline silicon [33]. The simulations revealed that the transverse electric field propagates without significant amplitude changes, while the longitudinal electric field is discontinuous through the interface when the incident beam is focused at the water/silicon interface (Figure 4.10 (top)). The magnitude of longitudinal component decreases by a factor of ε2/ε1 (~7.4), where ε1 and ε2 are the dielectric constants of the media. Moreover, the total intensity distribution of radially and azimuthally polarized beams after the transmission through the water/silicon interface (Figure 4.10 (top)) match well with the structures imprinted in the amorphous silicon film (Figure 4.8).

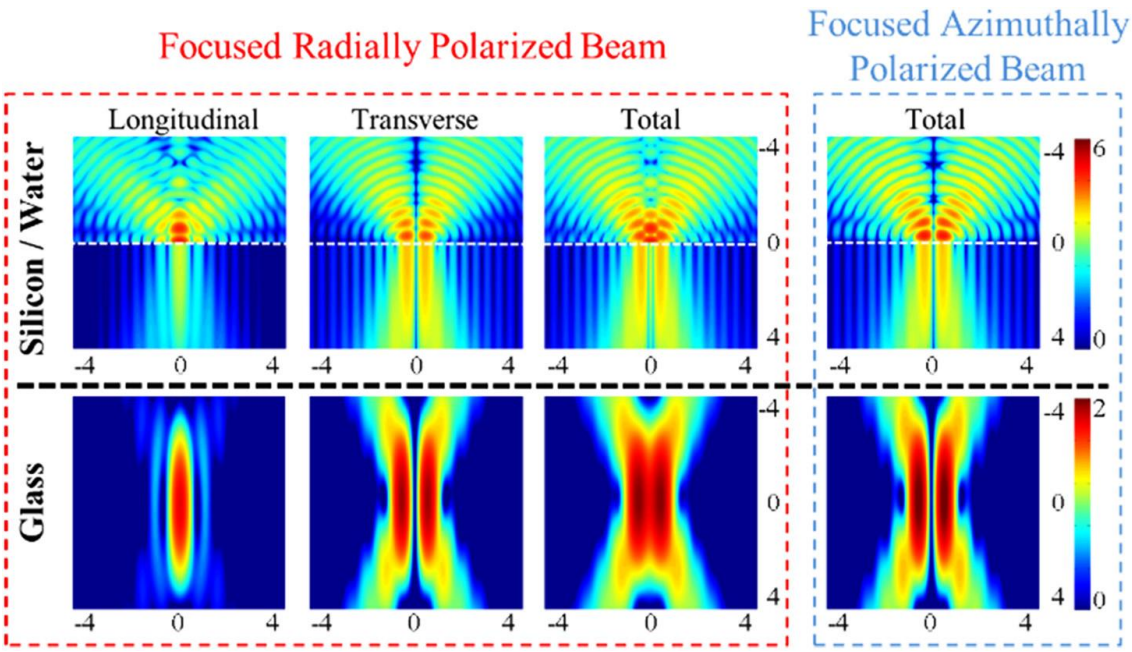

Figure 4.10 Simulation of cylindrical vector beams focused on silicon surface (n = 3.613) (top) and inside silica glass (n = 1.458) (bottom) via a 1.2 NA water-immersion (n = 1.3265) microscope objective (top) and via a 0.65 NA dry microscope objective (bottom). Color scales are logarithmic in arbitrary units; axes are in the units of wavelength.

On the other hand, inside the silica glass the magnitude of longitudinal and transverse components are of the same order, since the refractive index contrast

at the air/silica interface is relatively low (Figure 4.10 (bottom)). Experimentally, it was confirmed by the nanogratings formation both parallel and perpendicular to the beam propagation direction (Figure 4.7).

In conclusion, we have demonstrated the evidence of longitudinal component of tightly focused radially polarized beam by the observation of enhanced second harmonic generation in the z-cut lithium niobate crystal and by the laser-induced anisotropy oriented perpendicular to the longitudinal field in silica glass. Despite the lower threshold of ring-shaped modification in amorphous silicon film and the nanopillar formation in crystalline silicon, the longitudinal electric field generated by the single pulse radially polarized beam produces a negligible modification, which can be explained by the discontinuity of longitudinal field at the high-index-contrast interfaces. Thus, the longitudinal electric field is not effective for modifying flat surfaces of materials with high refractive index when irradiating from a low index medium. On the other hand, the effect of the high-index-contrast interface can be eliminated by using high numerical aperture immersion objectives, e.g. solid immersion lenses. Alternatively, the sub-wavelength structures oriented along the beam propagation direction such as nanopillars or enhanced surface roughness could be beneficial for material processing by pronounced longitudinal field.

Finally, if considering using focused radially polarized beam to create a small spot for data recording, one must be aware of the possible high-index-contrast interface.

Chapter 5: Anisotropic local field enhancement

It is well recognized that tightly focused ultrashort laser pulses can induce localized structural modification with the precision of tens of nanometers [50,51]. As a result, femtosecond pulses have been applied for high capacity multi-dimensional optical memory [52,53], fabrication of polarization sensitive elements [54] and micro-fluidic channels [55]. The interaction of the ultrashort light pulses with material is affected by multiple parameters such as pulse duration, pulse energy, spatio-temporal coupling and polarization. For instance, the tightly focusing linear polarization one can observe a strong anisotropy of the electromagnetic near-field distribution [56,57] affecting the laser material micro-processing [58,59]. Such anisotropy could be observed on many materials after multi-pulse ultrashort laser irradiation in the form of polarization-dependent structures [9,60,61]. Even in the single-pulse regime, elongated modifications along the laser polarization were observed in poly-methyl methacrylate ablation experiment (Figure 5.1) [58].

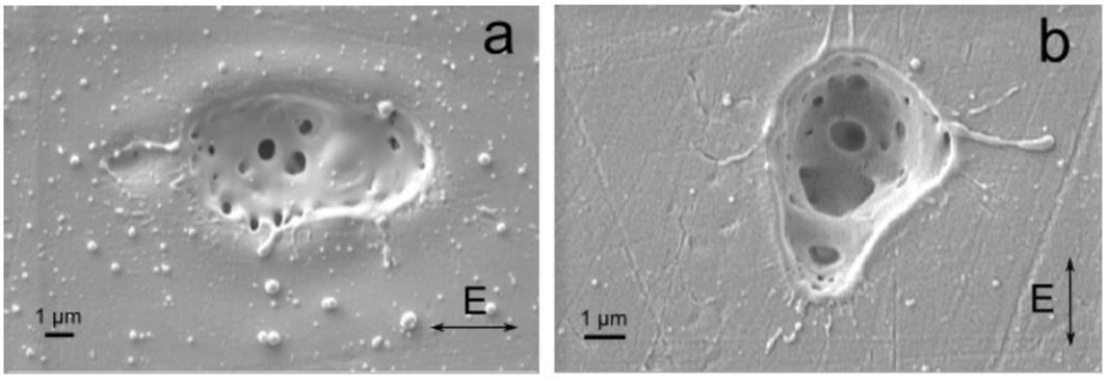

Figure 5.1 SEM images of ablation craters in PMMA produced by single-shot ultrashort laser (45 fs) irradiation of different polarizations. Image source: J. Guay *et al.* [58]

However, the origin of these laser-induced surface patterns, which occur after single or multiple pulses, is still under debate [59,60,62–65]. Various mechanisms, such as interference of incident laser and surface electromagnetic

wave [64], surface plasmon polaritons [66] and second-harmonic generation [67], have been proposed. The majority of the studies is focused on multiple pulse experiments and lacks information on the simplest case: single and double pulse-induced modification. At the very early stages of ripple-like structure formation, the laser-induced defects on the surface could trigger further modification [68,69].

In this chapter, I will present a detailed analysis of a newly observed reproducible silicon modification upon the single and double pulsed laser irradiation. I will demonstrate that the first pulse melts a thin layer of silicon and produces an isotropic crater, while the second pulse leads to its asymmetric deformation. The performed numerical calculations of the electric near-field distribution clearly demonstrate that the generated symmetric structure acts as a seed pattern for the subsequent polarization sensitive near-field imprinting. These results provide a basic understanding of silicon micromachining.

Experiments were performed using a mode-locked Yb:KGW ultrafast laser system (Pharos, Light Conversion Ltd.) operating at a wavelength of 1030 nm, 20kHz repetition rate, and 330 fs pulse duration. Series of dots were printed on the surface of p-type crystalline silicon (111) substrate, by either single or double pulse (50 μs time delay between pulses) irradiation with a linear polarization controlled by a zero-order half-wave plate. The laser beam was focused via a 0.65NA objective lens in the range from 0 μm to 12 μm above the substrate surface. The pulse energy was varied up to 600nJ in order to depict a large modification window.

After laser irradiation, the morphological changes of the surface were characterized using optical microscope (BX51 Olympus Inc.), scanning electron microscope (SEM) (Zeiss Evo50) and atomic force microscope (AFM) (Nanonics Multiview 2000).

5.1 Single pulse modifications on silicon

A smooth and symmetric 150nm deep crater-shaped structure with a rim was observed after focusing a single 120nJ(1.35J/cm^2) pulse 4μm above the silicon surface(Figure 5.2 (a)–(c)). The crater's radius of curvature of 2.69±0.08 μm was estimated from AFM profiles (Figure 5.2 (c)). Material ejection was not observed at these pulse energies, thus, we assume the structure was formed by rarefaction (shock) wave, which pushed the molten material from the centre to the periphery of the irradiated zone [49]. The light was absorbed by electrons, which afterwards transferred energy to the lattice via electron-phonon coupling resulting in an isotropic heating zone without collateral damage [70]. During the irradiation with the first pulse, substrate's surface was flat and homogeneous leading to an isotropic near-field distribution. Asymmetry was not observed in the crater-shaped structures induced by a single pulse with six different orientations of linear polarization (Figure 5.3(e)).

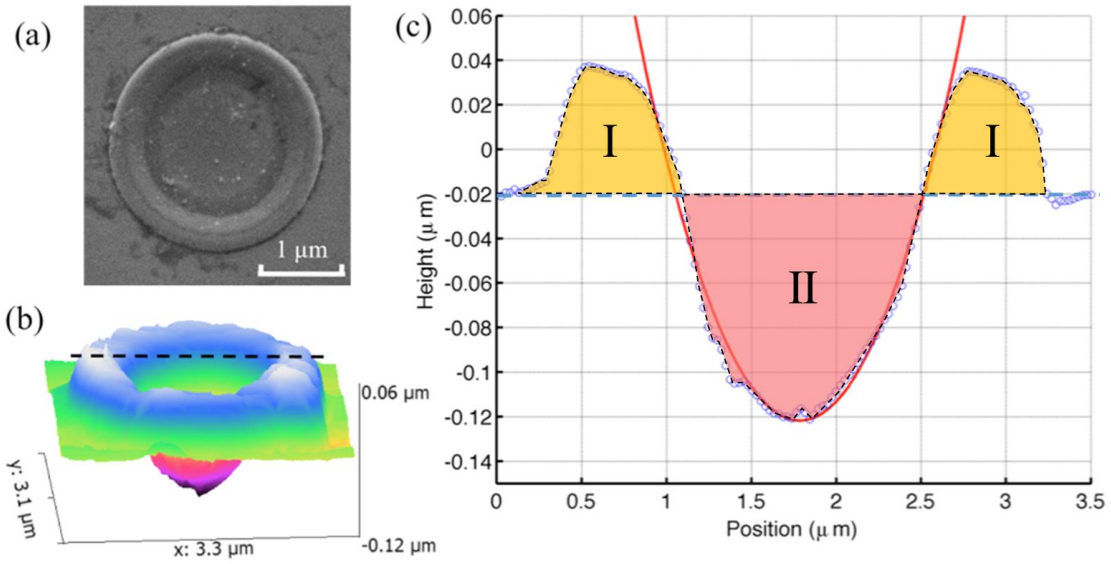

Figure 5.2 SEM (a) and AFM (b) images of the structure imprinted by one linearly polarized laser pulse of 120 nJ. (c) AFM profile taken along black line and the fitting curve for the surface curvature with R = 2.7 μm. The volumes of material, which moves on (area I), or is removed from (area II) are 0.062 and 0.070 μm^3 respectively.

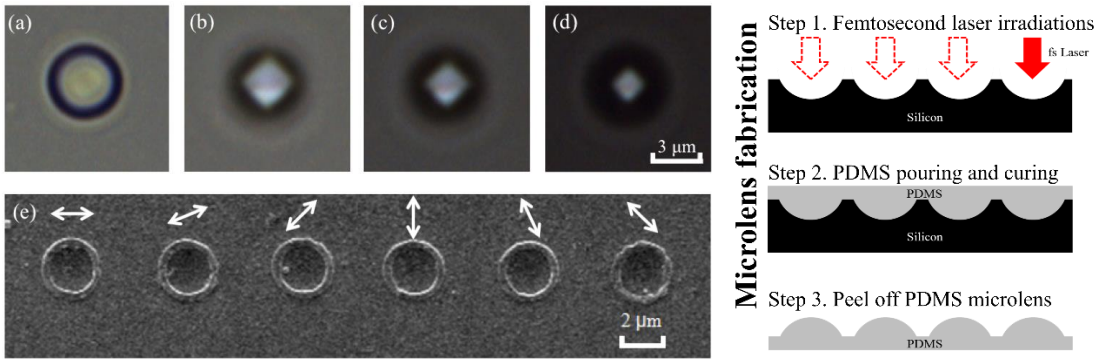

Figure 5.3 Left, (a) to (d) are the optical images created by one horizontally polarized laser pulse. (b) to (d) are the images of the modification in (a) with unfocused microscope while gradually closing a rectangular aperture. (e)SEM image of the modifications created by single pulse irradiation with different polarization orientations. Right, the proposed microlenses fabrication process.

The isotropic crater structures within its smooth surface can be implemented as a mold for the microlenses fabrication (Figure 5.3 right) or itself can be employed as optical microreflectors with a focal length of 1.345±0.04 μm. (Figure 5.3 (a)-(d)). To demonstrate this, the sample was examined under an optical microscope in the reflection mode, when the illumination light was partly blocked by an aperture. While moving the focal position of the microscope objective, we could clearly see the rectangular aperture imaged by the microreflector (Figure 5.3 (a)-(d)). The array of 5×5 microreflectors was imprinted on the silicon surface and implemented as a wavefront sensor (Figure 5.4). After examining the shape of each crater shown in Figure 5.4 (a), the position of the geometrical focus was estimated. Tracking the lateral displacement of the imaged aperture (Figure 5.4 (b)), the map indicating the wavefront of illumination can be extracted (Figure 5.4 (c)).

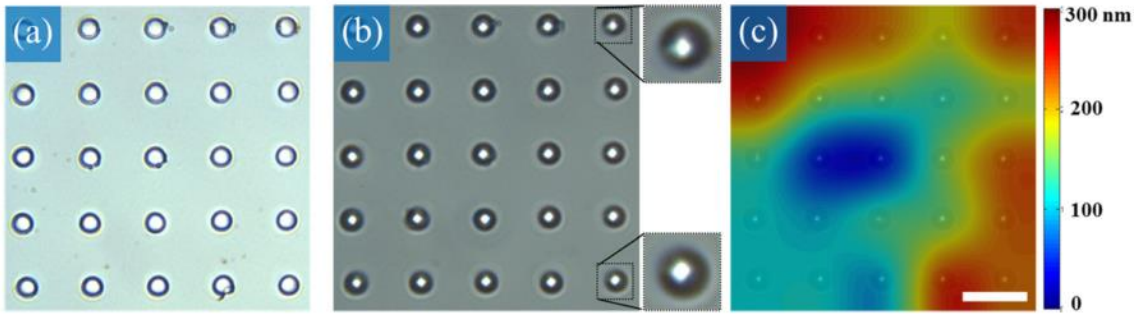

Figure 5.4 Silicon microreflectors array induced by single femtosecond laser pulses. Optical reflection images were taken (a) without and (b) with microscope aperture inserted in front of the illumination source. (c) The focal point displacement map caused by the wavefront of illumination was extracted from (a) and (b) images. The scale bar is 10 μm.

5.2 Double pulse modifications on silicon

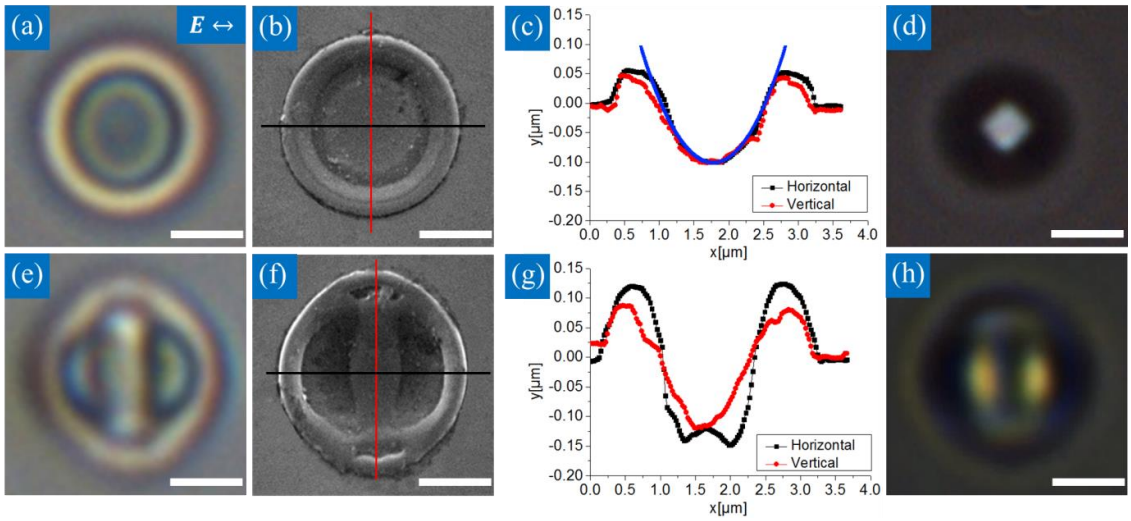

Figure 5.5 Silicon structures induced by linearly polarized single-pulsed (a-d) and double-pulsed (e-h) femtosecond laser irradiation. (a), (e) Optical reflection and (b), (f) topological SEM images, as well as (c), (g) AFM profile scans were performed after the first and second pulses. Pulses with the energy of 120 nJ were focused 4 μm above the silicon surface (2.7 J/cm^2). The repetition rate was 20kHz. *K* and *E* indicate the direction of pulse propagation and its state of polarization, respectively. The images in (d) and (h) represent the microscope aperture imaged using the laser-induced structures shown in (a) and (e), respectively. The scale bars: 1 μm.

Unexpectedly, we observed very different modification with double pulse structuring of the sample. And the formation of such structure was not affected by the time separation between pulses when the repetition rate was less than 20kHz. Here, an anisotropic transformation of the modified region was observed with the formation of several peculiar features (Figure 5.5 (e)–(h)). First, in the middle part of the crater, two enhanced modification zones oriented perpendicular to the light polarization were induced. As a result, a bridge-like structure with a height of roughly 25 nm was formed (Figure 5.5 (e)–(g)). The orientation of the bridge was perpendicular to the polarization and located in the center of the modified region. Secondly, the rim was deformed at the tips of

the bridge slightly elongating the crater shape. The crater depth along the direction parallel to the beam polarization was increased by more than 80%, while along the perpendicular direction only by 30%. The two induced lobes located inside the crater were functioning as twin microreflectors (Figure 5.5 (h)).

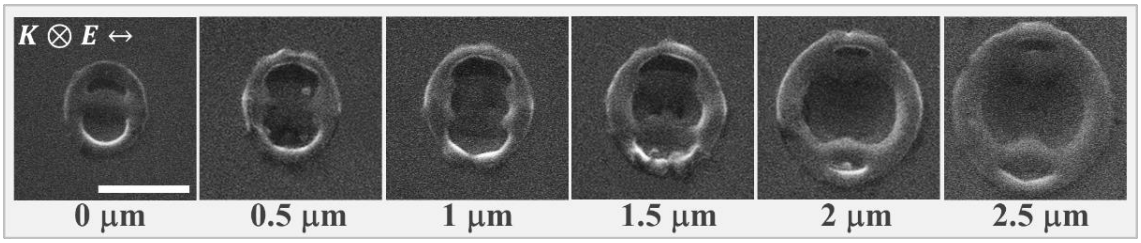

Figure 5.6 SEM images of the linearly polarized double pulse modification induced at different focusing position varying from 0 μm to 2.5 μm above the surface. The pulse energy was fixed at 15 nJ (0.27–0.47 J/cm^2). Scale bar is 1 μm.

The shape of the structure was changing significantly when the laser beam was defocused (Figure 5.6). The bridge was either merging or separating depending on the beam focal position. If the double pulse laser beam was focused on the surface, the bridge-shape structure oriented parallel to the polarization direction was produced (Figure 5.6, left), whereas the structure similar to the one in Figure 5.5 (f) emerged when the focus of the beam was above the sample surface (Figure 5.6, right).

The wavelength-sized polarization sensitive structures on silicon surface (Figure 5.6) may find applications for the polarization-multiplexed optical memory. The size and orientation of the structure can be independently manipulated by the energy of the first pulse and polarization of the second pulse, respectively. Assuming that the shorter wavelength should produce proportionally small structures with the same polarization dependence, we estimated that by recording data with wavelength of 300nm, a CD-sized disc with the capacity of 36GB can be achieved (0.5μm between track pitches, 6 bits polarization-multiplexed data resulting from 64 polarization states between 0° and 180°, and 2 bits power-multiplexed data per structure). The read-out technology could be implemented by monitoring the intensity of the linearly polarized laser beam, when the reflected light is modulated (Fresnel conditions) by the surface

morphology. The modulation in intensity and polarization could be detected using a quadrupole detector, which is already exploited in the traditional optical data storage read-out.

In addition, experiments were performed to demonstrate the multilevel polarization sensitive encoding on silicon surface (Figure 5.7). First of all, the isotropic craters were imprinted by the single pulse irradiation (Figure 5.7 (a)). Later, during the encoding stage, the subsequent irradiation with the different states of polarization of the writing beam was used to control the orientation of anisotropy of the imprinted structures (Figure 5.7 (b)-(c)). The slight asymmetry of the patterns in the direction perpendicular to the polarization could be explained by the displacement of the focal spot during the polarization rotation.

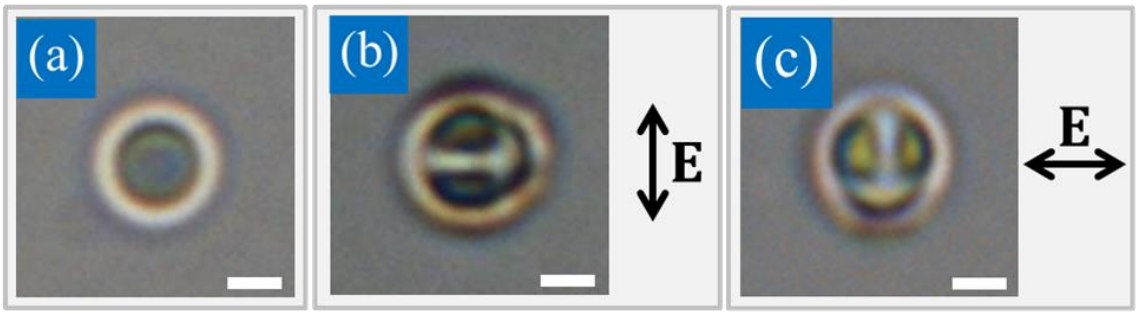

Figure 5.7 Optical microscope images of the silicon surface modified with (a) single and (b)–(c) writing pulses with two different polarizations indicated by arrows. Pulses with the energy of 40 nJ (0.77 J/cm^2) were focused at 2.5 μm above the surface. The scale bars: 1 μm.

For the theoretical analysis, the corresponding total near-field distribution was obtained simulating the propagation of the focused second pulse through a symmetric crater-shape structure pre-defined by the first pulse (Figure 5.8). A commercial-grade simulator (Lumerical) based on the finite-difference time-domain (FDTD) method was used to perform the numerical calculations of a total near-field distribution. Here, we distinguish between two regimes of polarization dependence for the light propagating through a large size ($d > \lambda$) and a subwavelength size ($d < \lambda$) single circular crater. We can assume that such a structure in the near-field behaves as an aperture. In this case, the explanation may be applied on the basis of an anisotropic near-field distribution dominated

for different regions of structure within the surface-wave modes and the field coupling to the waveguided modes of the aperture. For all conditions, two sets of the lobes of an intense field localized under the rim of the structure are generated with the orientation parallel to the light polarization (Figure 5.8 (a) and (c)). The generated mode in the center of the structure almost vanishes when the crater size is smaller than the excitation wavelength ($d/\lambda = 0.9$) (Figure 5.8 (a). Then the strong field generated inside the rim region dominates (Figure 5.8 (a). In such a system, it is expected to have a modification localized at the edges of the crater and oriented parallel to the field polarization. When the crater size increases ($d/\lambda = 4.0$), the lobes generated inside the rim are accompanied by the series of perpendicular lobes generated in the central part of the crater (Figure 5.8 (c)).

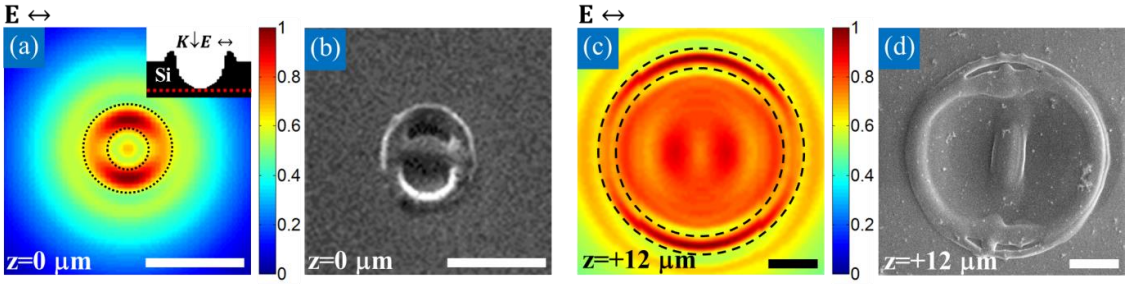

Figure 5.8 (a) and (c) Calculated total electric near-field distribution of the light propagating through an isotropic crater-shape silicon structure, and (b) and (d) its subsequent polarization sensitive modification measured by SEM. The double pulse laser beam was focused at (a) and (b) 0 µm and (c) and (d) 12 µm above the substrate surface with the pulse energies of 15 nJ (0.47 J/cm^2) and 300 nJ (0.55 J/cm^2), respectively. The dashed black lines in (a) and (c) indicate the contours of crater-shape pattern used for the calculations. Insets in (a) show the geometry of the pattern used to mimic the conditions during the second pulse irradiation. The dashed red lines--planes of the near-field monitoring. The scale bars: 1 µm.

The FDTD simulated field patterns (Figure 5.8 (a) and (c)) are in a good agreement with the morphology of re-solidified material (Figure 5.8 (b) and (d)) observed experimentally. Indeed, under the focusing conditions when the

modification area is smaller than the laser wavelength, the symmetric structure is slightly elongated, and the bridge-like structure along the polarization is produced (Figure 5.8 (b)). On the other hand, the bridge structure perpendicular to the polarization occurs when the beam is defocused (Figure 5.8 (d)). At the same time, the regions of the rim perpendicular to the bridge are modified, matching the intensity distribution visualized in numerical analysis (Figure 5.8 (c)).

5.3 Discussions and suggestions

The interaction of ultrashort laser pulses with silicon has been intensively studied by several authors [67,69,71,72]. And we are not the first to observe that single ultrashort laser pulse created the isotropic craters on silicon, Borowiec *et al.* found very similar structures on silicon using 130 fs pulses with energies ranging from 35 nJ to 1.9 μJ at 790 nm (Figure 5.9) [49]. The corresponding damage threshold defined by surface change observed through SEM is 150 mJ/cm^2, which is in the same fluence range as in our case (Figure 5.6). But they didn't perform any further experiments with double pulsed ultrashort laser irradiation.

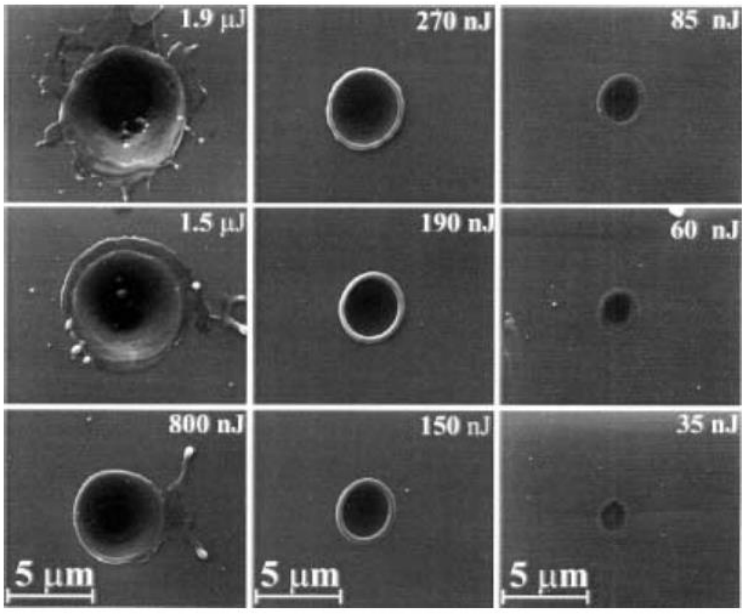

Figure 5.9 Silicon structures induced by linearly polarized single-pulsed femtosecond laser irradiation. Image source: A. Borowiec *et al.* [49].

In our experiment, the anisotropic structures were observed after double or multiple laser pulse irradiations. If we only pay attention to the rim region of the craters, it could be noticed that the intense field localized in that region distributes very similar within two cases (Figure 5.8 (a) and (c)). The rim part can be simplified as a combination of rectangular silicon oriented at different angles with respect to the polarization orientations.

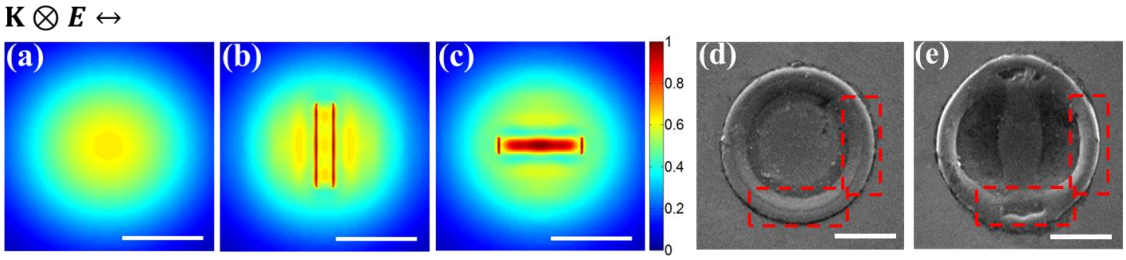

Figure 5.10 Electric field intensity distribution recorded within the FDTD simulation after the single pulse focused on (a) the silicon substrate surface, and the rectangular silicon block placed on the silicon substrate oriented (b) perpendicular and (c) parallel to the electric field direction. The color bar is normalized to 1. The scale bars: 1 μm. (d) and (e) topological SEM images.

The size of the rectangle used for the simulation was 1×0.2×0.05 μm^3 (length×width×height). For both rectangle orientations (Figure 5.10 (b) and (c)), the peak electric field intensity is about 56% higher than just focusing on a silicon substrate (Figure 5.10 (a)). Strong field enhancement can be observed over the rectangle when it is aligned parallel with the polarization direction (Figure 5.10 (c)). On the other hand, there is field enhancement localized only on the vertical edges of the rectangle when it is placed perpendicular to the polarization direction (Figure 5.10 (b)). This can be explained by the polarization dependence of the boundary conditions.

We could imagine that for the silicon block parallel to the electric field, the enhanced electric field would tend to split the structure into two parts (Figure 5.10 (c)). In the other case when silicon block is aligned perpendicular to the electric field, the structure was enhanced along its vertical edges (Figure 5.10 (b)). These deductions could be confirmed by comparing the AFM profiles (Figure 5.5 (c) and (g)) after single and double pulse irradiations. The rim was split at the tips of the bridge (Figure 5.10 (e)), and the rim height along the direction parallel to the beam polarization was increased by more than 150%, while along the perpendicular direction only by 60% compare with single pulse modification (Figure 5.5 (h)).

The boundary conditions algorithm can only explain the modifications appeared on the rim, but not the formation of centered bridge-like structure. The

explanation of the creation of such structure may be applied on the basis of an anisotropic near-field distribution dominated for different regions of structure within the surface-wave modes and the field coupling to the waveguided modes of the aperture.

Another curious thing is that what would happen if we treated the crystalline silicon with more pulses. The SEM profiles of the modification spots generated at laser fluence of 2.7 J/cm^2 with irradiation pulse number of N=1,2,3,4,5 and 6 are shown in Figure 5.11(a-f). The bridge-like structure perpendicular to the laser polarization appears after the second pulse irradiation. Afterwards, the whole crater is ablated and deformed (Figure 5.11(c-f)). However, the bridge-like structure remains in the middle of the crater, where the highest energy was deposited (Figure 5.11(c-f)). The development of the bridge-like structure follows a very reproducible manner in couple sets of experiments.

A sequence of periodic structures with a period of ~500 nm can be observed when horizontally polarized beam was implemented for scribing the silicon transversely (Figure 5.11(g)). Whereas, if the silicon was scribed along vertically direction, couple planes parallel to the beam moving direction are shown (Figure 5.11(g)). Similar results were also obtained by C. Hnatovsky *et al.* when scribing the silicon surface [59]. However, they didn't observe the bridge- like structure while drilling the silicon surface, as there were 2500 pulses imprinted.

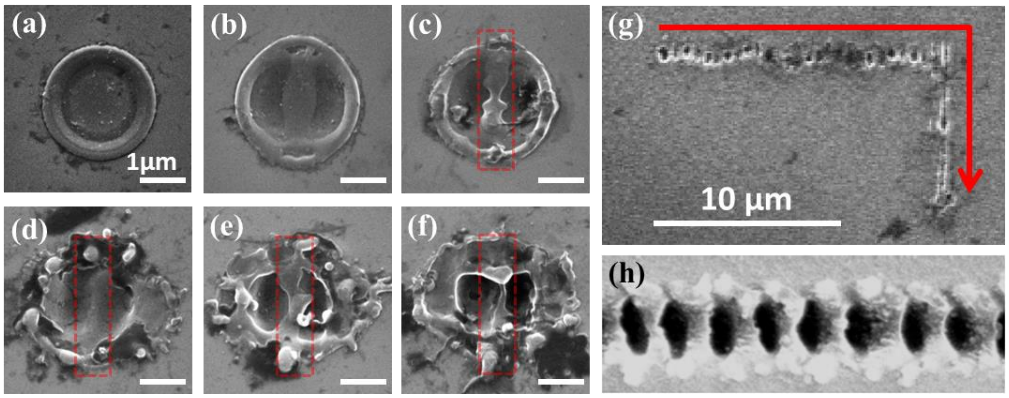

Figure 5.11 Pulse number dependence of the SEM profiles of the modification spot (a) N=1;(b) N=2;(c) N=3;(d) N=4;(e) N=5;(f) N=6. The scale bar is 1 μm. (g) The scribing in two directions using the same beam. The laser is horizontally polarized, and the repetitaion rate is 20 kHz. (h) The laser scribing SEM result. Image source: C. Hnatovsky *et al.* [59].

Interestingly, it was believed in C. Hnatovsky's paper [59] that the structures in Figure 5.11(h) were a low spatial frequency laser-induced periodic surface structure (LIPSS). Besides when scribing the silicon, we also obtained some periodic surface structures when irradiating the silicon with double-pulsed laser beam. Sequences of periodic structures with a period of ~1000 nm were observed perpendicular to the polarization direction (Figure 5.12 (a)-(d)). Compared to the modification induced by less energy (Figure 5.11(b)), the structures induced by 600nJ appear a much more irregular and irreproducible surface morphology. It seems that they are three different types of structural changes in different size regimes ($d < \lambda$, $\lambda < d < 5\lambda$ and $d > 5\lambda$).

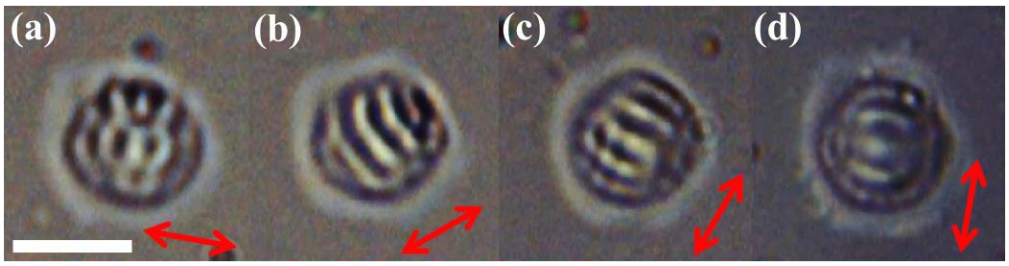

Figure 5.12 Optical microscope images of the silicon surface modified with (a-d) double pulses with four different polarizations indicated by arrows. Pulses with the energy of 600nJ were focused at 8 μm above the surface. The scale bars: 5 μm.

In conclusion, we have experimentally demonstrated the polarization sensitive structuring on a silicon surface by the linearly polarized femtosecond double pulses. The distribution of electric near-field becomes asymmetric and polarization dependent when the second pulse propagates through a circular crater structure produced by the first pulse. The phenomenon enables imprinting of optical microreflectors within the single pulse irradiation and is exploited for demonstrating the direct mapping of the near-field distribution within multi-pulse experiments. Polarization sensitive structuring on silicon can be used for the security marking or data storage applications.

Chapter 6: Femtosecond laser-induced nanogratings

As one of the main objectives of this thesis is to store data based on polarization sensitive ultrafast laser material modifications, I will firstly introduce the proposed mechanisms of ultrafast laser material modifications in transparent materials. The propagation of ultrafast laser pulses, ionization and laser matter interaction in transparent materials will be discussed.

Afterwards, the formation mechanisms of nanogratings will be discussed in this chapter. Despite several attempts to explain the physics of the peculiar self-organization process, the formation of nanogratings still remains debatable. In the following section, the properties of nanogratings and its applications are introduced. Later in this chapter, optimal parameters such as objective lens, laser power, number of pulses and pulse duration for data recording will be determined by sets of experiment. Lastly, I will discuss how induced stress influences the birefringent retardance value of nanogratings.

6.1 Ultrafast laser material modification in transparent material

The propagation of an electromagnetic field follows the Maxwell equations below:

$$\nabla \cdot \mathbf{D} = \rho \qquad \text{Equation 6-1}$$

$$\nabla \cdot \mathbf{B} = 0 \qquad \text{Equation 6-2}$$

$$\nabla \times \mathbf{E} = -\frac{\partial \mathbf{B}}{\partial t} \qquad \text{Equation 6-3}$$

$$\nabla \times \mathbf{H} = \mathbf{J} + \frac{\partial \mathbf{D}}{\partial t} \qquad \text{Equation 6-4}$$

where $\mathbf{D}$ is the electric displacement field or flux density, $\mathbf{B}$ is the magnetic flux density, $\mathbf{E}$ and $\mathbf{H}$ are the electric and magnetic fields, ρ, $\mathbf{J}$ are the total free charge density and total free current density. When the electromagnetic field propagates in a nonmagnetic medium, ρ and $\mathbf{J}$ are zero.

When laser pulses propagate in a medium, the refractive index of a material changes by the electric field of the light itself. This phenomenon is called optical Kerr effect. The refractive index n can be derived from:

$$\mathrm{n} = n_0 + n_2 I \qquad \text{Equation 6-5}$$

where n_2 is the second-order nonlinear refractive index and I is the laser intensity. The optical Kerr effect leads to nonlinear optical effects such as self-focusing and self-phase modulation.

Self-focusing happens when the refractive index of the medium in the irradiation region increases due to the Kerr effect (Figure 6.1). According to Equation 6-5, the value of the non-linear refractive index ($\Delta \mathrm{n}$) is proportional to the laser intensity (I). Therefore, the strength distribution of the non-linear refractive index has similar profile as the laser intensity (Figure 6.1(a)). Material in this

region functions as a focusing lens and focuses the incoming laser pulses (Figure 6.1(b)). Thus, the peak intensity of the beam in the self-focused region keeps increasing while the beam propagates in the medium. This process can be terminated when defocusing effects or material damage takes place.

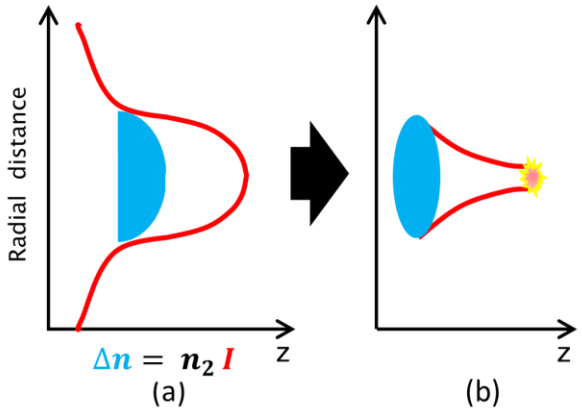

Figure 6.1 Schematic illustration of (a) the non-linear refractive index distribution generated by a laser beam and (b) induced focusing lens.

At a critical power, filament is formed when self-focusing balances diffraction after the focal position. The critical power can be derived from [73]:

$$P_{cr} = \frac{(0.61)^2 \pi \lambda^2}{8 n_0 n_2} \qquad \text{Equation 6-6}$$

where λ is the laser wavelength in vacuum. n_0 is 1.47 for fused silica at 1030nm.

The nonlinear refractive index for fused silica is $(3.0 \pm 0.35) \times 10^{-16}$ cm^2/W at 527nm and $(2.74 \pm 0.17) \times 10^{-16}$ cm^2/W at 1053 nm [74]. Therefore, the critical power for 1030 nm is in the range of 3.6 MW to 4.0 MW. For a typical Yb:KGW laser pulse with 280 fs duration, the pulse energy at critical power is around 1.2 μJ. The amount of self-focusing can be estimated by the ratio of the laser peak power to the critical power. Besides self-focusing, the ionization process of the material generates free electron plasma, which leads to a negative index change and prevents further self-focusing.

The band gap of fused silica is 9 eV (E_g) [75], whereas the photon energy is only 1.2 eV ($\hbar\omega$) at 1030 nm wavelength. A single photon with such low energy

cannot be absorbed in the linear-response regime. However, if the light intensity is sufficiently high, the laser pulse at 1030 nm wavelength can transfer energy to the electrons by nonlinear ionization. Two classes of such nonlinear processes are involved: nonlinear photoionization and avalanche ionization [30]. Photoionization is the process in which an ion is formed by photon induced electron excitation. Depending on laser intensity and laser wavelength, there are two regimes in which either multi-photon or tunnel ionization takes place.

Multi-photon ionization tends to happen at lower laser intensities and shorter wavelengths (still insufficient for single photon ionization). In this regime, several photons of energy lower than the ionization threshold are absorbed by the electrons simultaneously (Figure 6.2). When the intensity of the electric field is stronger and a longer wavelength is applied, tunnel ionization occurs (Figure 6.2). In this case, the potential barrier is distorted drastically, which leads to the reduction of the length of the barrier that electrons have to pass. As a result, the electrons can tunnel through the barrier and escape from the atom or molecule easily.

To determine which of the two, tunnel or multi-photon ionization occurs, the adiabatic parameter γ is calculated by the following equation [76]:

$$\gamma = \frac{\omega}{e}\left[\frac{m_e c n \varepsilon_0 E_g}{I}\right]^{\frac{1}{2}} \qquad \text{Equation 6-7}$$

where ω - $2\pi c/\lambda$ laser pulsation, e – charge of the electron, m_e – reduced mass of the electron, c – the velocity of light, n – refractive index of the material, ε_0 – permittivity of free space, E_g – band gap of the material, I - intensity of the laser. When γ is smaller than approximately 1.5, the photoionization is dominated by tunneling process. On the contrary, when γ exceeds 1.5, multi-photon process dominates. An intermediate regime containing both tunneling and multi-photon ionization exists when the adiabatic parameter is around the value of 1.5 (Figure 6.2).

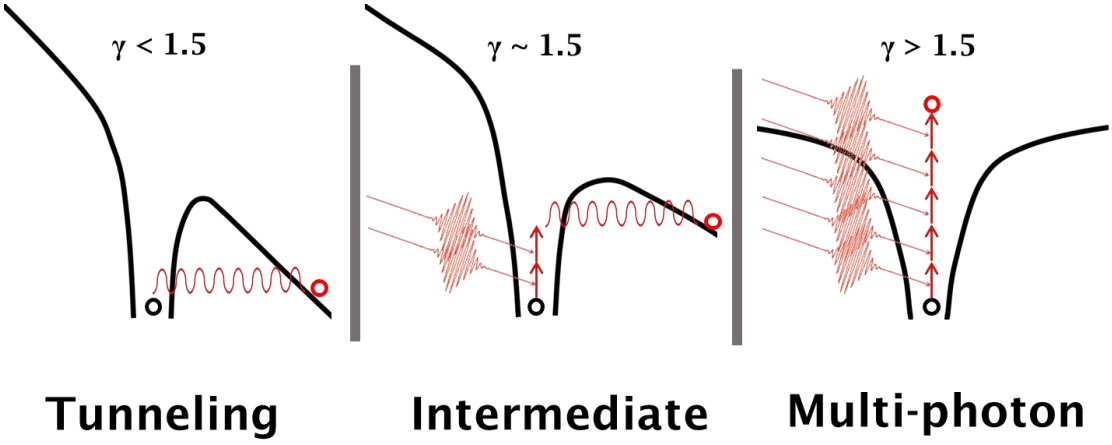

Figure 6.2 Schematic diagrams of three different types of non-linear absorption mechanisms. The red dots represent ionized electrons.

The initial free electrons generated by multi-photon and tunneling ionization can gain further energy by absorbing incoming photons from the laser light. When the energy of the electron reaches the energy of the band gap, impact ionization occurs. In this process, the electron with the energy over the band gap can relax to a lower energy by transferring a part of its energy to another electron in the valence band, resulting in two electrons in the conduction band. Such process will continue and increase the electron density in the conduction band as long as the incoming electromagnetic field is present.

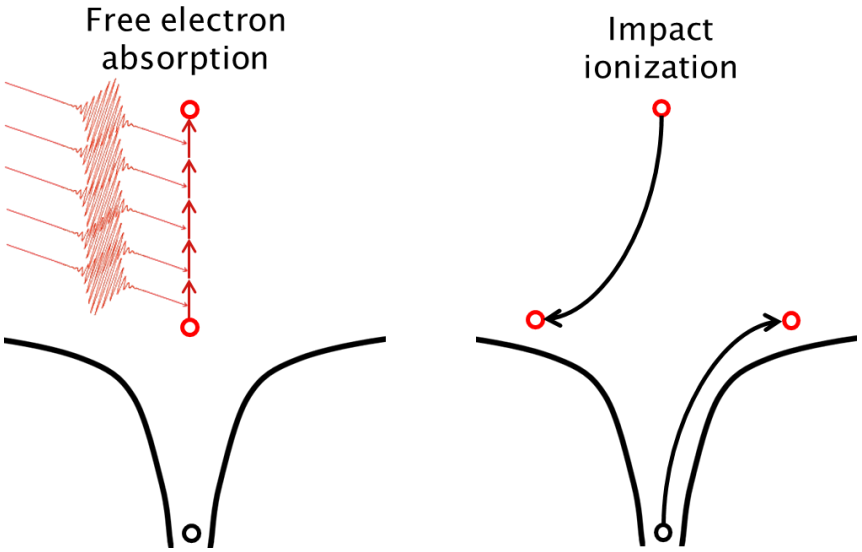

Figure 6.3 Schematic diagrams of avalanche ionization. Left: Free electron absorption. Right: Impact ionization.

The electron density generated through the avalanche ionization can be determined by the following equation:

$$n_{av}(t) = n_0 2^{w_{imp} \cdot t} \qquad \text{Equation 6-8}$$

where n_0 is initial electron density, w_{imp} is the probability of the impact ionization.

During the laser irradiation, energy is absorbed by the electrons through the nonlinear process mentioned above. Then, the energy from the hot electrons can be transferred into the lattice via electron-phonon scattering. For the fused silica, the typical electron-phonon coupling time is in the picosecond range [77]. Therefore, during a femtosecond laser pulse, the electrons are heated much faster than they can cool down by electron-phonon scattering. After the pulse has gone by, the energy is released to the lattice on a time scale much shorter than the heat diffusion time [78]. Therefore, the heat affected region is limited to the focal irradiated area and its vicinity, leaving a localized permanent modification in material.

6.2 Formation of laser induced nanogratings

Three types of localized permanent modification can be induced by ultrafast laser in the bulk of fused silica. Depending on pulse energy and pulse duration, there are positive refractive index change (Type 1) [4,79], nanogratings (Type 2) [9] and microvoids (Type 3) [50] (Figure 6.4).

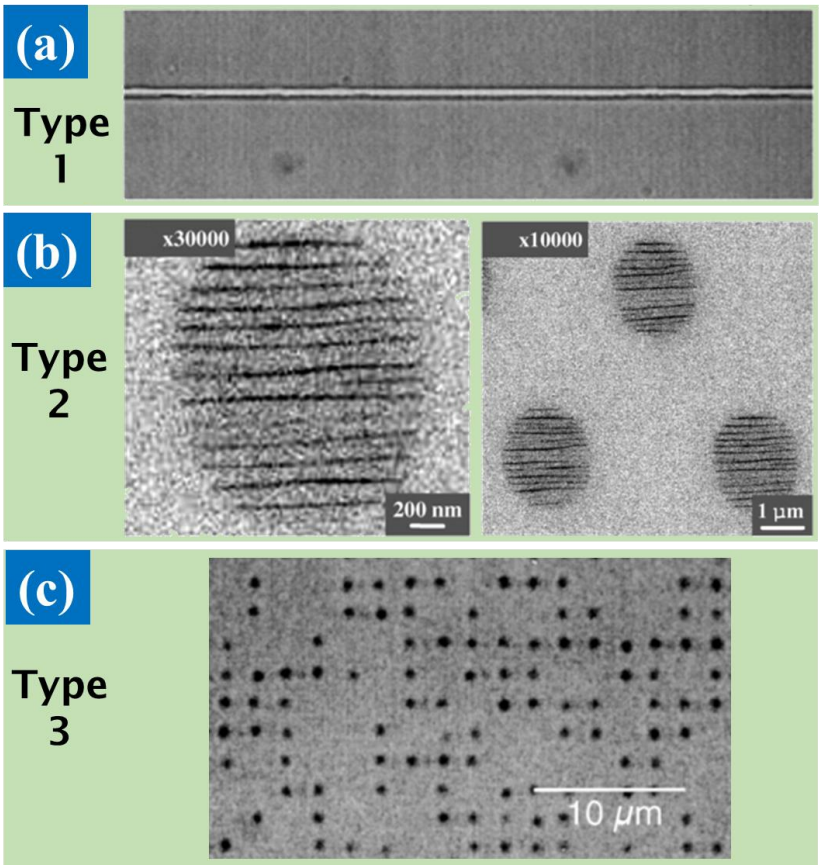

Figure 6.4 Three types of localized permanent modification: (a) positive refractive index change (b) nanogratings and (c) microvoids. Image source: (a) K. Miura *et al.* [79], (b) Y. Shimotsuma *et al.* [9], (c) E. Glezer *et al.* [50].

Previous experimental study has indicated that three types of modifications can be induced at different pulse energies when laser pulse is shorter than 200 fs [80]. The modification types change from type 1 to type 2 and then type 3 with the increase of the pulse energy (Figure 6.5). At longer pulses, the permanent positive refractive index change (type 1) cannot be introduced into the fused silica, however, the type 2 modification appears at relatively low energies (Figure 6.5).

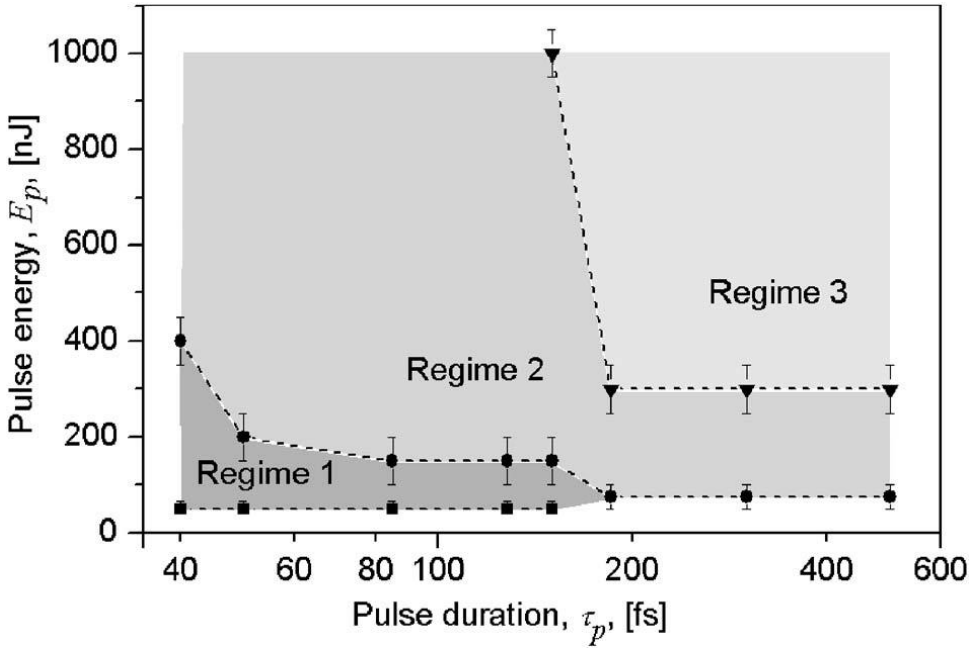

Figure 6.5 Pulse energy vs pulse duration for three regimes of femtosecond laser modification in fused silica. Regime 1, 2, 3 corresponds to type 1, 2, 3 modification respectively. Image source: C. Hnatovsky *et al.* [80].

The earliest work related to the type 2 modification can be traced back to the late 1990s when anisotropic modification was observed in fused silica glass after femtosecond laser irradiation [44,81]. It was later revealed that such an anisotropy was due to a self-assembled periodical structural modification (called nanogratings) generated in the bulk of irradiated medium [9]. Unlike the LIPSS, which can be seen on many dielectrics and metal surface [63], the nanogratings can be observed only in the bulk of couple materials: fused silica [9], sapphire [61], tellurium oxide [82], borosilicate and ULE glasses [83,84]. Among them, fused silica is the most widely used material for generating nanogratings.

The nanogratings has two periodicities: one perpendicular to the direction of the polarization and another parallel to the light propagation direction [85] (Figure 6.6). The gratings perpendicular to the polarization direction has a period in the range of 100-300nm depending on experimental conditions [86]. Simultaneously, the gratings has a second period evolves from the top of the structure to the tail (Figure 6.6). The initial period of the second periodicity is close to the light wavelength in the material (λ_0/n) [85].

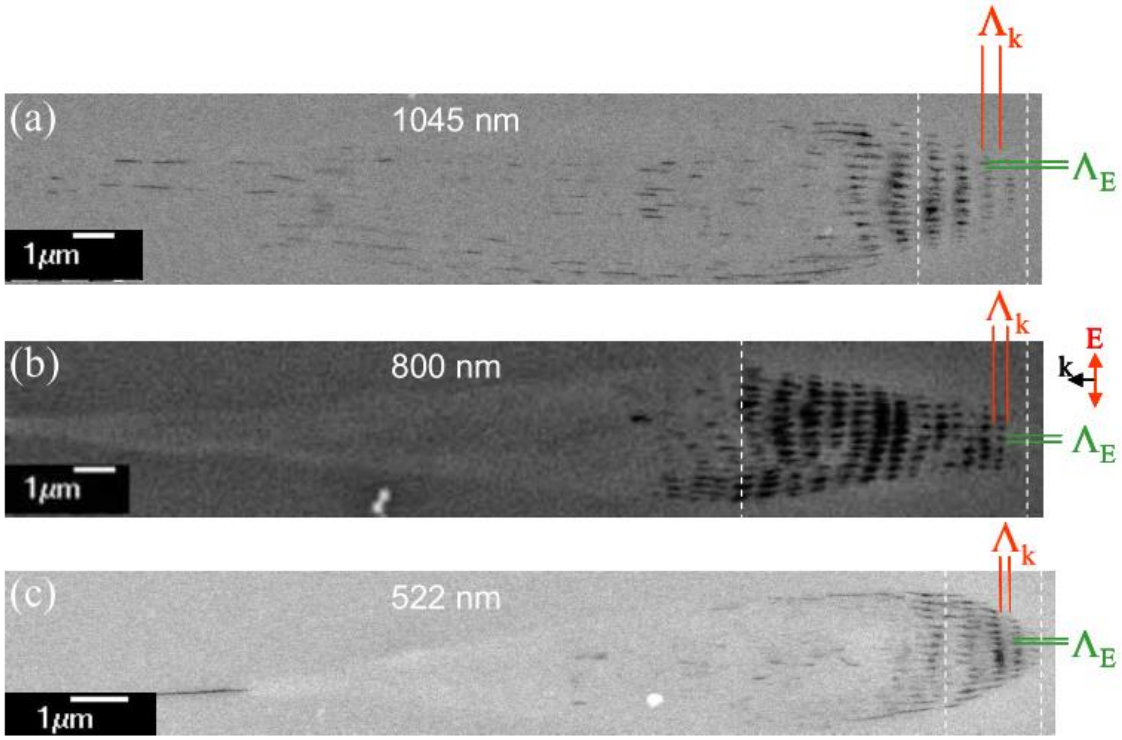

Figure 6.6 SEM profiles of nanogratings induced by three different wavelengths (a)1045nm, (b)800nm,(c)522nm of the irradiated femtosecond laser pulses. E and k are electric field and wave vector of the writing laser beam. Image source: W.Yang *et al.* [85].

The explanations of nanogratings formation are mainly focused on the periodicity perpendicular to the beam polarization direction. Many attempts were made to explain the formation mechanism of the peculiar nanostructure [9,87,88]. The first explanation was based on an interference of the induced bulk electron plasma wave with the incident light field [9]. During the laser irradiation, multi-photon ionization leads to high electron density, the induced plasma absorbs the laser energy through one-photon absorption model [89]. The absorbed energy excites an electron plasma wave which can couple with the incident light wave if the plasma wave propagates in the plane of light polarization. Inhomogeneities introduced by electrons moving in this plane most likely lead to the initial coupling [44]. The periodic structure, generated by the interference, further enhances this coupling, leading to a periodic distribution of plasma concentration. Later, this distribution is frozen in the bulk of the medium. The periodicity of the nanogratings can be determined from the equation below:

$$\boldsymbol{k}_{ph} + \boldsymbol{k}_{gr} = \boldsymbol{k}_{pl}. \qquad \text{Equation 6-9}$$

where $\boldsymbol{k}_{ph} = \omega n/c$ is photon wavevector, ω is the angular frequency, n is the refractive index, c is speed of light. $\boldsymbol{k}_{gr} = 2\pi/\Lambda_{gr}$ is gratings wavevector, Λ_{gr} is gratings period, $\boldsymbol{k}_{pl} = \omega_{pl}/v_{pl}$ is plasma wavevector, $v_{pl}$and ω_{pl} is the speed and angular frequency of the plasma wave.

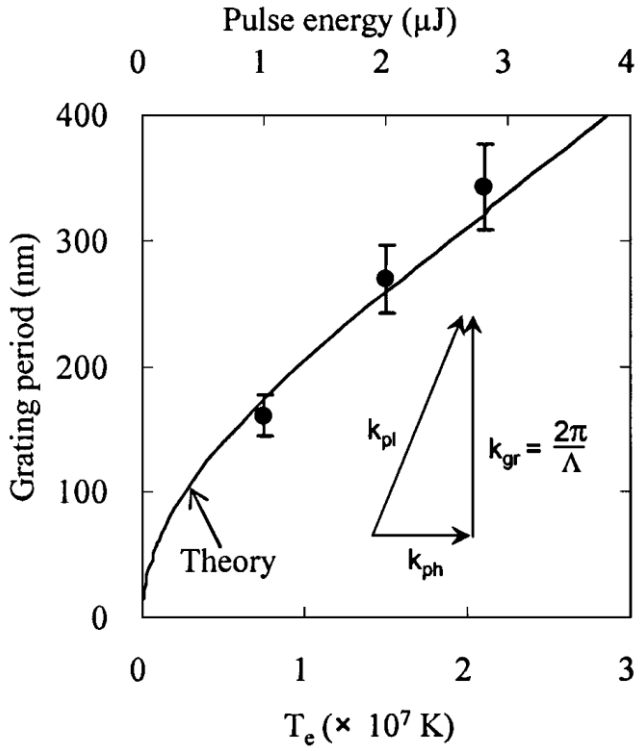

Figure 6.7 Dependence of nanogratings period on electron temperature. Inset is the wavevector matching diagram. Image source: Y. Shimotsuma *et al.* [9]

The analytical expression can be obtained by considering energy conservation condition, momentum conservation relation, and dispersion relation [9]:

$$\Lambda_{gr} = \frac{2\pi}{\sqrt{\frac{1}{T_e}\left(\frac{m_e\omega^2}{3k_B} - \frac{e^2\eta_e}{3\varepsilon_0 k_B}\right) - k_{ph}^2}} \qquad \text{Equation 6-10}$$

where m_e is the electron mass, e is the electron charge, η_e is the electron density, T_e is the electron temperature, and k_B is Boltzmann constant.

From the Equation 6-10, it can be obtained that the period of nanogratings should increase with an electron density η_e and electron temperature T_e. According to the equation, ultrashort laser pulses with a central wavelength of 800 nm should induce the nanogratings with a period of 150 nm when $T_e = 5 \times 10^7$ K and $\eta_e = 1.75 \times 10^{21} cm^{-3}$ [9]. However, the maximum of the electron temperature is determined by the band gap of the material. For the case of silica glass, the electron temperature should not exceed 1.1×10^5 K. Additional energy from the hot electrons will be dissipated through impact ionization as mentioned in the previous section.

Thus, the formation mechanism based on interference was adapted after considering two-plasmon decay [89,90]. Compared to the first explanation, the new mechanism involves that an incident laser photon splits into two plasmons of about half of the photon energy. The two plasmon waves of the same frequency propagate in opposite directions in the plane of light polarization and meet Cherenkov's mechanism of momentum conservation [90]. This phenomenon appears when plasma density reaches quarter of the critical level ($\frac{\eta_{cr}}{4} \sim 4 \times 10^{20} cm^{-3}$). Such plasma density is more close to the density under experimental conditions. Due to the coupling of plasma wave and incident light, the generation $3/2\omega$ harmonic should be observed as a sign of two-plasmon decay.

The third explanation of nanogratings formation is by nanoplasma formation [87]. Natural inhomogeneities in the dielectric such as color centres and defects lead to the generation of localized inhomogeneous nanoplasma. Anisotropic growth of the initial spherical nanoplasma was expected due to the local field enhancement at the boundary (Figure 6.8). The electric fields at the equator and poles of the spherical nanoplasma are determined based on the equations below [87]:

$$E_E = \frac{3E}{\varepsilon' + 2} \qquad \text{Equation 6-11}$$

$$E_P = \frac{3\varepsilon' E}{\varepsilon' + 2} \qquad \text{Equation 6-12}$$

where E is the electric field, ε' is the ratio of the real parts of the electric permitivities for the nanoplasma sphere and the dielectric medium.

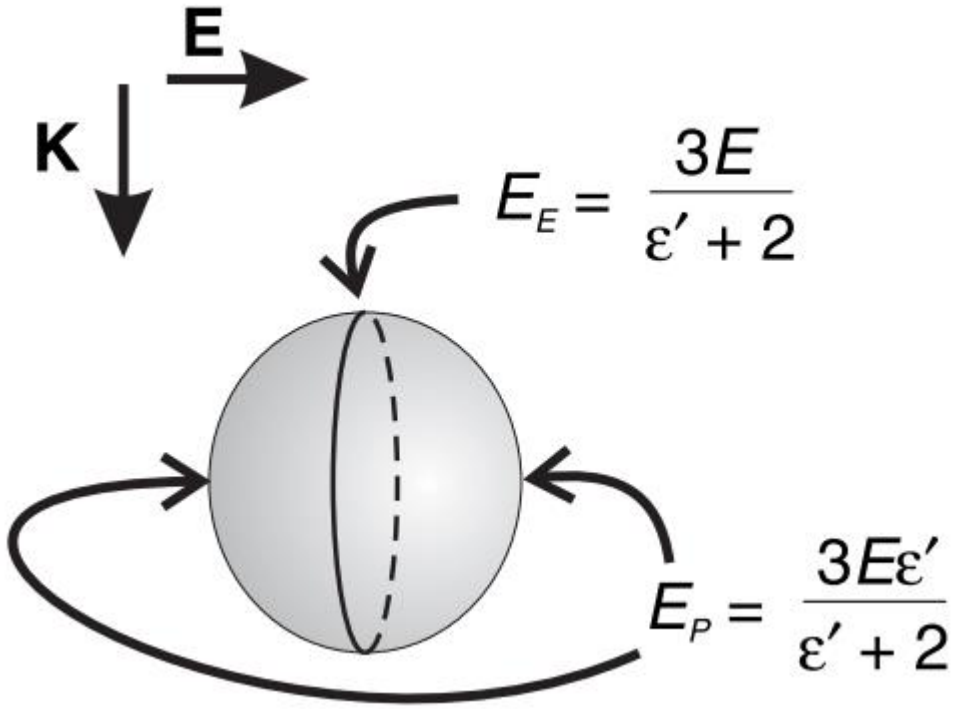

Figure 6.8 Schematic illustration of the local field enhancement at the boundary of a nanoplasma. K indicates the propagation direction of the laser beam, E is the electric field. Image source: V. Bhardwaj *et al.* [87].

When ε' is smaller than 1 (the plasma density is smaller than the critical density), the local field at the equator is stronger than the field at the poles of the nanoplasma sphere. The enhanced electric field at the equator leads to the formation of nanoplane perpendicular to the beam polarization direction. However, this mechanism fails to explain the formation of nanoplanes when the plasma density is beyond the critical density (i.e. when $\varepsilon' > 1$) [91].

The three mechanisms illustrated above are all related to the generation of plasma and its response with laser beam. However, they fail to explain the formation of nanogratings along beam propagation direction (Figure 6.6) [92].

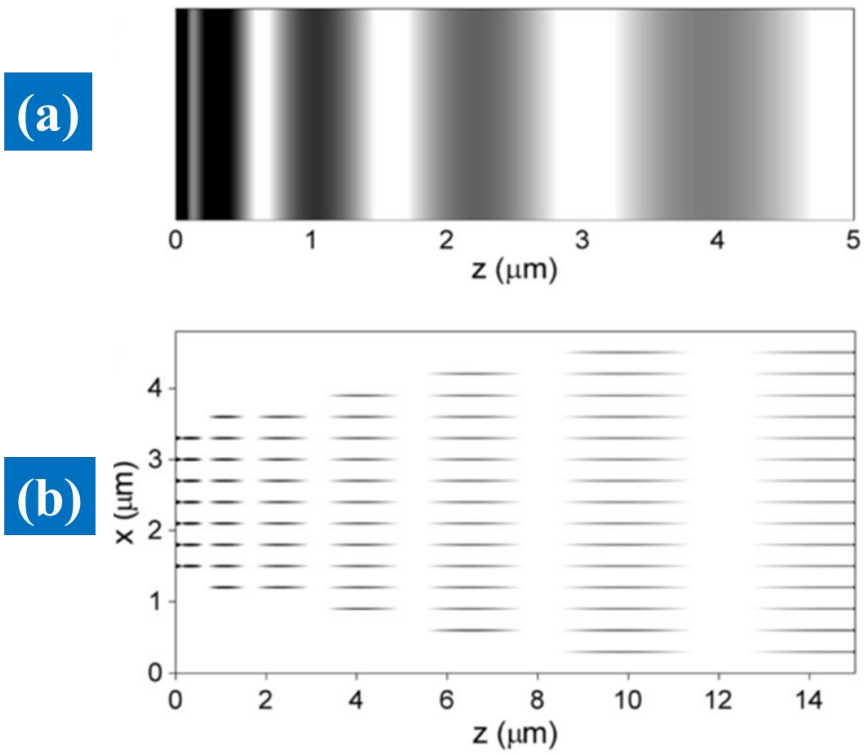

Figure 6.9 Theoretical simulation of the formation of the grating (a) zoomed in the z direction and (b) in the x and z direction. Image source: M. Beresna [92].

Therefore, another mechanism was proposed based on interference, attractive interaction and self-trapping of exciton-polaritons [92]. Exciton-polaritons are mixed light-matter quasiparticles from strong coupling of excitons and photons. Propagation of exciton-polaritons can be seen as a series of virtual absorption and emission processes. In the fused silica glass, the two dispersion branches of exciton-polaritons may be excited simultaneously by multi-photon absorption [92]. The interference of two propagating exciton-polaritons leads to the formation of grating structures. The excitons turn into indirect states after decoupling from light due to phonon assisted relaxation [93]. The excitons at indirect states can be easily trapped and exist for several microseconds or longer [94]. Therefore, the trapped indirect excitons can image the grating structures generated by two exciton-polaritons interference [94]. The interference of two exciton-polaritons leads to formation of the grating and determines the periodicity along beam propagation direction (Figure 6.9).

The self-trapped excitons can interact with fused silica and generate molecular oxygen following the mechanism below:

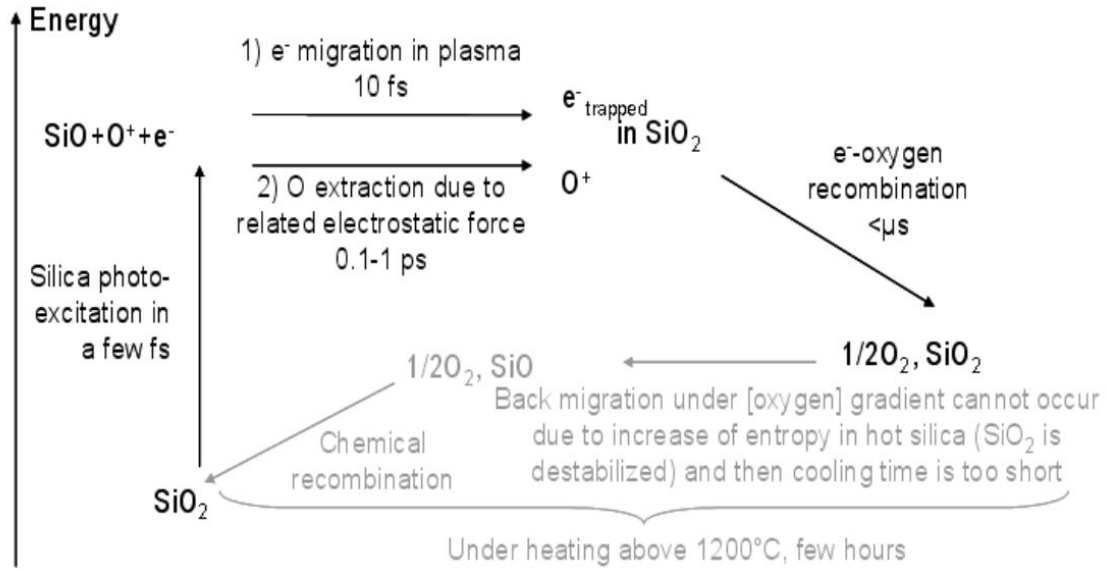

Figure 6.10 Mechanism of molecular oxgen generation and related phenomena. Image source: J. Canning [95]

Nanopores filled by molecular oxygen are generated in the locations where high density of self-trapped excitons is present. The existence of molecular oxygen was observed in GeO_2 glass after femtosecond laser irradiation [96]. In addition, the laser induced nanopores in fused silica was confirmed by A. Champion and Y. Bellouard [97]. The grating patterns are generated by agglomerations of these silica nanopores [92].

All of the above explanations of nanogratings formation are under the condition of single pulse irradiation. However, it is well recognized that nanogratings can only be generated after multiple pulses irradiation. Such behaviour reveals that some accumulation processes must take place during the nanogratings formation. Therefore, direct experimental observation of the pulse-to-pulse evolution of nanogratings formation would be very beneficial.

6.3 Properties and applications of nanogratings

Nanogratings have many peculiar properties such as being rewritable [98], self-replicating [86] and thermal stability [99]. But the main characteristic of nanogratings is form birefringence [9,81]. The form birefringence is due to either rods, spheres or platelets with one refractive index suspended in a medium with a second refractive index [100]. For the case of nanogratings, they can be seen as parallel planes with different refractive index which lead to form birefringence (Figure 6.11(b)).

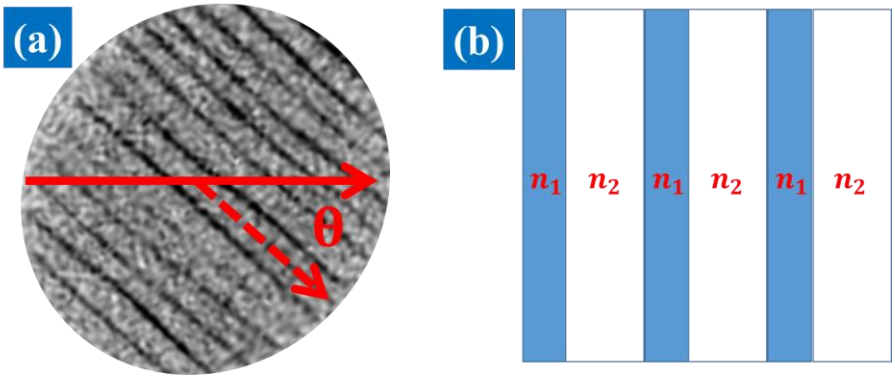

Figure 6.11 (a) SEM image of nanogratings. (b) Schematic illustration of birefringence caused by nanogratings. θ is the azimuth of the slow axis.

The refractive indices of nanogratings for ordinary n_0 and extraordinary n_e can be simplified to equations below (Figure 6.11(b)) [100]:

$$n_o = [f n_1^2 + (1-f) n_2^2.]^{1/2} \qquad \text{Equation 6-13}$$

$$n_e = \left[\frac{n_1^2 n_2^2}{f n_2^2 + (1-f) n_1^2}\right]^{1/2} \qquad \text{Equation 6-14}$$

where f is the filling factor, n_1 and n_2 are refractive indices for platelets forming the nanogratings (Figure 6.11).

The relation of ordinary and extraordinary refractive indices can be derived from Equation 6-13 and Equation 6-14:

$$n_e^2 - n_o^2 = -\frac{f(1-f)(n_1^2 - n_2^2)^2}{f n_2^2 + (1-f) n_1^2} \leq 0 \qquad \text{Equation 6-15}$$

Therefore, the form nanogratings always function as a negative uniaxial crystal. The value of $n_e - n_o$ is in the range of -2 to -4 x10^{-3} [99], which is of the same order of magnitude as positive birefringence in crystalline quartz 9x10^{-3} [99].

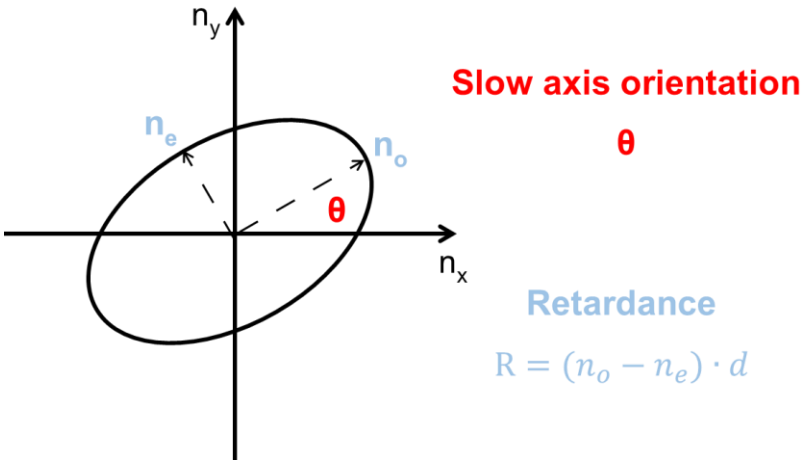

Figure 6.12 The form birefringence can be characterized by slow axis orientation and phase retardance. d is the thickness of birefringent structure.

The form birefringence can be characterized by phase retardance and slow axis orientation (Figure 6.12(a)). Additionally, these two values can be individually manipulated by intensity and polarization of the incident beam.

Therefore, it enables the fabrication of customized birefringent optical elements by ultrafast laser direct writing. The induced birefringence in ULE is equivalent to fused silica glasses at longer pulses, but much smaller when laser pulse is shorter than 200 fs [83]. And the form birefringence in borosilicate glass has only 12% phase retardance compared to fused silica glass [83]. Among all materials, fused silica is the best option for form birefringent applications.

Many devices such as Fresnel zone plate [101], cylindrical vector beams converter [102], airy beam converter [103] and polarization sensitive camera [104] have been fabricated by manipulation of the nanogratings induced form birefringence.

6.4 Laser writing parameters

In order to manipulate the birefringent signal of modification spots, firstly accurate laser parameters have to be defined. Parameters namely, objective lens, laser power, number of pulses and pulse duration determine the structure type and strength of birefringence.

Large numerical apertures immersion objective can focus the beam at a tight spot and compensates refractive index mismatch at the surface of the material. Therefore, a modification with small volume can be achieved, which is essential for 5D optical recording as more data can be stored in a limited space if a single memory voxel occupies less volume. As a result, a water immersion objective ($\mathrm{NA} = 1.2$, $\mathrm{NA_{eff}} \sim 0.75$ from $\mathrm{NA_{eff}} = \mathrm{n}\frac{D}{2f}$, where n is the refraction index, D is the diameter of the beam, f is focal length;) with aberration correction from 130μm to 210μm was chosen. It allows the reduction of the spot length down to 2μm (Figure 6.13).

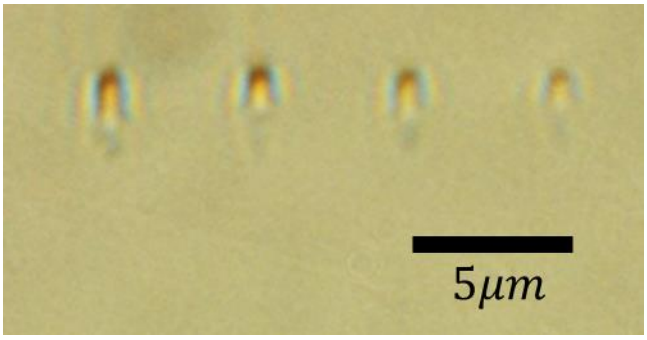

Figure 6.13 Microscope images of spot structure fabricated in fused silica observed from side. The laser parameters were: 30-40nJ/pulse, 1030 nm, 280 fs, 200 kHz and 400 pulses.

The experiments were performed with Pharos laser operating at 1030nm and the repetition rate was set to 200 kHz. An internal pulse stretcher-compressor was implemented to stretch pulse duration ranging from 280fs to 3.5ps. The horizontally polarized beam was focused with a water immersion objective ($\mathrm{NA} = 1.2$, $\mathrm{NA_{eff}} \sim 0.75$) 130μm underneath the surface of a glass sample. The structures were later analysed with the Abrio birefringence measurement system (Figure 2.3).

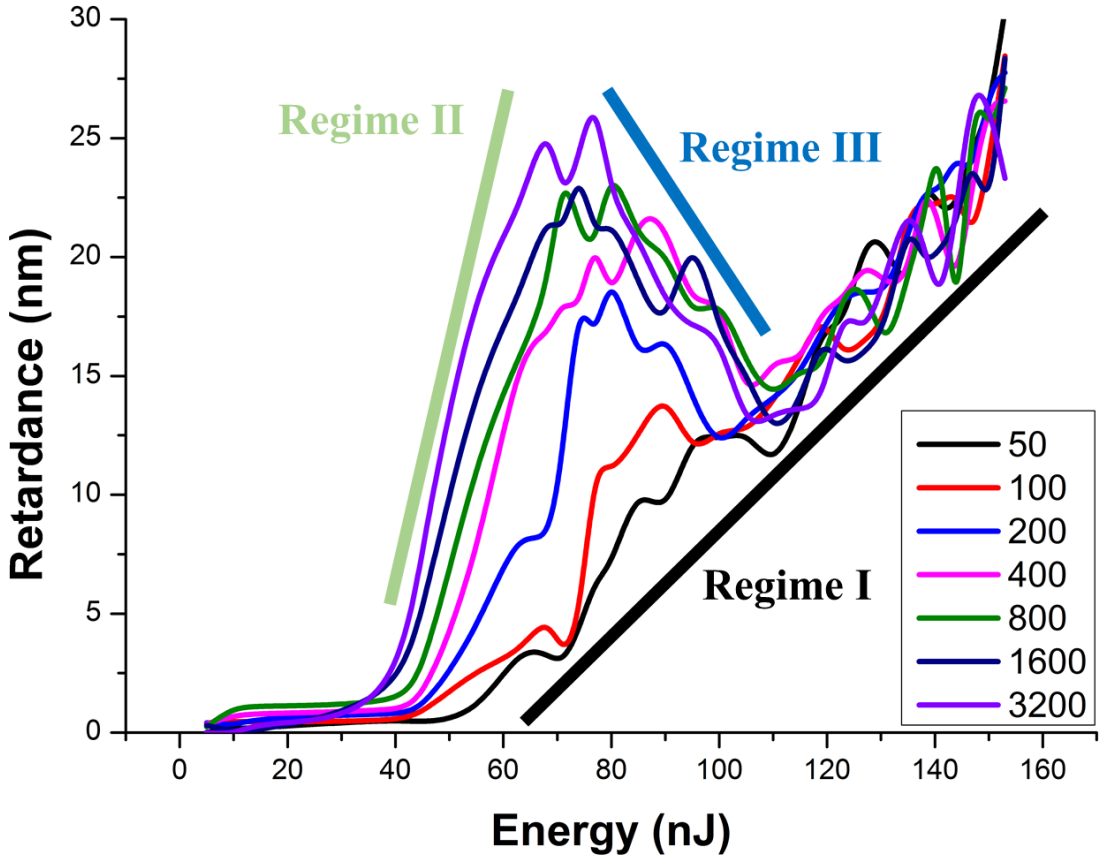

Figure 6.14 Retardance dependence of birefringent spots on laser energy and number of pulses at 280fs pulse duration.

In order to observe the influence of number of pulses on the induced birefringent spots, a set of dots (there were 5 dots in each condition) was written in fused silica with the pulse energy ranging in steps from 5nJ to 150nJ and number of pulses ranging from 50 to 3200. The pulse duration was set to 280fs. The results indicate strong dependence on energy levels and number of pulses. The tendency of the averaged retardance value of each condition was revealed by several spline fitting curves in Figure 6.14. The standard deviations of the measured values are around 15%. The fluctuation is caused by the limited number of measurement CCD pixels per each modification spot. If high NA microscope objective lens and sub-micron-sized CCD pixels are employed to the measurement system, correspondingly, the standard deviations should be reduced.

In Regime I, the number of pulses was insufficient to form proper nanogratings, the main contribution of phase retardance came from induced stress around the modification spots.

In Regime II, the nanogratings were well formed by the sufficient number of pulses. The increase of retardance can be observed while increasing energy or number of pulses (Figure 6.14). This prominent characteristic makes this regime ideal for 5D optical storage as the strength of phase retardance can be manipulated by changing energy levels.

In Regime III, where the pulse energy was even higher, the strength of phase retardance starts to drop (Figure 6.14). It reduces to the minimum value when the pulse energy is around 110nJ. The distinct growth tendency of phase retardance for 50 pulses indicate that there was no generation of nanogratings for such low number of pulses but only laser-induced stress.

We compare the results from all cases of different pulse numbers, and 400 is selected as the number of pulses for 5D optical memory recording. With such number of pulses, the modifications can provide sufficient strength of retardance and have minor fluctuations of the birefringent signal.

Second, we need to decide which pulse duration should be implemented for 5D optical memory writing. A set of dots was written in fused silica with the pulse energy ranging in steps from 5nJ to 150nJ and pulse duration ranging from 280fs to 4.5ps (Figure 6.15). The pulse duration for 5D optical recording was set as 280fs due to shorter pulse gives higher phase retardance according to the profile in Figure 6.15.

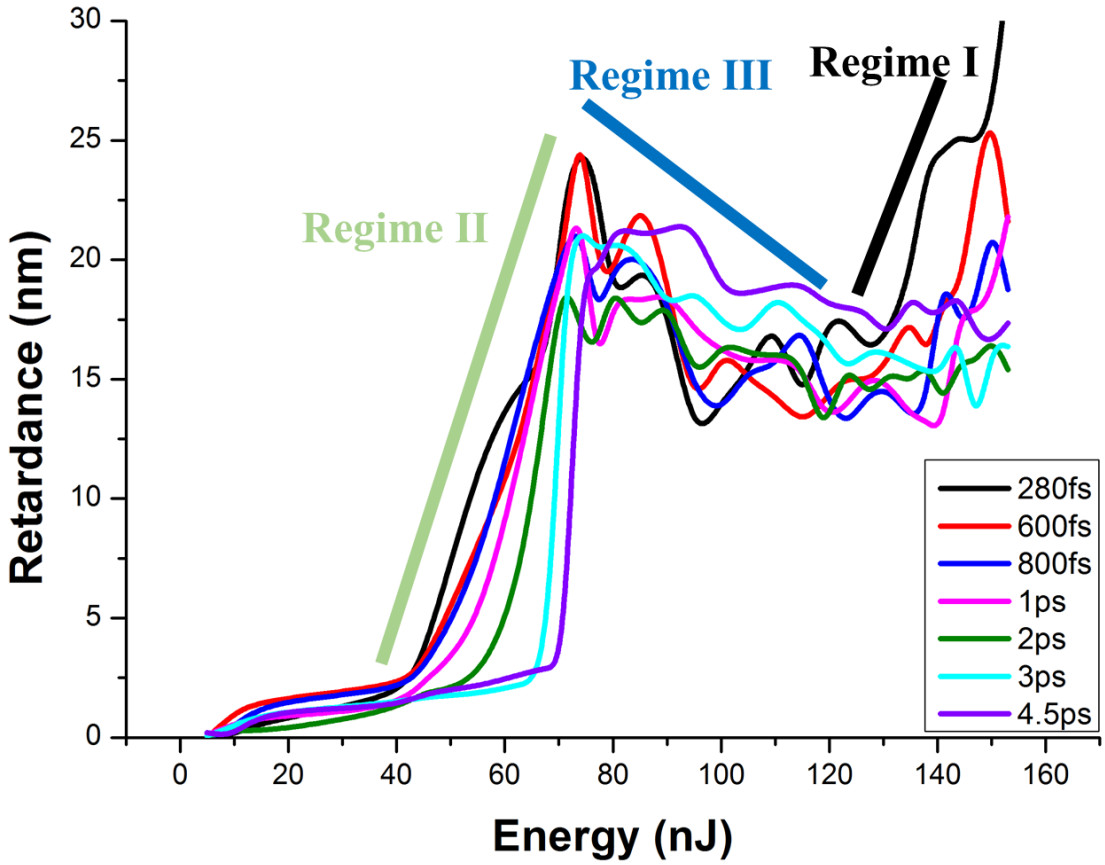

Figure 6.15 Retardance dependence of birefringent spots on laser energy and different pulse durations with 400 pulses.

The measurement results indicate that the energy threshold of the form birefringent modification depends on pulse duration (Figure 6.15). The phenomenon that modification threshold is higher at longer pulse duration is expected [78]. We can see that the strength of retardance starts to develop at the lowest energy when the pulse duration is 280fs. In this case, there is wide range of energy levels which can be chosen in order to manipulate the values of retardance. Furthermore, low threshold for birefringent modification means a laser with fixed power can be split into more number of beam spots when multiple beam spots approach is employed in 5D optical memory. Therefore, conclusion can be drawn that laser with 280fs pulse duration should be implemented for 5D optical data storage system.

6.5 Stress-induced birefringence around laser direct-written spots

Recent studies suggest that nanogratings are self-organized planar structures, which consist of a porous material [95,105]. The porous regions of nanogratings lead to volume expansion of the material and induce stress around the structures. Further study indicates that the distribution of such induced stress depends on the nanogratings orientation, i.e. laser polarization [105]. Additionally, another research shows that the pressure of the stress depends on laser parameters such as energy per pulse [106] However, the generated stress in fused silica leads to birefringence [105–108], resulting in undesired birefringence properties.

Recent study indicated that the stress induced by laser-modified lines depends on the orientations of lamellae in regard to the laser writing direction (Figure 6.16 (left)) [105]. Similarly, the stresses are generated around birefringent spot horizontally and vertically (Figure 6.16 (right)). Such stresses induce birefringence have the phase retardance following this equation [105]:

$$R = T * C * (\sigma_1 - \sigma_2) \qquad \text{Equation6-16}$$

where R is the phase retardance, T is the thickness of the sample, C is the stress optic coefficient and is around $3.48 \times 10^{-12} Pa^{-1}$ at 1030nm and $(\sigma_1 - \sigma_2)$ is the difference of principal stress.

The stresses push the material from the modification region to the horizontal and vertical surroundings (Figure 6.16 (right)). Therefore, the materials are more compressed along the directions where the pressure applied (Figure 6.16 (right)). Such directions are equivalent to slow axis orientations as material has higher effective refractive index along these compressed directions. Thus, we can conclude that the slow axis orientation of stress-induced birefringence is parallel to the direction of stress.

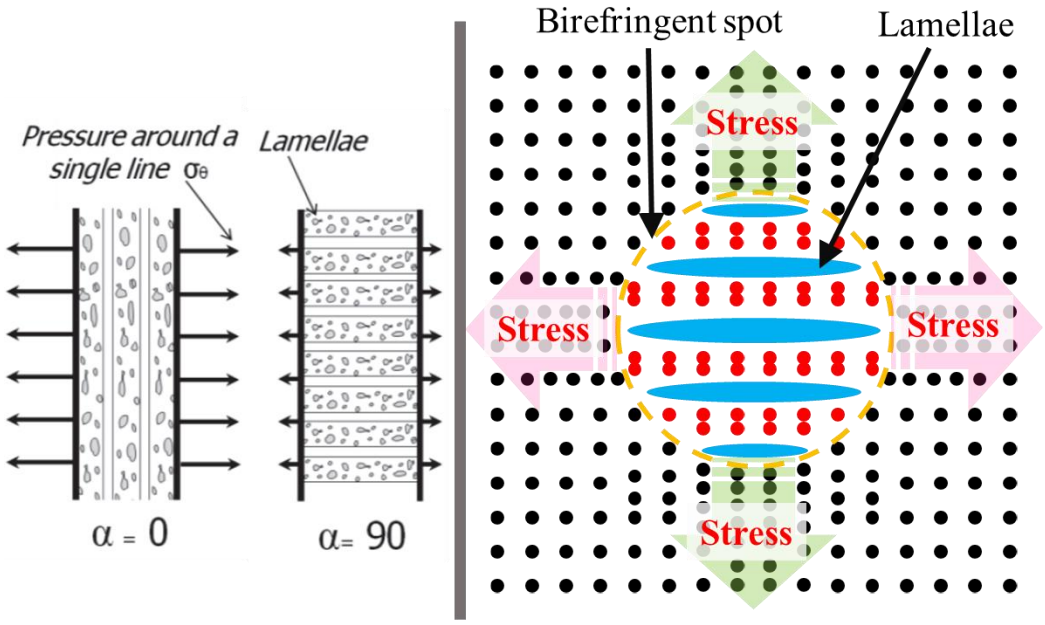

Figure 6.16 Left: Schematic drawing of three lines with different lamellae orientation with respect to the writing direction. Source: A. Champion, *et al.* [105]. Right: Schematic illustration of induced stress around a birefringent spot. The solid dots and dashed yellow circle indicate the material and modification region.

Such stress-induced birefringence was frequently observed during 5 dimensional optical memory experiments while high NA objective was applied. A reasonable hypothesis is that highly localized structural changes create high tension to the surrounding materials, squeeze them towards certain directions and generate stress-induced birefringence. Such unwanted birefringence is what we would like to neglect during 5 dimensional optical memory recording. Therefore an experiment was performed in which different numbers of laser pulses with different intensities were focused underneath a fused silica sample (Figure 6.17). The pulse duration is 280fs, pulse energy is ranging from 27nJ to 90nJ and the repetition rate is 200 kHz.

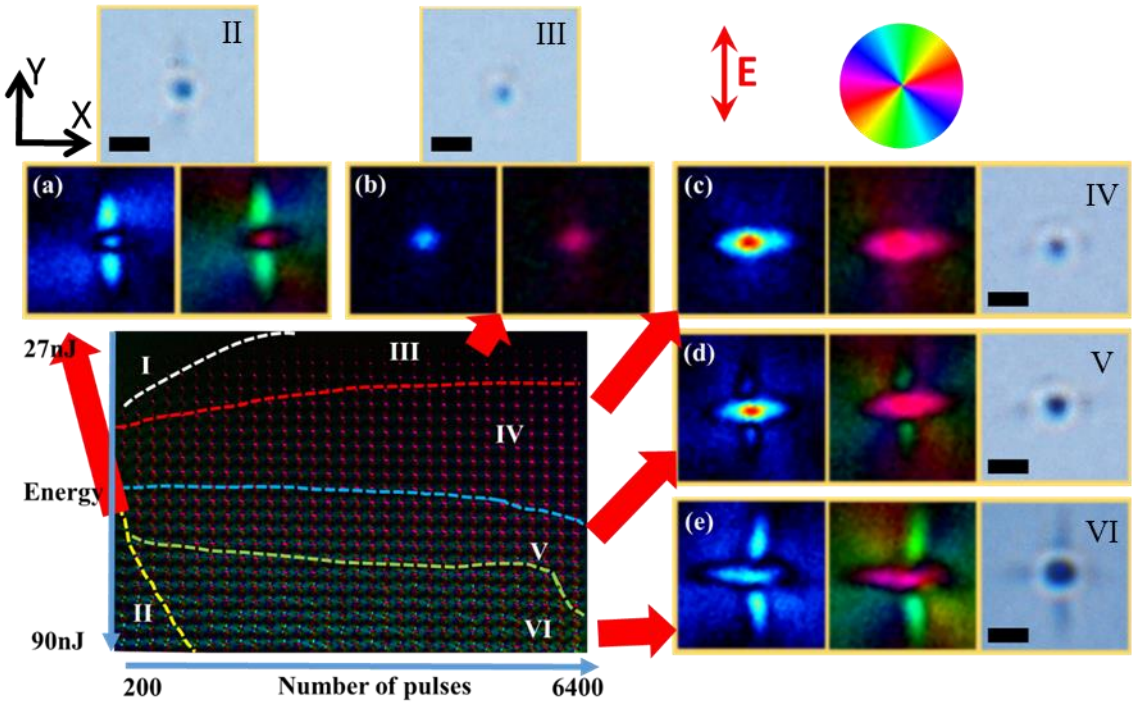

Figure 6.17 Birefringent measurement of structures fabricated with a water immersion objective ($NA = 1.2$, $NA_{eff} \sim 0.75$) on laser energy for different number of pulses. The enlarged images are corresponding optical images, Abrio images of retardance and slow axis orientations (see inset). The scale bar is 1μm, the image plane is xy plane.

Depending on the level of laser energy and number of pulses, one can induce six different types of modification: low intensity induces the structures with no birefringent signal (positive refractive-index change, **regime I** in Figure 6.17); low number of pulses but high energy results in the generation of stress parallel to the polarization direction (**regime II** Figure 6.17(a)); intermediate intensity leads to rounded birefringent spots (**regime III** Figure 6.17(b)); the stress starts to generate horizontally at high energy (**regime IV** Figure 6.17 (c)); the induced stress starts to grow in vertical direction at higher energy (**regime V** Figure 6.17(d)); and at the highest intensity the value of retardance drops and the vertical stress grows to its maximum (**regime VI** Figure 6.17(e)).

Regime III

With the increase of number of pulses and pulse energy, the strength of retardance increases gradually. The porous structures in lamellas are formed and induce very small pressure to the surroundings (Figure 6.18). Although the value of retardance is quite small, this regime is ideal for 5D optical recording as no obvious stress can be observed.

Regime II

The number of pulses is smaller than the condition in Regime III and the energy is much higher. Such energy induces large size porous structures, which are distributed inhomogeneously inside the modification region (Figure 6.18). Randomly distributed porous structures produce huge stress vertically due to the material expansion in this direction. However, the stress induced by each porous structure is isolated along horizontal direction when the lamellas are not well formed. Therefore, small overall pressure is created along the horizontal direction.

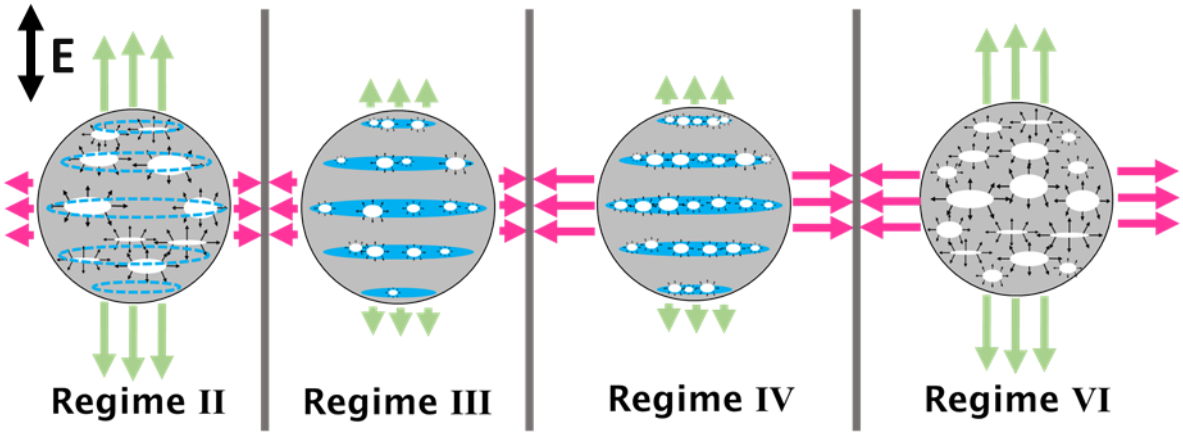

Figure 6.18 Schematic illustrations to explain the laser-induced stresses around the modification spots in different regimes. The arrows indicate stresses.

Regime IV

The number of pores increases further, meanwhile the lamellas are generated perpendicular to the electric field. The horizontally oriented stresses are accumulated along the materials between lamellas and push surrounding materials outwards (Figure 6.18). The strength of retardance is the highest in this regime as the overall retardance is the result of both nanogratings and stress-induced birefringence.

Regime V

The intermediate regime, where the vertical stresses start to generate.

Regime VI

In this regime, the stress increases gradually inside lamellas and causes their collapse eventually [105]. Big porous structures are randomly distributed in the modification region (Figure 6.18). The horizontal and vertical distributed stresses are the sign of material expansion and nanogratings generation from former pulses (Figure 6.17(e)).

6.6 Conclusions

The formation mechanism of laser induced nanogratings was attempted to be explained by plasma wave interference, nanoplasma formation and exciton-polaritons generation. All the suggested explanations are within the scope of single pulse irradiation regime. However, it is known that the generation of nanogratings requires multiple laser pulses. Therefore, experiments aiming at direct observation of the pulse-to-pulse evolution of nanogratings formation should be carried out in the future in order to provide more information.

The laser writing parameters for 5D optical recording was determined by a series of experiments. The experimental results indicated that shorter pulse duration (280fs), 400 pulses and high NA immersion objective are most suitable for 5D optical recording. A beam expanding 4f telescope configuration should be employed into the writing system in order to fill the whole aperture of the objective lens. However, a tightly focused laser beam leads to a highly localized modification in the volume of fused silica. The stress-induced birefringence was observed around the modification spot. Several different regimes of stress were illustrated and the formation mechanism was attempted to explain.

Chapter 7: 5 dimensional optical memory

7.1 Introduction

7.1.1 Importance of Optical Data storage

The evolution of information storage during the history of mankind involves four distinct eras: painted information, carved information, scripted information and digitalized information [109]. The main creative development in this evolution is digitization when mankind could turn almost everything into binary number '0' and '1'. The modern binary number system was first introduced by Gottfried Leibniz in 1703, who was inspired by a Chinese binary system called I Ching. The first modern breakthrough of digitization came in 1801 when the Jacquard loom was first demonstrated. The Jacquard loom simplified complex manufacturing textiles processes by controlling a chain of punched cards in a continuous sequence. The invention of this device enabled complex operations and data storage through paper punched card. The first semiconductor diode in 1906 eventually allowed electronic circuit and data storage to become a reality.

Through the 20th century, one of the main innovations for data storage came about with the invention of optical discs (CDs, DVDs, Blu-rays). With high speed rotation drives (around 10,000 rpm), the writing rate of a Blu-ray disc could achieve around 100 MB/s. This development provided the ability to store large quantities of data in a weightless (around 20 g), small (standard 12 cm diameter) and high capacity (up to 1 TB) DVD or Blu-ray disc. With the invention of the laser diode (a gallium arsenide semiconductor diode firstly demonstrated in 1962) made it possible to compress the whole optical disc reading and writing system in a very compact form. As a result, the CD, DVD and Blu-ray read/write technology are ubiquitous in everyday life: laptops, video game consoles, cars, portable CD players, etc.

In the 21st century, the ability to store and access data is growing rapidly with the internet bringing all forms of information technology to everyone's fingertips. We cannot deny that this tangibility of information has made life faster, informative and more enjoyable than ever. However, with this ability, every

individual or company that is generating large amounts of data on a daily basis, which in turn introduces the desperate need of more efficient forms of data storage. The International Data Corporation investigated that total capacity of data storage is increasing by around 60% each year [110]. As a result, around 44 zettabytes of data will be generated by 2020 [111]. This amount of data will cause a series of problems and one of the main will be power consumption. 1.5% of the total US electricity consumption in 2010 was given to the data centres in the U.S [109]. According to a report by the Natural Resources Defence Council, the power consumption of all data centres in the U.S. will reach roughly 140 billion kilowatt-hours per each year by 2020. This amount of electricity is equivalent to that generated by roughly thirteen Heysham 2 nuclear power stations (one of the biggest stations in UK, net 1240 MWe).

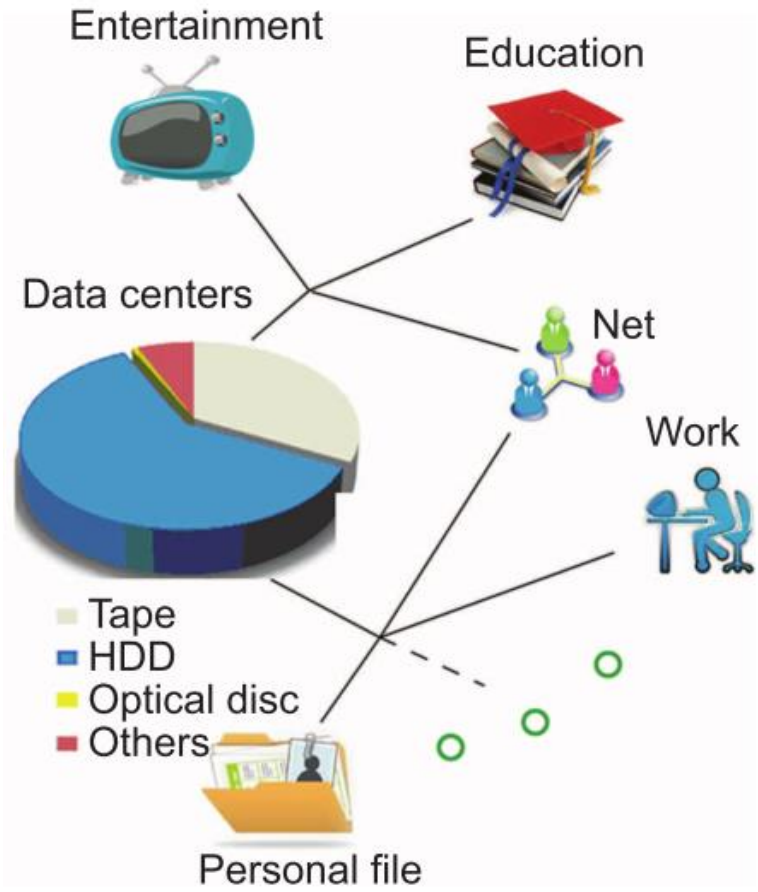

Figure 7.1 The percentage of different storage methods for data centres. Image source: M. Gu *et al.* [109]

Most of these data centres are built based on hard-disk drive (HDD), with only a few designed on optical discs (Figure 7.1). HDD is the most popular solution for digital data storage according to the International Data Corporation [109]. However, HDD is not an energy efficient option for data archiving; the loading energy consumption is around 0.04 W/GB [112]. In addition, HDD is an unsatisfactory candidate for long-term storage due to the short lifetime of the hardware and requires transferring data every two years to avoid any loss. Such additional data transfer process apparently requires even more energy and increases the total cost for data storage. Therefore, the techniques which exhibit high capacity, low energy consumption and long lifetimes are essential for the future. Recent attempts to develop long-term and high capacity data storage and to prove that the data will survive for millions to billions years have been promising [113]. However, despite the space eternal memory concepts, the proposed alternative technologies storing information on DNA [114], silicon-nitride/tungsten based medium [115], microscopically etched/electroformed nickel plates [116,117], are technologically expensive and slow to be practical.

The current solution is the optical disc technique, which only holds a small percentage of data centres usage at present (Figure 7.1). Due to the fact that data cannot be reached instantaneously, optical disc is not the best option for major storage. Nevertheless, since energy is mainly consumed during the initial data writing process, optical discs is more economic in energy usage. The optical disc drive will stay idle after the data is well written. Hence, the advantages such as low price and reduced energy consumption makes the optical disc system the ideal system for data archiving and internet backup currently. Optical disc system as shown in Figure 7.2 is widely employed in industry. It enables the storage of thousands of optical discs and read/write, transfer and placement of the discs simultaneously. The specific disc, which contains data from any one user, will be picked up and transferred to the read/write drive before accessing based on user habits. This kind of optical-disc-based data storage system can lower the cost and spend less energy, meanwhile ensuring that users can access files from their own terminals instantly. Such system is gradually adopted by industrial, Panasonic has developed an optical disc data achieving system in collaboration with Facebook in order to meet the exponential growth of data [118,119].

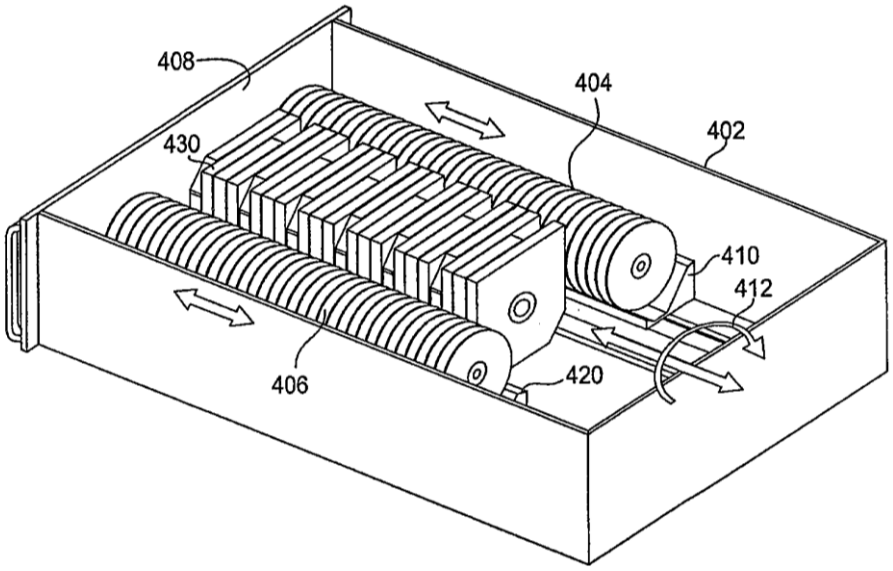

Figure 7.2 An optical disc housing contains optical discs (404, 406), read/write drives (430), sleds (410, 420), track (412) and power sources. Image source: R. Goyal, *et al.* [120]

We believe that optical data storage, well known for its green characteristics, will be the mainstream for data archiving in the near future. The main kind of optical discs employed for data archiving in big data centre is Blu-ray disc, which is limited to tens of GBs [121]. How can GB-scale Blu-ray disc capable for the explosive expansion of data storage? In 2020, tons of Blu-ray discs will occupy tremendous space (about 34 round trip to the moon with Blu-ray discs) [111,118]. Therefore, an optical disc which enables high capacity is essential for our future needs. Currently optical data storage is based in predominantly planar technology, which exploits the linear light absorption of the material, thus is constrained to the surface modification. In addition, planar technology is limited in the number of modification layers, consequently restricting the capacity. In order to further expand the potential optical data storage capacity, a volumetric approach was suggested, known as 3D optical memory, where data can be stored in multiple layers making use of the whole volume of the material.

7.1.2 Breaking the storage-capacity limit by multiplexing

Unlike CD, DVD and Blu-ray discs, which need to add the extra layers physically, the three dimensional (3D) optical storage technique can write potentially thousands of layers (Figure 7.3). Latest developments in 3D optical memory has achieved an approximate capacity of 10 TB in a small spot size of 100 nm by utilizing a dual beam technique named super-resolution photoinduction-inhibition nanolithography (SPIN) [35]. This technology provides the possibility of breaking the diffraction barrier and achieving the smallest features at sizes down to 9 nm [122].

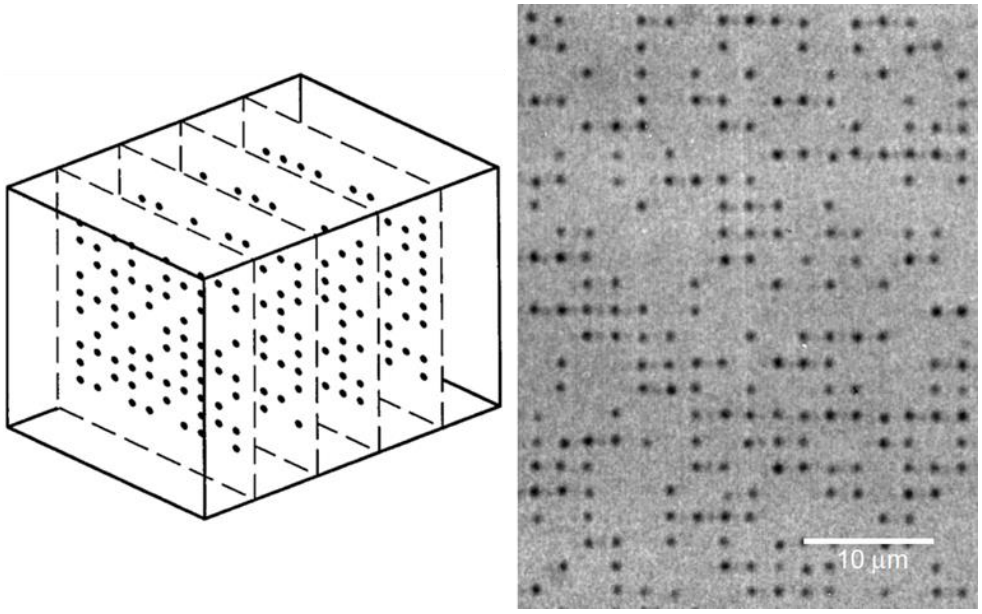

Figure 7.3 Schematic diagram of 3D optical data storage by ultrafast laser in bulk transparent materials. Image source: E. Glezer *et al.* [50].

Normally in a single memory cell or voxel, only 1 bit of data can be stored. However, there is the potential of storing more than one bit in a single voxel by implementing multiplex technology. As a result, the total storage capacity can be further increased alongside readout speed. This approach can be applied in materials which exhibit sensitivity to not only the intensity of the light source used to read but also to other properties of light. The signal can then be read in several independent channels, thus enabling multiplexing of data. Several parameters like polarization [20,52,123,124], wavelength [52,125], space [35,50,126,127], fluorescence [126,127] have all been deliberated as the

additional dimensions for optical data storage. Various materials have been implemented for multi-dimensional data storage such as silver clusters embedded in glass [127] and gold or silver nanoparticles [52,128] (Figure 7.4). The method of data multiplexing is an alternative to holographic data storage [129], which allows overcoming the capacity limit dictated by the optical diffraction.

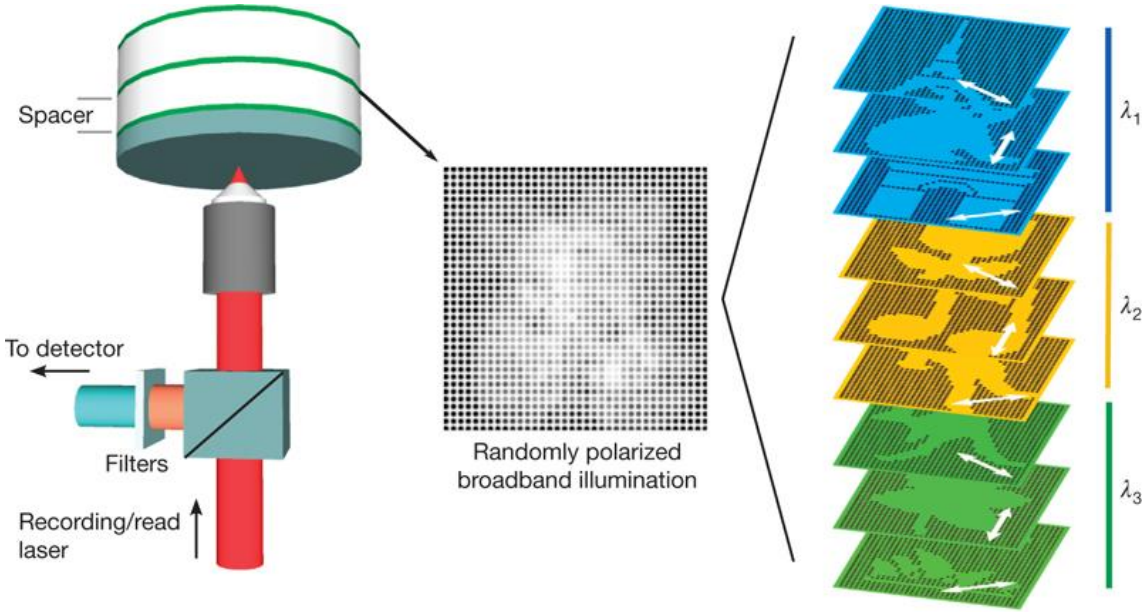

Figure 7.4 Multiplexed optical memory using gold nanorods. The images were patterned using different wavelengths and polarization states as 4th and 5th dimensions. Image source: P. Zijlstra *et al.* [52]

Although lots of attempts have tried to push the boundary of optical data multiplexing, however, limited by the properties of materials five dimensions multiplexing is still the maximum [109].

7.1.3 5D optical storage by laser induced nanogratings

Securely storing large amounts of information over even relatively short timescales of 100 years, comparable to the human memory span, is a challenging problem [130,131]. A general trend, defined in particular by the diffusion process, is a decrease in lifetime as storage density increases. For example, vast amount of data written by individual atoms can only be stored for 10 ps at room temperature [132,133]. The conventional optical data storage technology used for CDs and DVDs has reached capacities of hundreds of gigabits per square inch, but its lifetime is limited to several decades [134–136]. The major challenge is the lack of appropriate storage technology and medium possessing the advantages of both high capacity and long lifetime.

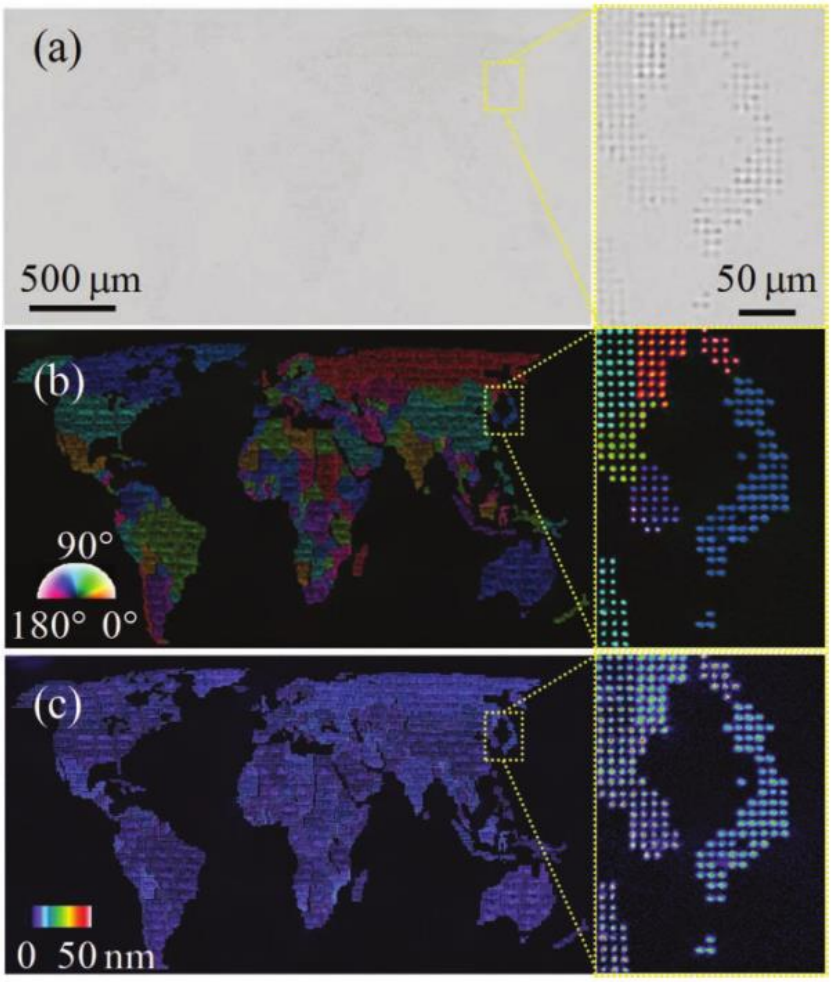

Figure 7.5 Images of the "Small World Map" demonstrating 5D optical memory. (a) optical, (b)slow axis orientation,(c)phase retardance. Image source: Y. Shimotsuma *et al.* [137]

Optical recording based on femtosecond laser writing exhibited both two advantages due to its high-precision high-energy deposition characteristic. It was first proposed and demonstrated in photopolymers [138], later in the bulk of non-photosensitive glass [50,139,140].

More recently polarization multiplexed writing was demonstrated by using self-assembled nanogratings produced by ultrafast laser writing in fused quartz (Figure 7.5) [38,92,137]. The nanograting, featuring 20 nm embedded structures, the smallest ever produced by light [9,44,55,87], is a structural modification which can resist high temperatures [99].

Despite several attempts to explain the physics of peculiar self-organization process, the formation of these nanostructures still remains debatable [9,88,137]. On the macroscopic scale the self-assembled nanostructure behaves as a uniaxial optical crystal with negative birefringence. The optical anisotropy, which results from the alignment of nanogratings, referred to as form birefringence, is of the same order of magnitude as positive birefringence in crystalline quartz [54]. The two independent parameters describing birefringence, the slow axis orientation (4th dimension) and strength of retardance (5^{th} dimension, defined as a product of the birefringence and length of structure), were explored for the optical encoding of information in addition to three spatial coordinates [92]. The slow axis orientation and the retardance are independently manipulated by the polarization and intensity of the incident beam. As a result, the polarization and intensity multiplexing increases the amount of data held per modification spot. Simultaneously the reading speed is increased since more number of bits can be retrieved by reading one modification spot compared to conventional data storage where each physical spot contains only one bit.

Besides the benefits of multiplexing, the 5D optical data based on nanogratings can be also erased and rewritten, which are two important features when considering data storage. The initial nanogratings can be replaced with new ones whose direction is dependent on the incident rewrite laser beam [98]. The rewriting process can be clearly observed in Figure 7.6 (a-c), where the original spot is rewritten with 3, 30, 300 and 4000 pulses of a beam with a laser polarization rotated by 45°. 200 pulses should be enough to erase the previous induced birefringence signal while not generating a strong new signal from the

rewrite laser pulses (Figure 7.6 (e)). About 2000 pulses could completely rewrite the structure, which has the same birefringence signal as the original one. (Figure 7.6 (e)).

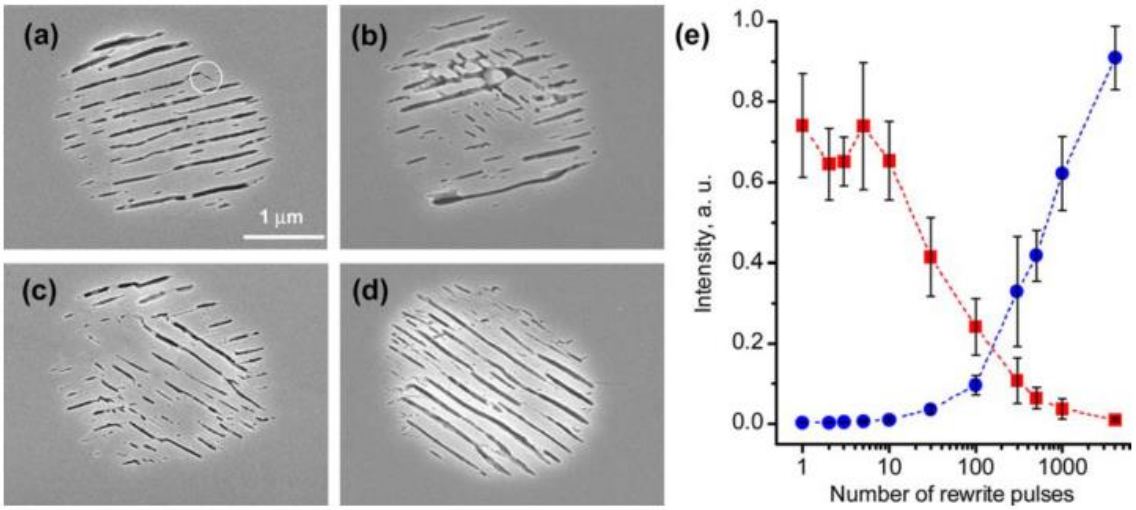

Figure 7.6 Rewriting laser-induced nanogratings with (a) 3, (b) 30, (c) 300 and (d) 4000 pulses. The rewrite polarization is at 45 to the original polarization. (e) Intensity of the birefringence signal as a function of number of rewrite laser pulses where the input polarization is at 45 to the original nanogratings (red squares), and at 45 to the replacement nanogratings (blue dots). Image source: R. Taylor *et al.* [98]

The 5D optical storage technique applied to fused silica is ideal due to fused silica's high chemical and thermal stability (Figure 7.7), making fused silica the ideal medium for long term data storage [99]. Latest studies have demonstrated a fused silica based long lifetime 3D optical memory that has a data capacity equivalent to a DVD disc [141,142]. Additional evaluation results indicate that this optical memory possesses a lifetime of over 319 million years [141].

The situation for 5D optical memory is even superior. Previous studies indicate that the phase retardance only starts to drop at 800℃, but the difference of the phase retardance generated by two levels of energy remains almost the same. [99] (Figure 7.7). Such behaviour is beneficial for the memory application. Even if the birefringence signal drops after a certain period of time or under

some special conditions, the data will still be readable as long as the difference between each signal level is sufficient.

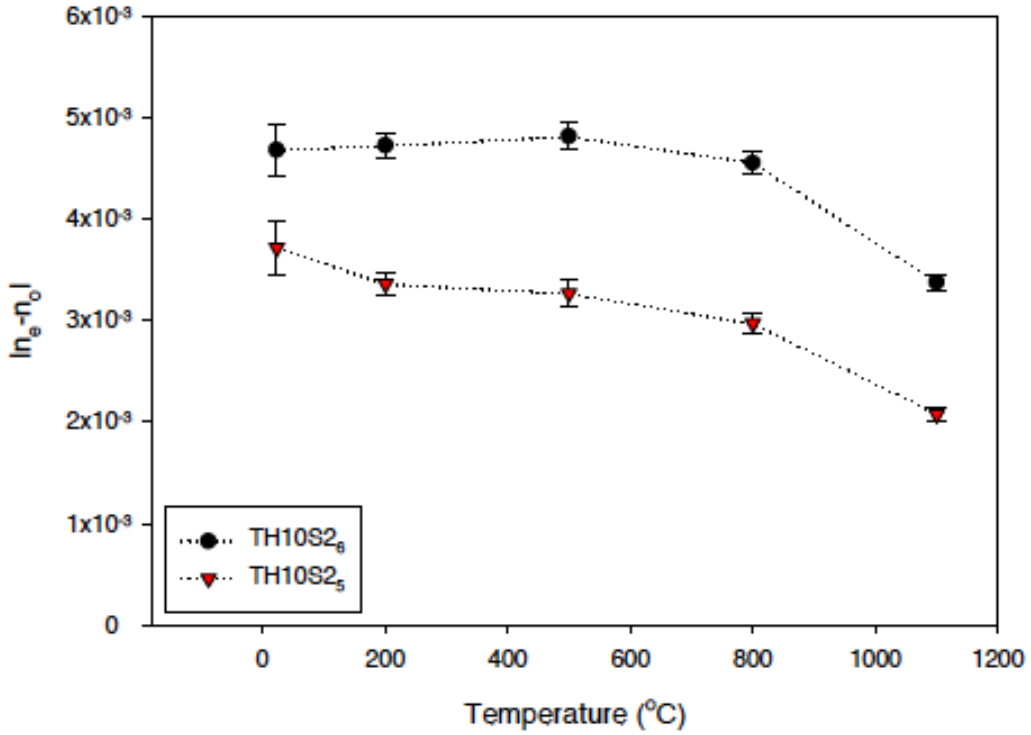

Figure 7.7 Laser induced birefringence value in fused silica as a function of annealing temperature. Pulse energy was set to 1.60 J (black dots) and 2.14 J (red triangles). Image source: E. Bricchi and P. Kazansky [99].

7.1.4 Limitations of laser direct writing setup

There are two independent parameters describing laser-induced form birefringence: slow axis orientation and strength of retardance, which are independently manipulated by the polarization and intensity of the incident beam. Therefore, in order to encrypt the data in 4th and 5th dimension (slow axis orientation and strength of retardance), the data writing setup should be able to change the polarization states and intensity levels of the beam selectively. To get a better understanding of how to improve the writing speed, a simple equation for optical data writing is given below:

$$S = D \times N_s \times N_e \qquad \text{Equation7-1}$$

where S is the speed of data writing (unit: bits/sec)

D is the amount of data per each multiplexed spot (unit: bits/spot)

N_s is the number of spots per each laser exposure (unit: spots/exposure)

N_e is the number of laser exposure per each second (unit: exposures/sec)

By increasing the number of phase retardance levels and slow axis orientations, D can be increased accordingly. In addition, multiple birefringence spots can be printed per one laser exposure (N_s) in order to increase the total writing speed. Whereas, the last variable N_e is determined by many factors:

1. The time spent between two laser exposures (t_m). This time duration involves one laser exposure and movement of the stage.
2. The repetition rate of the laser (f_{rep}) and the number of pulses needed for one laser exposure (N_{pulse}).
3. Time for polarization optics to alter the polarization states and the intensity of beam (t_{optics}).

N_e is limited by the most time-consuming process:

$$N_e = \min(1/t_m\ , f_{rep}/N_{pulse}\ , 1/t_{optics}) \qquad \text{Equation7-2}$$

f_{rep}/N_{pulse} can offer thousands of laser exposure per second using the laser direct writing setup described in section 2.1, on the other hand, $1/t_{optics}$ is a relatively small number (<10). The conventional control using polarization optics turns the manipulation of polarization and intensity into a slow serial process. The rotation of half-wave plate takes a relatively long time (>100 ms) and considerably reduces writing speed. What if we can use a brand new way to control the polarization states and intensity of the beam without rotational polarization optics? In that case, N_e will be only determined by $1/t_m$ and f_{rep}/N_{pulse}.

7.2 Experimental setup

The polarization states of beam are manipulated by rotating a zero-order half-wave plate in our direct laser writing setup. However, how to control polarization states without conventional rotational items? One straightforward idea is to control the intensity distributions of two orthogonal polarizations. Therefore, each spot`s polarization state, which is defined by superposition of two orthogonal polarizations, can be manipulated arbitrarily. Following this idea, it requires a complex setup involving two EASLMs to achieve independent manipulation of two orthogonal polarizations. We came up the idea that instead of using two EASLMs, broke the beam symmetrically in order to obtain two orthogonal polarizations (Figure 7.8(a)).

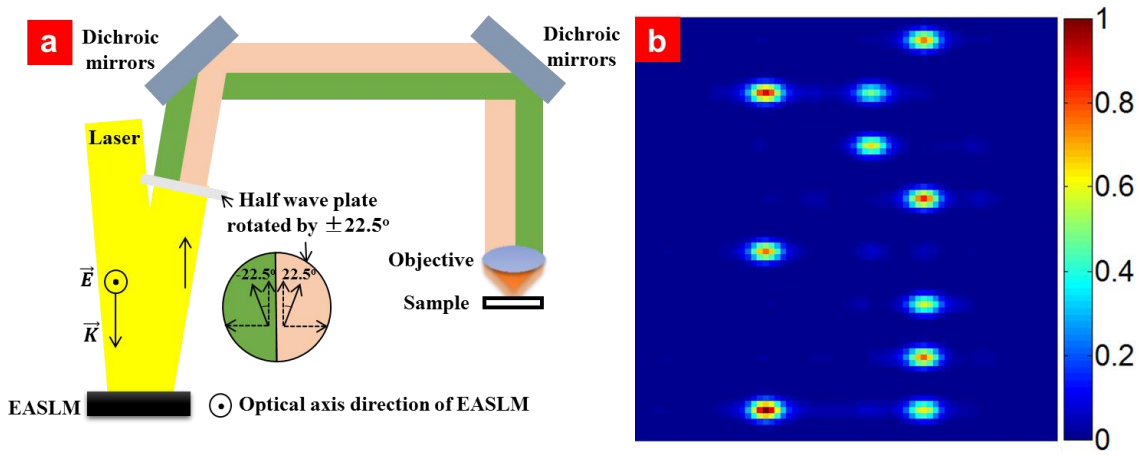

Figure 7.8 (a) Schematic setup for two orthogonal polarization arrangement. (b) Normalized intensity distribution calculated from the holograms on the EASLM.

The screen on EASLM was divided into two halves; each half was printing the hologram correspondingly generated for each polarization. After the beam illuminated on EASLM, the laser beam passed through a half-wave plate matrix and was focused with microscope objective into the sample. The matrix was made up by two half-wave plates (Figure 7.8(a)). The optical axis of the waveplates were -22.5˚ and +22.5˚ separately. Hence, the polarization states of two halves of the beam became -45˚ and 45˚ (Figure 7.8(a)).

The simulation results (Figure 7.8(b)) indicated that although this arrangement could give the arbitrary intensity and polarization control as designed, but each

imprinted spot will be elongated horizontally due to the asymmetric beam arrangement. And such elongation could introduce stress along certain direction when modifying the glass. Therefore, we speculated it is better to keep the beam high-fold rotational symmetric to avoid the elongated beam intensity distribution.

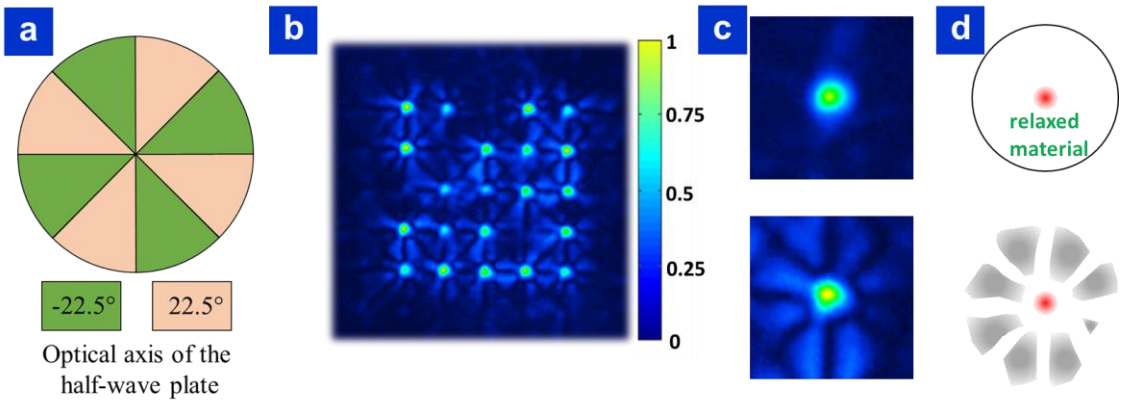

Figure 7.9 (a) Schematic of high-fold rotational symmetric arrangement of half-wave plates. The colours of the half-wave plates indicate the angles of the optical axis. (b) Intensity profile on a CCD camera when using a designed hologram especially for such arrangement. (c) Enlarged intensity plots of beam spots without (top) and with (bottom) the half-wave plates matrix in (a). (d) Schematic drawings showing the induced modifications in (c).

As can be seen from the Figure 7.9(a), a four-fold rotational symmetric half-wave plates arrangement was employed. However, the intensity profile of the beam shows a distinct eight lobes pattern around the central spot (Figure 7.9 (b) and (c) bottom). Such lobes pattern, whose peak intensity is around 50% of the maximum intensity of the central spot, could introduce material densification or even nanogratings when the pulse energy is high. Eventually, these unwanted material changes may lead to stress-induced birefringence around the modification spot. Hence, we concluded that it is not worthy to control the intensity of two orthogonal polarizations by breaking the beam symmetric. However, the arrangement of placing a half-wave plate element after the EASLM in order to control the polarization states of the beam could be implemented in other data recording setups.

Then, it came up with an idea that we could achieve the data writing by controlling which half-wave plate the specific beams array went through and the manner of stage movements. Similar to machinery automation, all spots with different polarization and intensity could be covered just by keep moving the sample in a repeatable routine while changing the holograms on EASLM.

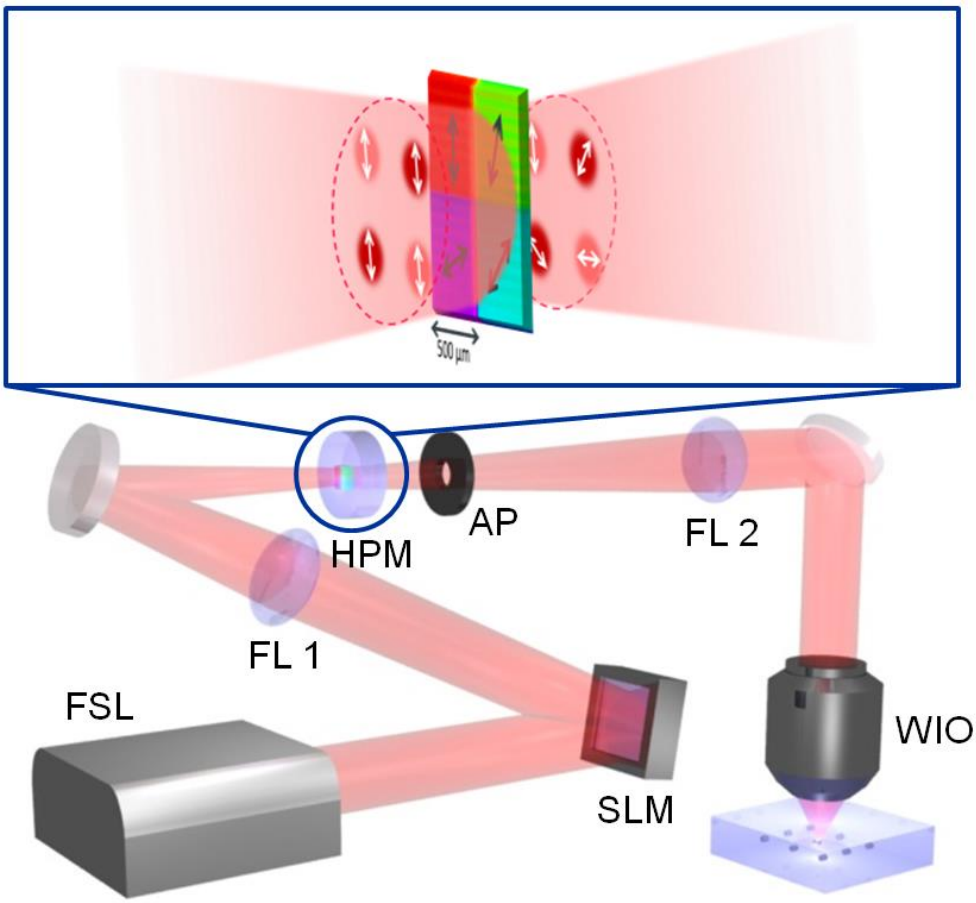

Figure 7.10 5D optical storage ultrafast writing setup. FSL and FL represent femtosecond laser and Fourier lens, respectively. EASLM and HPM represent spatial light modulator and half-wave plate matrix. AP and WIO are the aperture and water immersion objective (1.2 NA). Linearly polarized (white arrows) beams with different intensity levels propagate simultaneously through each half-wave plate segment with different slow axis orientation (black arrows). The colours of the beams indicate different intensity levels.

To realize this idea, a laser imprinted half-wave plate matrix (see HPM in Figure 7.10), made of 4 segments, was added to the 4f optical system enabling motion free polarization control. In the focus plane of the first Fourier lens, where the half-wave plate matrix was placed, several beams with different intensity distribution were projected by the hologram displayed on the SLM. After passing through the segments of the half-wave plate matrix, beams with different polarizations were obtained. Subsequently, the plane of the half-wave plate matrix that contains predefined intensity and polarization distribution is reimaged directly into the sample by the microscope objective. The 4f telescope configuration was employed in order to make sure that the aperture was fully filled by the beam. After synchronising the movement of the sample with the refresh rate of the SLM, multiple birefringent dots with four slow axis orientations and various phase retardance levels can be simultaneously imprinted.

The writing setup, which is illustrated in Figure 7.10, required a particular writing procedure to achieve data recording. A group of beams with different intensity levels were projected by the first Fourier lens (FL 1) onto the half-wave plate matrix (HPM), which consisted of four different half-wave plate segments each with different slow axis orientations as seen in Figure 7.10. The half-wave plate matrix was fabricated by ultrafast laser nanostructuring process described in details elsewhere [54]. After propagation through the matrix four groups of beams with different polarizations were formed (Figure 7.11). By synchronising the movement of the sample with the refresh rate of the SLM, all polarization states could be recorded into one layer. In Figure 7.11, the recording process was depicted inside a 3×3 dot region (yellow square in Figure 7.11). The whole region could be completely filled after four laser exposures. Simultaneously, additional dots with information were printed outside of this 3×3 dot region, thus effectively making the data recording rate much higher. Following this recording procedure, the motion-free polarization and intensity control for 5D optical data recording could be accomplished. The spots distribution during one laser exposure was defined by the polarization states of the spots and orientations of the half-wave plate matrix following the writing manners. Afterwards, the distributions of spots were handed over to a computer workstation for producing holograms. Then the produced holograms were automatically numbered, stored and later used during the laser writing process.

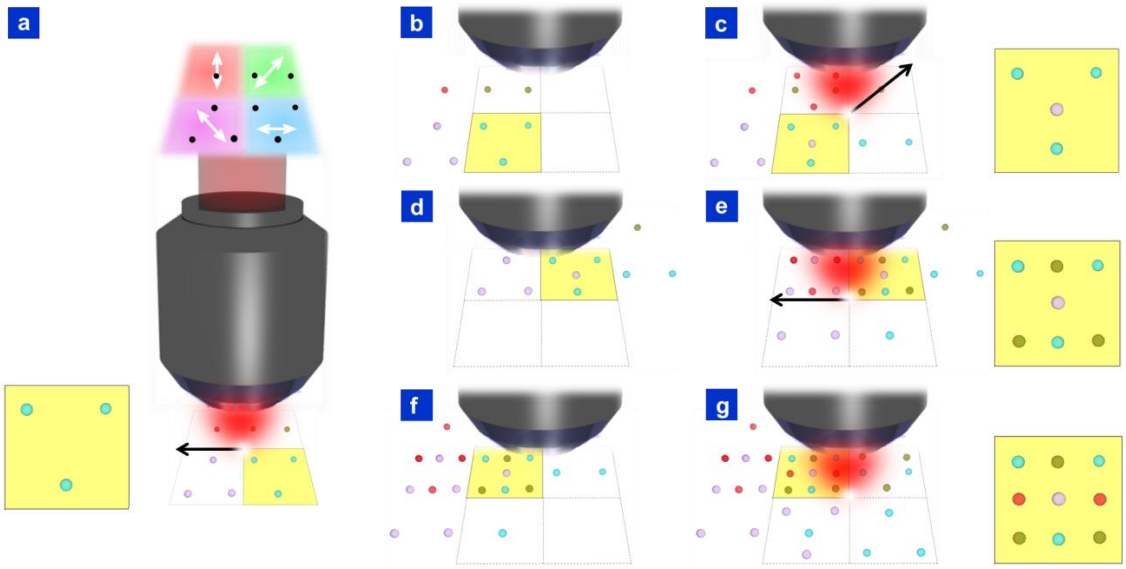

Figure 7.11 The schematic illustration of data storage by the femtosecond laser direct writing technique. The digital data is encoded in spatially variant polarization states of modification spots and divided into the regions whose size is defined by the number of spots and its density. The half-wave plate designed of four sub regions with different orientations of optical axis (red, green, violet and blue) is fabricated and placed before the objective lens. Changing the computer generated holograms, the multi-beam patterns are formed and specific sub-regions of the wave plate are illuminated. Simultaneously controlling the spatial position of the substrate, the target distribution of spots is written in glass. Black spots indicate the original polarization state of the beam. Numbers indicate the specific region of the spots matrix.

Additionally, more states of polarization can be exploited for data encoding by fabricating a half-wave plate matrix with more than four segments (Figure 7.12(a)). The number of intensity states can also be increased by changing the hologram generation parameters. Consequently, these added states, limited by the resolutions of the slow axis orientation (4.7˚) and the retardance (5 nm) [137], can enable more than one byte per modification spot with the current birefringence measurement system. By recording data with a 1.4 NA objective and shorter wavelength (250-350 nm), a disc (4.7 inches in diameter and 1.2 mm thickness) with the capacity of 360 TB can be recorded.

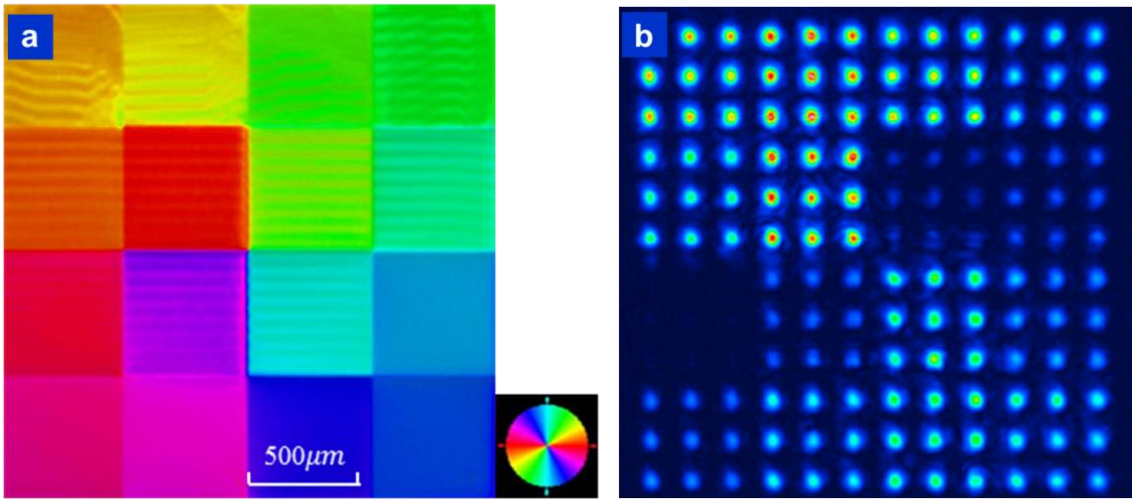

Figure 7.12 (a) Color-coded slow axis orientation of the half wave-plates matrix imprinted in silica glass. (b) Transmitted intensity profile of a spots matrix goes through the half wave-plates matrix in (a) and a linear polarizer.

7.3 Data recording

Up to now, we already demonstrated the data writing process and were able to write any distribution of spots with different polarization and intensity states. Then, how we generate the holograms from the data we would like to store? The holograms take a relatively long time (2 seconds per hologram) to generate, longer than the duration between two laser exposures. Therefore, the holograms cannot be simultaneously generated during the data recording; they have to be prepared in advance. In general, the hologram generation process follows three steps:

1. Read the data into binary bits. The text file follows standard ASCII coding and other files such as pdf and images are read by standard 'fread' function in MATLAB.

2. Certain number of matrixes of spots with different polarization states and intensity levels are built based on the binary data. The number of matrixes equals to the number of data storage layers. All these parameters can be described by the following equations:

$$\text{Data storage spots} = \text{Total data bits}/(\text{bits per one spot can stored})$$
$$\text{Data storage spots per layer} = \text{Data storage spots}/\ (\text{Data storage layers})$$
$$\text{side length} = \text{Ceil}(\text{Squareroot}(\text{Data storage spots per layer}))$$

   where ceil means round towards positive infinity. Thus, all data are ensured to be included in the square matrix. Each square matrix contains the parameters, namely polarization states and intensity levels, of every data storage spot.

3. According to the writing manners, the program automatically picks the specific spots distributions and generates the corresponding holograms. The program will repeat this sequence until all holograms are generated.

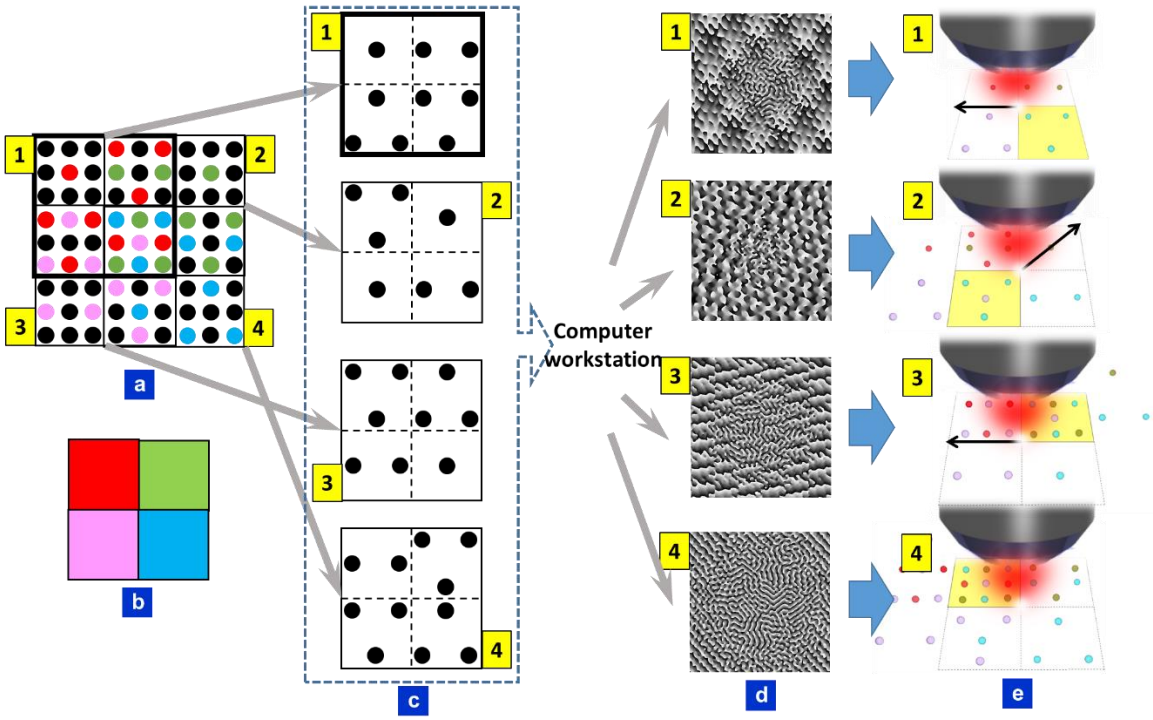

Figure 7.13 The schematic illustration of optical storage recording preparation process. (a) the polarization states of modification spots. Black spots are not involved in this series of writing, spots with other colors indicate different polarization states. (b) Half-wave plate matrix. The colors represent the polarization states of beam when passing through specific wave plates. (c) Target spots distribution. (d) The hologram generated for target distribution of spots. (e) Write the spots in glass. The numbers indicate the writing manners.

The spots distribution during one laser exposure (Figure 7.13(c)) was defined by the polarization states of the spots (Figure 7.13(a)) and orientations of the half-wave plate matrix (Figure 7.13(b)) following the data recording manner. Afterwards, the distributions of spots were handed over to computer workstation for producing holograms (Figure 7.13(d)). Then the produced holograms were automatically numbered, stored and later be used during laser writing (Figure 7.13(e)).

The Data recording experiments were performed with a Yb:KGW based femtosecond laser system (Pharos, Light Conversion Ltd.) operating at 1030 nm and delivering 6.3 μJ pulses at 200 kHz repetition rate and pulse duration

tunable from 270 fs to 800 fs. Despite longer pulse duration can induce higher retardance (80 nm) [83], it also leads to higher stress accumulation and eventual material cracking [50]. As a result, the pulse duration was set to 280 fs.

The drive for our 3D translation stage was an Aerotech A3200 Drive Rack, which could be manipulated by NView (a software provided by Aerotech). NView offers full access of manipulating both the laser and the translation stage. The NView code can be found in the Appendix A. In order to complete the 5D optical storage writing process as demonstrated in Figure 7.11 and Figure 7.13, we need to send the generated holograms onto the EASLM. However, NView does not provide any functions for accessing images or graphic control. But fortunately, NView can access externally located EXE file. Therefore, the final data recording software was divided into two parts: an NView program, which fired/paused the laser and controlled the stage motions; and an external EXE program, which received signal from the NView program and sent specific holograms onto the EASLM.

7.4 Readout results and optimization

The readout of the recorded information encoded in nanostructured glass was performed with a quantitative birefringence measurement system (Abrio, CRi Inc.) integrated into an optical microscope (BX51, Olympus Inc.). Light from a halogen lamp was circularly polarized and filtered with a band-pass filter at 546 nm. After being transmitted through the layers containing information, the signal was collected with a 0.6 NA objective and the state of polarization was characterized with a universal liquid crystal analyser. Typical value of the retardance measured in the experiments was 40 nm. Using this system, three birefringent layers separated by 20 μm in depth could be easily resolved (Figure 7.14 (a)). The phase retardance (Figure 7.14 (c)) and slow axis orientation (Figure 7.14 (d)) was extracted from the raw data, then normalized (Figure 7.14 (e) and (f)) and discretized before the final result was achieved (Figure 7.14 (g) and (h)).

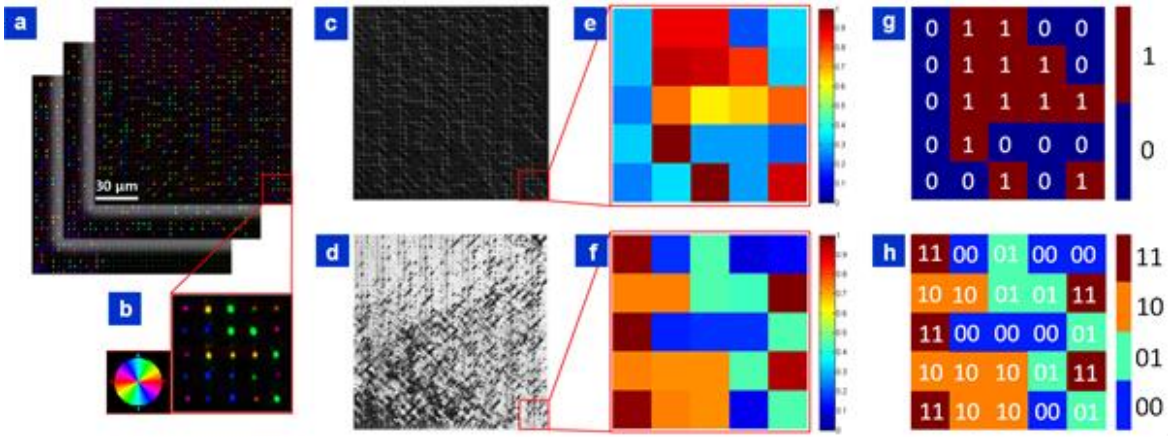

Figure 7.14 5D optical storage readout. (a) Birefringence measurement of the data record in three separate layers. (b) Enlarged 5×5 dots array. (c) Retardance distribution retrieved from the top data layer. (d) Slow axis distribution retrieved from the top data layer. (e), (f) Enlarged normalized retardance matrix and slow axis matrix from (b). (g),(h) Binary data retrieved from (e),(f).

The extraction was achieved by a MATLAB script according to the flow chart in Figure 7.15. The MATLAB script for data retrieving can be found in the Appendix C. The n_1 and n_2 are two reference values predefined to separate the retardance values into two levels. The n_1 is set higher than the retardance value of the

measurement background. Similarly, θ_1, θ_2, … , θ_8 are the fixed reference values in order to split slow axis orientations into four different azimuthal angles.

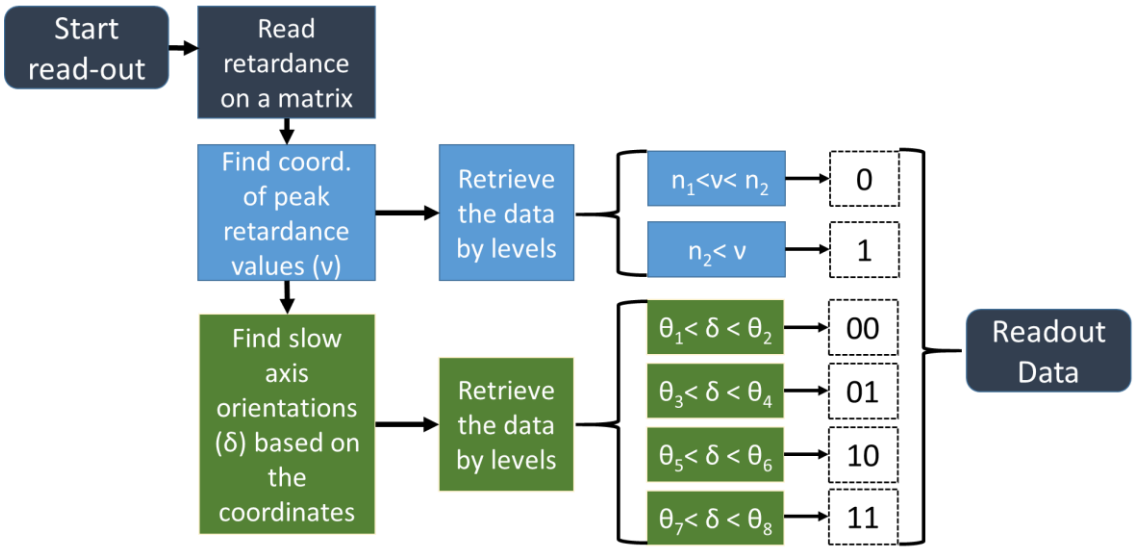

Figure 7.15 Flow chart of retrieving data of 5D optical storage.

The information was decoded by combining two binary data sets retrieved from the phase retardance and the slow axis orientation (Figure 7.15). Out of 11664 bits, which were recorded in three layers, only 42 bits errors were obtained (Table 7.1). Most of the errors were recurring and can be removed by additional calibration procedures, which accounts for the retardance dependence on polarization.

The idea of the optical memory based on femtosecond laser writing in the bulk of transparent material was first proposed in 1996. More recently ultrafast laser writing of self-assembled nanogratings in **c**lass **s**a**3** proposed for the polarization m**5**ltiplex**E**d optical memory, where the information encoding would be realized by means of two birefringenc**m** parameters, i.e. the sl**g**w axis orientation (4th dimension) and s**42**ength of retardance (5th dimension), **)f** addition to three spatial coordinates. The slow axi**{** orientation **á**nd the retardance can be controlled by polarization and intensity of the`incidenô beam respectively. The unprecedented parameters including 360 TB/disc data capacity, thermal stability **5**p to 1000˚C and practically unlimited lifetime. However the implementation of digi**4**al d**!4**a storage, whi**b**h is a cruc**a**al step t**k**wards the real world applications, has not "een demonst**2**ated by ultraf**!**st laser **s**riting.Here we success**n**ully recorded and`retriev**g**d a`di**o**i**u**al copy □f the text **æ**ile in 5D using polarization controlled se**m**f-assembled`ultrafa**ó**t laser nano**{p**ructuring in silica glass.

Table 7.1 Retrieved text from 5D memory. The letters with errors were bolded.

In the 5D optical storage shown in Figure 7.14 (a), the distance between two adjacent spots was 3.7 μm and the distance between each layer was 20 μm. Applying the same writing method on a disc of conventional CD size with 60 layers, 18 GB capacity can be achieved. Using the same parameters it was also successfully recorded across three layers a digital copy of a 310 KB file in PDF format (Figure 7.16).

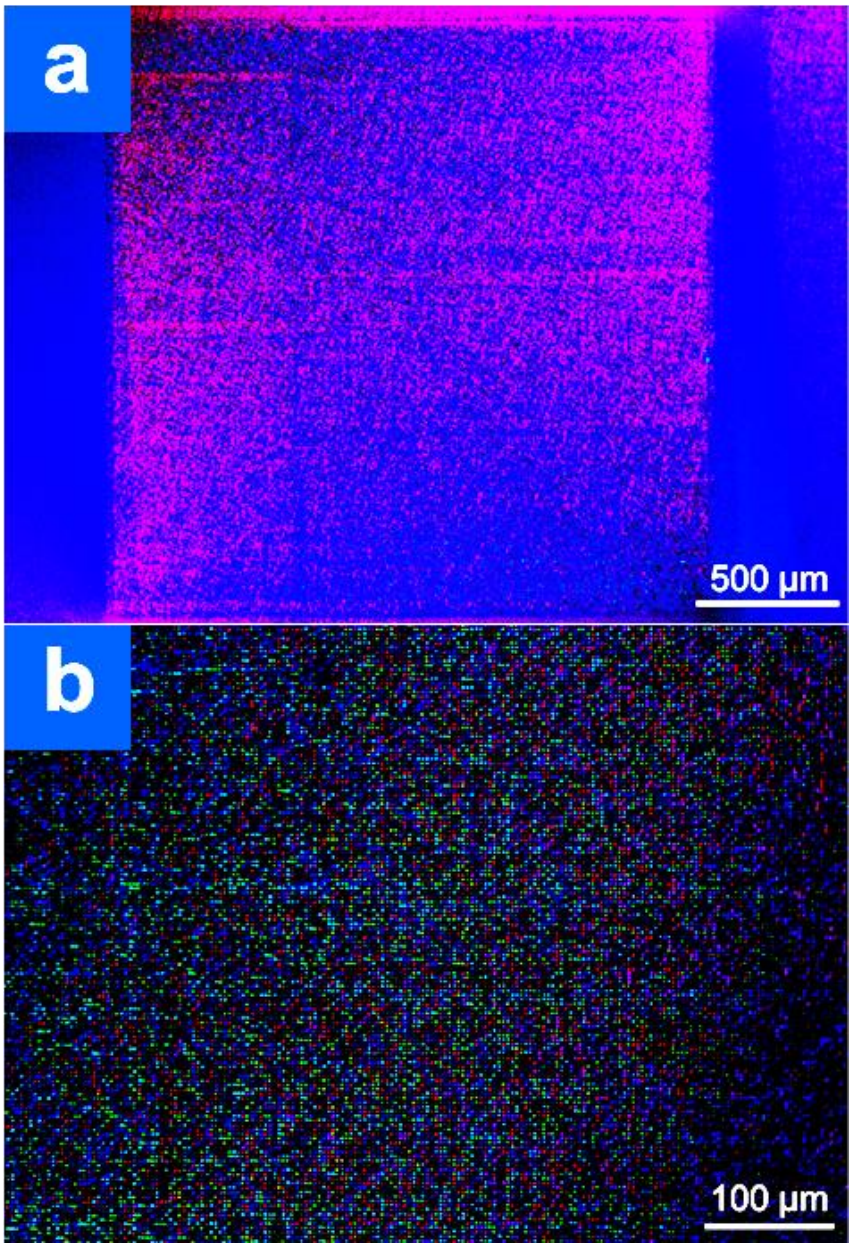

Figure 7.16 (a) Birefringence measurement of the pdf abstract record in fused silica. (b) Enlarged birefringence measurement results.

Now let us take a look back to the retrieved text in Table 7.1. We can find out that many errors are duplicated, for example the letter "**t**" in "s**t**rength", "digi**t**al" and "da**t**a" are read out as "**4**". The binary values represented "t" and "4" are "01110100" and "00110100". Therefore, one bit (the second bit) has been readout incorrectly. Same repeated errors can be found: "**r** (01110010)" been readout as "**2** (00110010)" in "st**r**ength", "demonst**r**ated"; "**s** (01110011)" been readout as "**{** (01111011)" in "axi**s**", "nano**s**tructuring";"**a** (01100001)" been readout as "**!** (00100001)" in "d**a**ta" and "ultraf**a**st". These frequently seen errors indicate that many errors are generated following certain patterns. And they could be excluded by optimization.

We have noticed that some of the errors are shown frequently in the retrieved text. Additionally, if we compare the retardance values of spots induced by different polarizations but same intensity, we can find out that the values of retardance are different depending on slow axis orientations. And this dependence is the cause of the repeated errors in Table 7.1. Similar dependence was observed when characterizing the birefringence signal of laser-written lines [104]. This polarization dependence phenomenon could be related to the pulse front tilt of ultrashort light pulse [105,137,143].

An experiment was implemented for calibration. It was performed with Pharos operating at 200kHz repetition rate. A series of dots was imprinted in fused silica by 400 laser pulses with 16 different polarizations and two levels of energy. The energies were set to 50nJ and 75nJ, lower than the energy when nanogratings starts to generate stress. The strength of the modification was proved to be depending on the writing laser polarization direction when writing lines [104,143]. However, we could observe the dependence more obvious when writing dots. The distribution of retardance values by different polarizations generally follows a sinusoidal-like curve (Figure 7.17 (a)). The peak values of retardance are almost twice as the minimum values for both energies.

The results from the experiment performed with Pharos operating at 500kHz repetition rate are very similar (Figure 7.17 (b)).

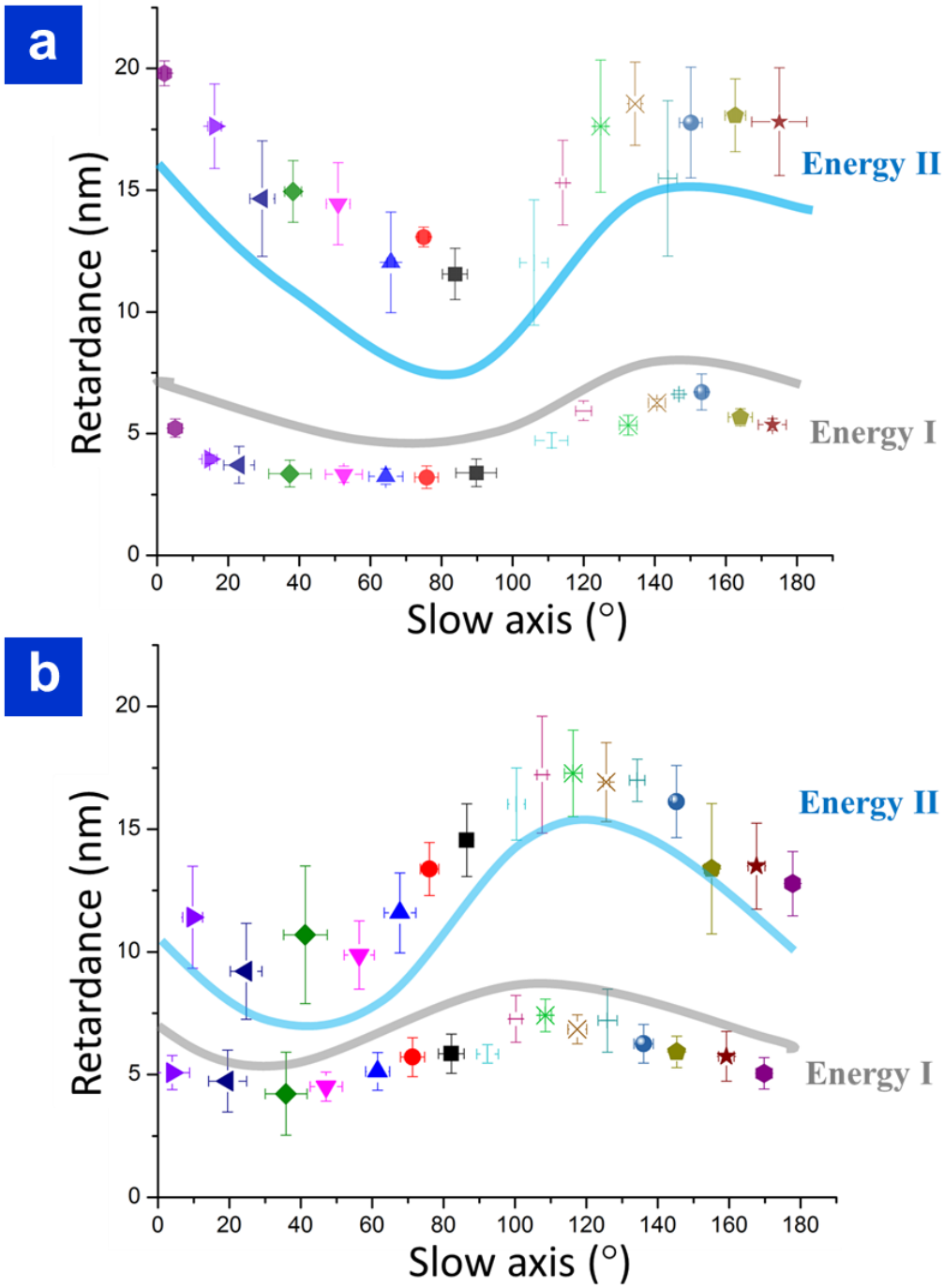

Figure 7.17 Retardance dependence on 16 different slow axis orientations when written with laser pulses delivering two different energies. (a) Delivering 50nJ (Energy I) and 75nJ (Energy II) 400 pulses at 200kHz repetition rate. (b) Delivering 36nJ (Energy I) and 48nJ (Energy II) 2200 pulses at 500kHz repetition rate. The curves are visual guide only.

From the results in Figure 7.17, we can have more profound understanding why the errors were introduced in previous experiment (Table 7.1). Birefringent spots can have significant different values of retardance by same energy when the incident polarizations are different. The ratio of the value of phase retardance between two energy levels ranges from about 2:1 to 4:1 depending on slow axis orientations. In addition, the slow axis orientations are shifted for the incident beams with same polarization but different energy levels (Figure 7.17). Therefore, the readout flow chart in Figure 7.15 is not suitable for future use when there are more states of incident polarizations and energies. The predefined retardance reference values were set differently according to the slow axis orientations. Hence, a new readout flow chart (Figure 7.18), where the data readout process of retardance and slow axis orientation are associated together, was created.

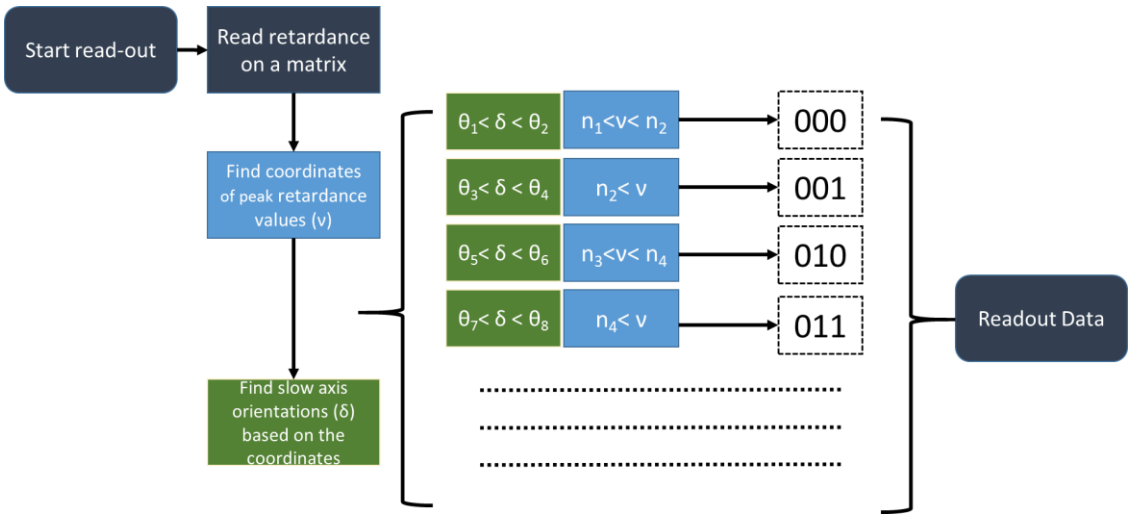

Figure 7.18 Redesigned flow chart of retrieving data of 5D optical storage.

Using the method as demonstrated in Figure 7.18, a new set of experiment was performed. A paragraph from Encyclopedia Britannica about Sir Isaac Newton was recorded in glass. There were four modification layers, but separated by 5 μm. In order to reduce the crosstalk between layers, generate less stress and increase the optical storage capacity, the dots were arranged similarly to body-centered cubic geometry (Figure 7.19(a)). Four segments from each recording layer are shown in Figure 7.19(b). When the birefringence measurement microscope was used to focus on one specific layer, the other layers were out of

focus and did not affect the birefringent measurement values. Such arrangement scheme increases the capacity four times in comparison to the one with 20μm layer separation.

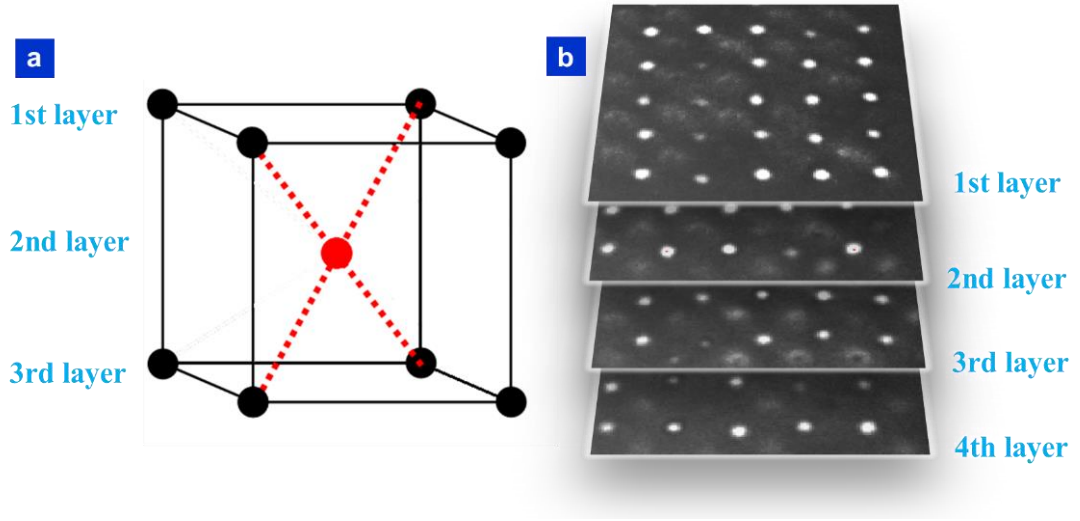

Figure 7.19 (a) Schematic illustration of how birefringent spots are distributed as a body-centered cubic. (b) Measured retardance value in greyscale of four layers.

There were 1087 Bytes of data being recorded in four modification layers. The first word in this recorded Encyclopaedia Britannica paragraph is illustrated indicating how the optimization influenced the final readout results (Figure 7.20). By using the readout method as illustrated in Figure 7.18, the error rate was reduced to 0.22% (19 out of 8696bits) compared to 0.36% previously.

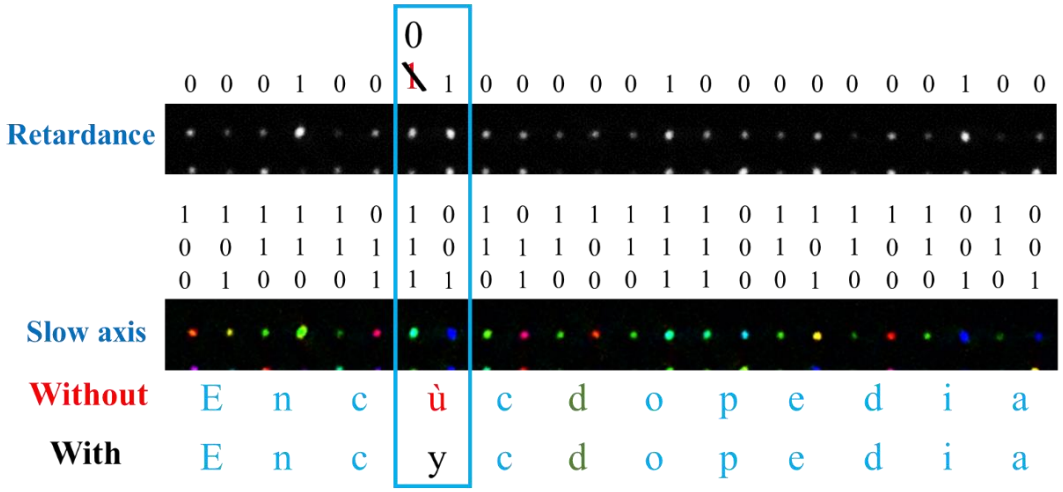

Figure 7.20 Readout the data spots with and without optimization.

7.5 Superiorities of 5D optical memory

7.5.1 Lifetime

5D optical memory attracts great interests partly due to its unlimited lifetime. If the sample is placed at room temperature (303K) the lifetime of nanogratings is $3\times10^{20\pm1}$ years (Figure 7.21). Moreover if the temperature reaches 462K, the lifetime is 13.8 billion years (Figure 7.21). Although, many factors such as temperature variation, pressure and atmosphere haven't taken into account, 5D optical memory is still a very promising permanent data storage technique.

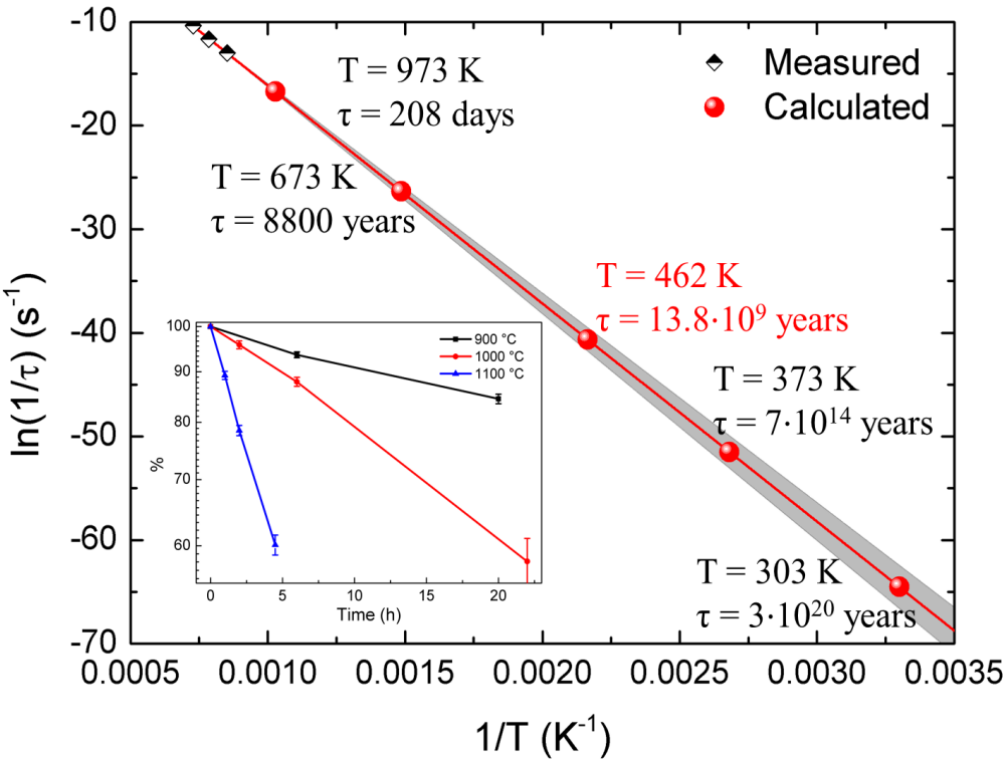

Figure 7.21 Arrhenius plot of nanogratings decay rate. Black dots indicate measured values; red dots are calculated based on fitting results. The grey shaded zone indicates the tolerance of extrapolated values. At the temperature T = 462 K nanogratings would last for the current life time of the Universe. (Inset) The decay of the strength of retardance with time at different annealing temperatures.

The overall data storage techniques can be separated into three most-common groups: semiconductor, magnetic and optical. Semiconductor data storage such as flash drives and solid-state drives (SSD) provide a lifespan around ten years [144]. This is due to the floating-gate transistors in semiconductor based memory becoming unreliable after a number of program/erase cycles [145]. Hence, the lifetime of this memory is mostly depending on its workload, for example, a SSD memory with heavy workload (320GB/day) only has 10% of lifetime as compared to the memory with less of a workload (32GB/day) [146].

For magnetization-based memory such as HDD needs to transfer data every couple of years in order to prevent data loss [109], while the data stored in conventional optical discs such as CD, DVD, HD DVD and Blu-ray only last tens of years [142]. However, already commercialized Millenniata optical discs (M-DISC™) claimed that their discs have an extra-long lifetime up to 1000 years [147]. Also, void-based optical memory in fused silica indicate a lifetime of 300 million years [142,148]. Other schemes such as holographic memory and phase change memory can only reach the lifetime of few decades [149,150].

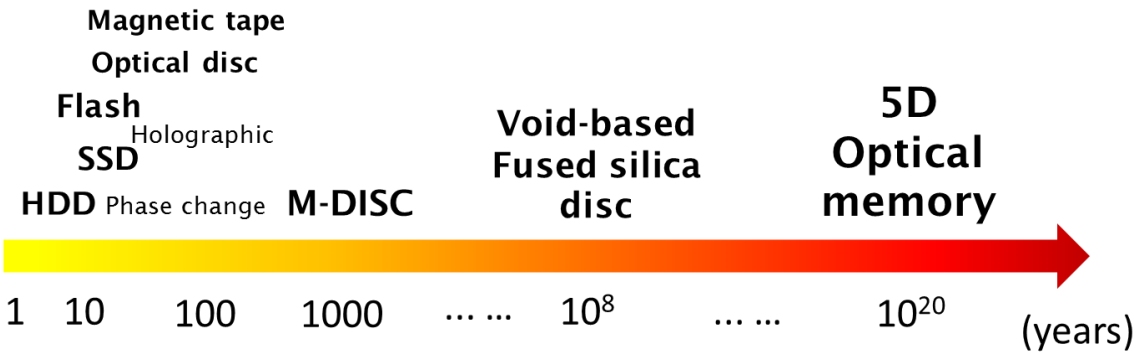

Figure 7.22 Schematic illustrations of typical lifetimes of different data storage approaches.

Data storage approaches are compared in Figure 7.22 in order to give a more intuitive view of storage lifetime. 5D optical memory with its nearly unlimited lifetime is superior to other memory solutions from a lifetime viewpoint.

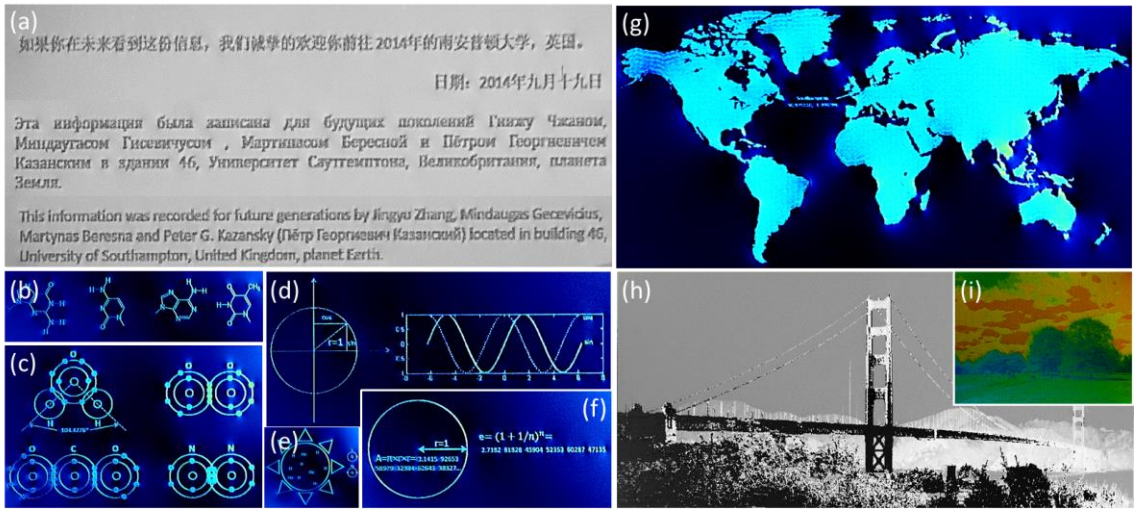

Figure 7.23 Eternal 5D optical data storage: (a) messages written in Chinese, Russian and English languages, (b) structure of four bases found in DNA, (c) molecular structures of water, oxygen, carbon dioxide and nitrogen, (d) profiles of sin and cos functions, (e) mechanism of star formation, (f) mathematical constants π and e, (g) world map with coordinates of Building 46 in Southampton University, and (h-i) sceneries on Earth.

5D optical memory with its nearly unlimited lifetime is superior to other memory solutions. Additional guides stored as visual information could be easily used as a key for the further decoding processes. The complex recording/readout of the eternal 5D optical data storage in silica glass: *Eternal Time Capsule* is demonstrated in (Figure 7.23).

7.5.2 Capacity

We recorded in three layers a digital copy of a 310 KB file in PDF format (Figure 7.16). Applying the same 5D recording method on a disc of CD size, the capacity should follow the equation below:

$$C = \frac{T}{s} \times \frac{S_d}{D_m^2} \times I \qquad \text{Equation 7-3}$$

where, C: capacity; T: thickness of the disc; s: separation between layers; S_d: surface available area of the disc; D_m: distance between two adjacent spots; I: bits of information contained in one modification spot.

It gives us 18 GB capacity from our experiment demonstrations (Figure 7.16). However, it can be affirmed that more states of polarization can be exploited for data encoding by fabricating half-wave plate matrix with more than four segments. The number of intensity states can also be increased by changing the hologram generation parameters. Consequently, these added states, limited by the resolutions of the slow axis orientation (4.7°) and the retardance (5 nm) [137], can enable more than one byte per modification spot with the current birefringence measurement system. One modification spot can contain 4 bits (16 states) data from retardance and 5 bits (32 states) data from slow axis orientation of the birefringence.

The minimum size of the modification is limited by wavelength of the laser light, numerical aperture of the focusing objective lens and modification threshold of the material. By increasing the numerical aperture to almost 1.0 (in air), a focused linearly polarized beam with Gaussian intensity profile can reach a small focal area of $0.31\lambda^2$ [151].

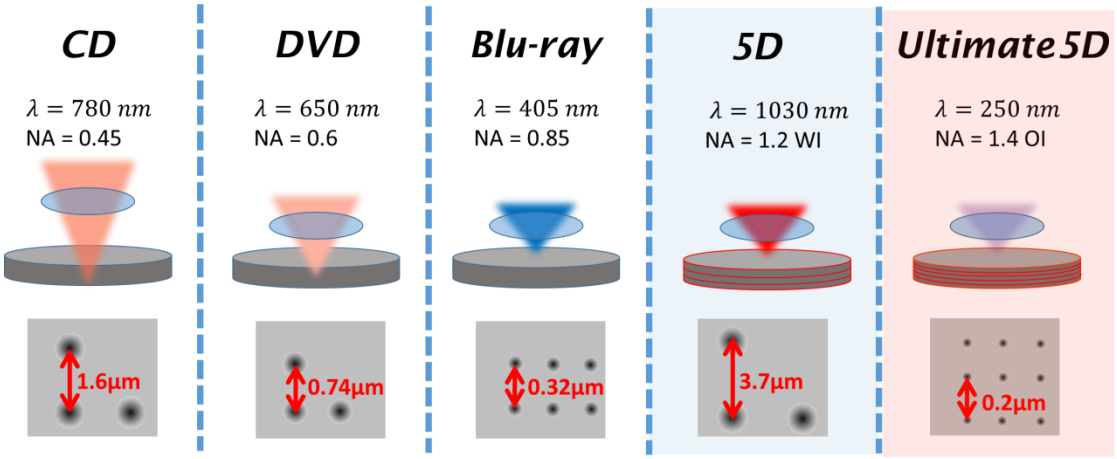

Figure 7.24 Comparison of various parameters of CD, DVD, Blu-ray, current 5D and ultimate 5D: wavelength (λ), numerical aperture (NA) and track pitch.

Diameter of a focused laser spot (d) is limited by the optical diffraction of the light as $d = {}^{1.22\lambda}/_{NA}$ [35]. By applying the same equation with our experimental conditions, the diameter of the femtosecond laser spot is around 1040nm.

The width of the generated pit should be smaller than the diameter of the laser spot. It varies depending on the modification threshold of different materials. In our experiments, the widths of the birefringence spots range from 500nm (${}^{0.58\lambda}/_{NA}$) to 800nm (${}^{0.93\lambda}/_{NA}$) depending on intensity levels. If assuming the relation of the constant, wavelength and numerical aperture holds, the ultimate 5D optical recording system (Figure 7.24) should produce the birefringence spots with the width ranging from 100nm (${}^{0.58\lambda}/_{NA}$) to 166nm (${}^{0.93\lambda}/_{NA}$). Therefore, it is possible to reduce the separation between each adjacent spot to smaller than 200 nm by implementing a laser with 250nm wavelength and an objective lens with 1.4NA.

Along the direction of beam propagating, the length of the structure was around 2μm under our experimental conditions (Figure 6.13). If applying a laser with shorter wavelength and higher NA, the length can be even reduced to 300nm. And the separation between each adjacent layer can be reduced to less than one micrometer. Thus, we obtain 360 TB for 5D storage in 1200 layers for a typical disc with 1.2 mm thickness.

However, the depth of focus drops dramatically when increasing numerical aperture and reducing wavelength [152]. Approaches such as using phase apodizers [152], phase patterns based on 3D Fourier transform [153] and Fresnel lens phase grating patterns [154] can enable volumetric multifocal beam modification. Among these approaches, adding the Fresnel lens' phase pattern onto the SLM requires less computer calculation and no extra device. The position of the focal plane can be manipulated by adding the lens' phase pattern to the existing computer generated hologram. The maximum displacement of the focal plane should be determined by the total pixel number of the SLM. The phase pattern of Fresnel lens should follow the equation below:

$$\varphi_z(\vec{\rho}) = \frac{2\pi\rho^2 z}{\lambda f^2} \bmod 2\pi \qquad \text{Equation 7-4}$$

where z is the targeted displacement of the beam array relative to the initial focal plane, f is the effective focal length and $\vec{\rho}$ represents a pixel position on the SLM screen.

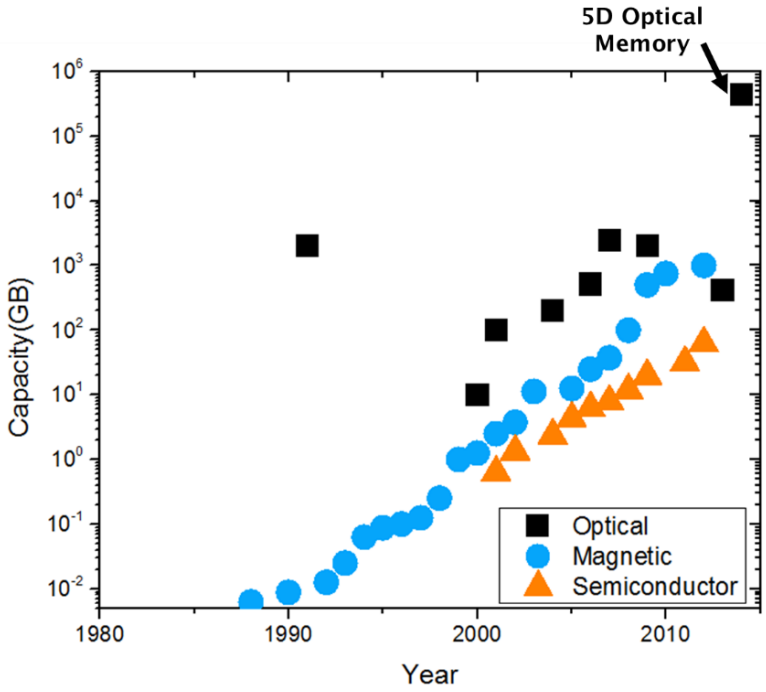

Figure 7.25 The development of semiconductor, magnetic and optical based data storage [19,35,52,109,138,155–158]. The capacity of optical, magnetic and semiconductor memory is calculated based on an area of 1 inch^3, 1 inch^2 and 1 inch^2 respectively.

The magnetization-based data storage, in which each data bit is recorded in a smallest 10nm side magnetic island, has the theoretical limitation of 12TB [109,158]. However, even this number of capacity is much lower than what 5D optical memory promised. 5D optical memory, which may give a capacity of 439TB/inch^3 in the future, exceeds other technologies more than one order of magnitude.

The capacity of magnetic and semiconductor based storage grows exponentially in the last couple decades (Figure 7.25). This is due to only few materials such as silicon, iron(III) oxide and cobalt-based alloy were intensively investigated for magnetic and semiconductor based data storage. And the industrial standards were set very early, therefore researches and developments could be done following certain roadmap. In the case of optical data storage, studies were carried out on massive materials such as, nonphotosensitive glass [50,53], photosensitive polymer [159], phase-change materials [160] and metal nanoparticles [52]. No general consensus has been reached regarding the next generation optical data storage.

7.6 Discussions and suggestions

In the previous sections, we have demonstrated the prototype of 5D optical data coding, writing, readout and decrypt process. However, there are many technique problems restricting the writing and readout speed. In this section, I will discuss current situations and suggest possible solutions.

7.6.1 Writing system

The actual writing speed for the setup in Figure 7.10 is about 75 bits/s due to the bad synchronization of Aerotech stage, laser and EASLM. The maximum writing speed can reach 6 KB/s if the stage, laser and EASLM can be manipulated and synchronized under a same software environment. The bottleneck of the data recording rate of this writing setup is created by the repetition rate (200 kHz) and the average power of the laser (6 W) and slow refresh rate of the EASLM (60 Hz). We believe that a maximum 120 Mbit/sec data recording speed can be achieved by using an EASLM with a faster refresh rate (20 kHz [161]) and high power ultrashort laser oscillators operating at megahertz repetition rates with an average power over 50 W [162]. The multiplexing technique can also help to exceed the data recording speed of the standard binary optical encoding system at the same laser repetition rate.

Compared to conventional optical disc solution, for example Blu-ray disc, which offers tens of MB/s data rate, the writing speed for 5D optical memory is impractically low. What is the main issue?

As illustrated in section 7.1.4, the speed of data writing is determined by three factors: D (amount of data per spot), N_s (number of spots per each laser exposure) and N_e(number of laser exposure per each second). The maximum value of D is 8bits per modification spot and the current value is 3bits per spot. Increasing D to its maximum will only increase the writing speed by less than three times.

The current value of N_s is 25 spots per laser exposur, N_s can reach 1000 spots per laser exposure if a laser with 50W power is employed. In this case, the data recording speed can be increased by 40 times. Assuming both D and N_s reach

their maximum, the writing speed will achieve 640KB/s. However, the speed is still very slow compared to the data storage solutions on the market.

The problem is the value of N_e. The data recording setup (Figure 7.10) involves an EASLM, whose refresh rate is 60Hz. This means that the maximum value of N_e we can obtain is 60. Therefore, the recording system has a maximum writing speed of 6KB/s. To improve the writing speed, one straightforward idea is to employ an EASLM with faster refresh rate into the writing setup. Then, the next obstacle to overcome will be the movement of the translation stage. So let us examine the factors which determine N_e again:

1. The time spent between two laser exposures (t_m). This time duration includes one laser exposure and the subsequent movement of the stage. $N_e \leq 1/t_m$

   If assuming the acceleration, deceleration and vibration of the stage may take 10ms per each irradiation, the maximum N_e is around 100.

2. The repetition rate of the laser (f_{rep}) and the number of pulses required during one laser exposure (N_{pulse}). Thus, $N_e \leq f_{rep}/N_{pulse}$

   The maximum N_e is 1250 by applying current setup (repetition rate equals to 500kHz and minimum 400 pulses for one laser exposure).

3. Time for the polarization optics to alter the polarization states and the intensity levels of the beam (t_{optics}). Therefore, $N_e \leq 1/t_{optics}$.

   The current maximum value of N_e is 60. Whereas, other SLMs with much faster refreshing rate (20 kHz) are under development.

From above, we can see that even we solve the problem caused by the current EASLM, the next issue need to be addressed will be the movement of the stage. In addition, if we can find a stage with both high precision and high moving speed (rotary stage), then the writing speed will be limited by f_{rep}/N_{pulse}. Although, there are some experiment results indicating that the birefringence signal is strong enough for data recording when focusing only few tens of pulses through low NA objective. However, this may due to the fact that beam focused by low NA objective produces an elongated structure. And longer structure results in higher phase retardance since the birefringence signal is accumulated

along the vertical direction. However, we always want to keep the structure as small as possible in all dimensions in order to offer higher capacity. Therefore, such approach, which achieves reduced number of pulses by sacrificing total capacity of the memory, is not a promising option.

Nevertheless, to reduce number of pulses required for generating structures is a major direction to increase data writing speed. Therefore, I would like to discuss the possible improvements of the writing system based on two assumptions:

Assumption 1: Still requires tens of pulses to generate birefringent spots.

1) Translation stage.

The beam will draw a line of 4μm during one laser exposure if the translation stage is not stationary during laser irradiation (assuming repetition rate, pulses per laser exposure and writing speed are: 500 kHz, 100, 20mm/s). It will be unrealistic to produce enough birefringence signals with such few pulses spread along a 4μm distance. Therefore, the translation stage has to be stationary while firing laser. In this case, the effects of acceleration, deceleration and vibration of the stage need to be well inspected during writing.

2) Laser

High power femtosecond laser oscillators working at megahertz repetition rates with average power over 50W.

3) Holograms

Pre-calculating all holograms consumes more time than writing data itself. In addition, the hologram files occupy thousands times more storage space than the data itself (the size of one hologram is around 400KB). Therefore, it would be great to get rid of the holograms.

4) EASLM

Liquid crystal based EASLMs on the market have a relative low refresh rate ranging from 30 Hz to 1 kHz. Other devices such as deformable mirrors and magneto-optical based SLM offer higher refresh rate. However, the number of

pixels for deformable mirrors is relatively small (several thousands) [163]. Lacking enough pixels results in dropped quality of the reconstruction patterns [164]. The best candidate would be the magneto-optical based SLM, whose response time is around 0.015μs [161]. It can offer a refresh rate up to tens of MHz.

Ultimately, a new writing setup is suggested below summarizing all the ideas above. The design concept of this setup, in the light of former setup in Figure 7.10, is to get rid of calculating holograms. The multiple beam spots approach is also applied in order to increase the writing speed.

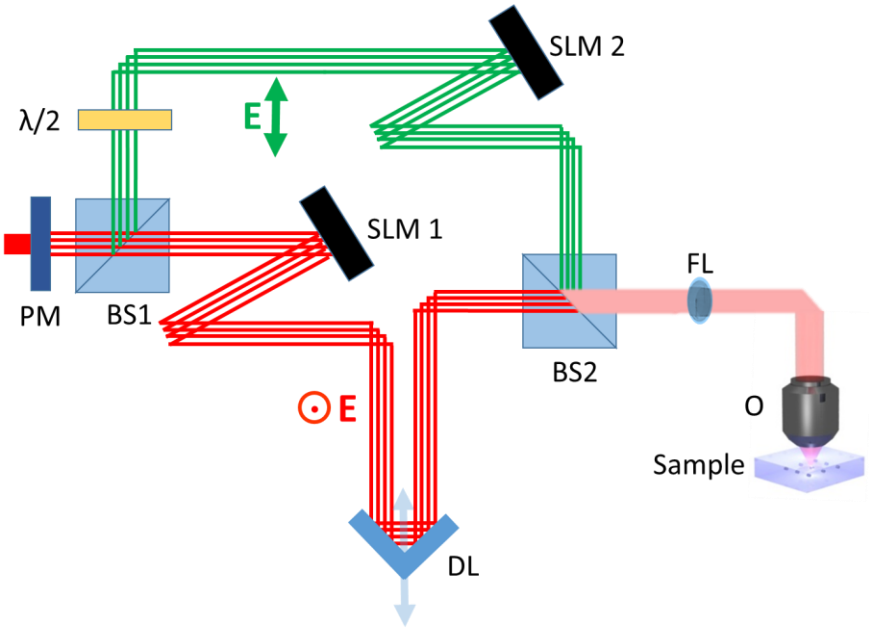

Figure 7.26 Schematic drawing of proposed writing setup for Assumption 1: phase mask (PM), polarizing beam splitters (BS1, BS2), half-wave plate (λ/2), spatial light modulator (SLM1, SLM2), optical delay line (DL), Fourier lens (FL), objective (O).

The polarization manipulation is achieved by using two orthogonally polarized beams and two SLMs (Figure 7.26). Thus, each merged beam spot can have arbitrary polarization states by superposition of two orthogonal polarizations. The delay line is used to compensate phase difference for two orthogonal beams.

The intensity modulation of the beam is achieved by a phase mask and two SLMs (Figure 7.26). A phase pattern, which changes the beam profile from Gaussian distribution into a spots array (32×32), can be fabricated as a phase mask by

lithography techniques. The pattern is generated by the GSW algorithm explained in section 3.2 (Figure 7.27 (a)). The spots array (Figure 7.27 (b)) is irradiated on the screen of the SLM (Figure 7.27 (c)). The SLM screen is divided into 32×32 separate square areas. Each area contains one hologram, which determines whether to reflect or scatter the irradiated beam on this area (Figure 7.27 (c)). The intensity of the reflected beam can be manipulated by switching holograms, which could be pre-generated by a mechanism based on phase-only gratings [165] (Figure 7.27 (c)).

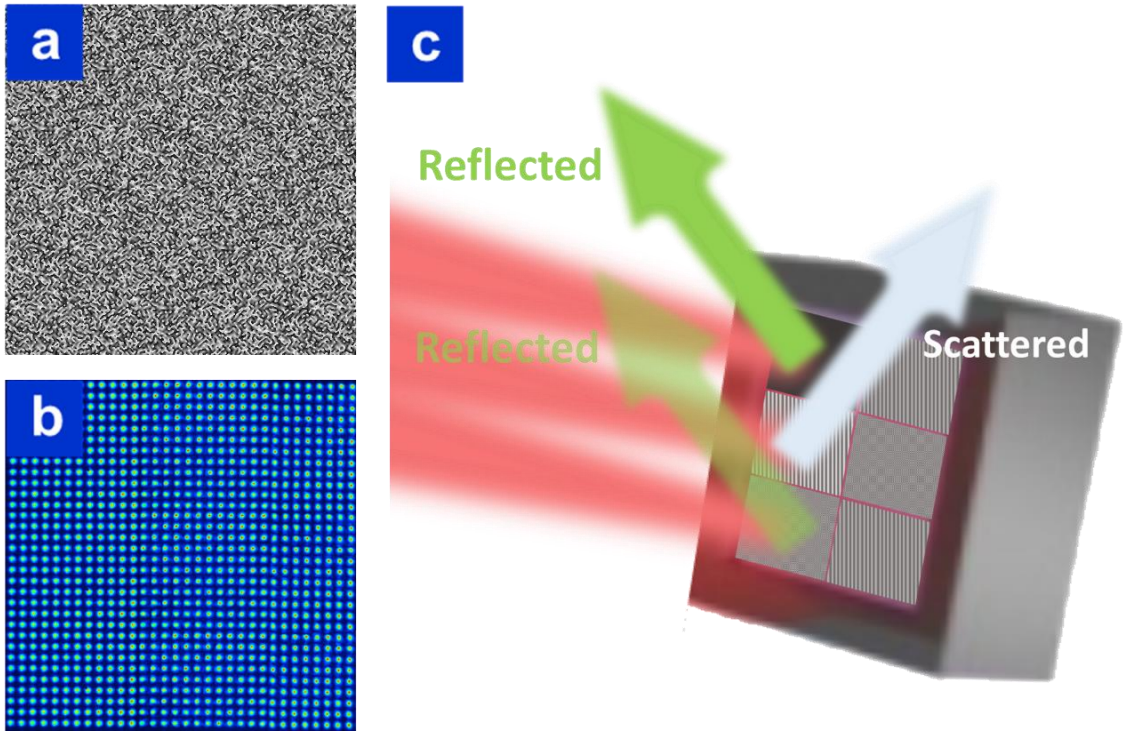

Figure 7.27 (a) Phase hologram for the phase mask. (b) Intensity profile of spots array generated by the hologram in (a) on a CCD camera. (c) Schematic drawing of the spots array irradiating on the SLM.

There are only several limited states for each beam spot in the spots array: to be scattered or to be reflected with different intensity levels. Therefore, this data recording system only involves certain number of pre-generated holograms. For example, if the data encoding requires 4 bits from phase retardance modulation, then the intensity levels of the beams can be manipulated by 16 separate pre-designed holograms. During laser writing, the computer workstation only requires to print a matrix of 32×32 holograms on the SLM. The pre-designed

holograms are placed according to the coordinates of the holograms matrix. Thus, we have gotten rid of complex iterated hologram generation process.

The writing speed can reach around 800 Kbit/s by using the system illustrated in Figure 7.26 based on Equation7-1:

$$S = D \times N_s \times N_e$$
$$= 800\ Kbit/s$$

D, 8 bits per spot (16 states for polarization states and 16 states of retardance).

N_s, We can have a maximum of ~1,000 spots by using a laser with an average power of 50W.

N_e, is limited by the time spent for acceleration, deceleration and vibration of the stage. The maximum of N_e is 100, assuming a minimum 10ms time is required during one laser irradiation cycle.

The highest writing speed is around 800 Kbit/s while employing the writing system demonstrated in Figure 7.26. The advantages of this system are no massive pre-calculated holograms and no rotational polarization optics. However, the drawback is there is considerable number of devices in this writing system. And the recording speed is limited by the time spent on the movement of translation stage.

Assumption 2: It only requires single or several pulses to generate birefringent spots.

In this case, translation stage is not a tricky problem anymore. Rotary stage system such as spindle platter, which is implemented in CD and Blu-ray drives, can be employed in 5D optical recording system. Compared to translation stage, which is giant and expensive, rotary stage system is more compact and much cheaper. It is already a well-built system while optical storage system develops.

In order to increase the writing speed and certainly avoiding calculating holograms, a recording system based on rotary stage is demonstrated:

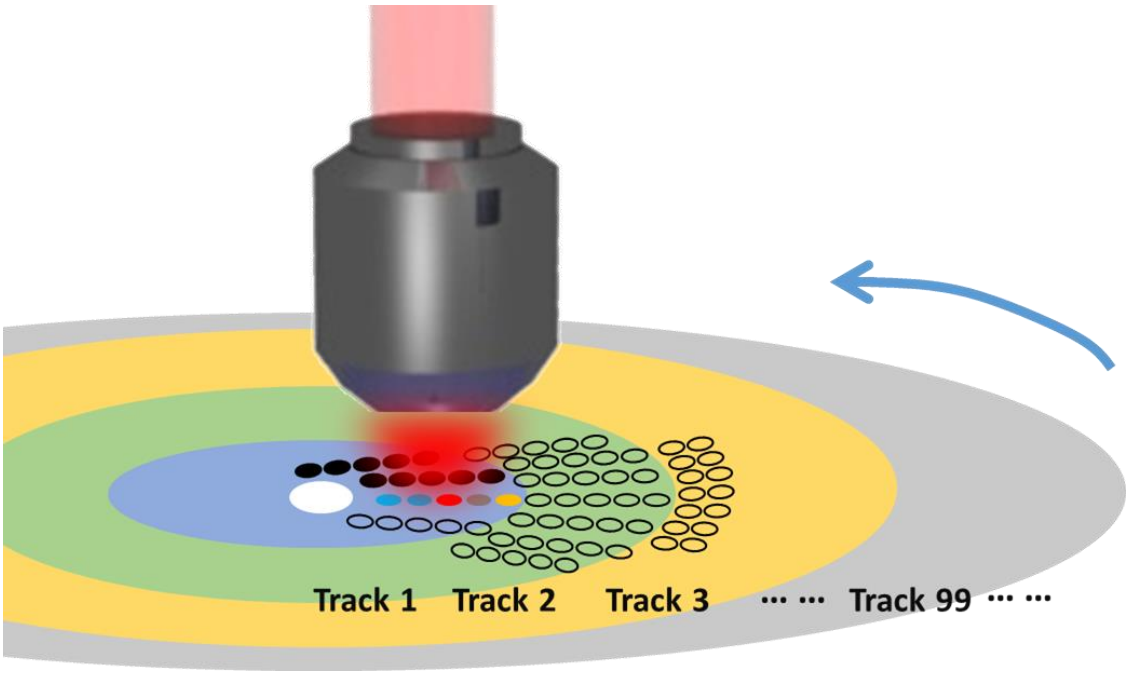

Figure 7.28 Schematic drawing of 5D optical recording on a fused silica disc for assumption 2. The colors indicate polarization state of the spots. The hollow ellipses represent vacant data slots.

To increase the number of dots per laser exposure, 100 beam spots are used for modifying a spinning fused silica disc. Instead of placing in a square matrix as previous setups, the spots have to be positioned along a straight line in order to fit the rotation disc (Figure 7.28). The disc is separated into many concentric tracks (Figure 7.28), which are the smallest write/read data blocks for the optical storage.

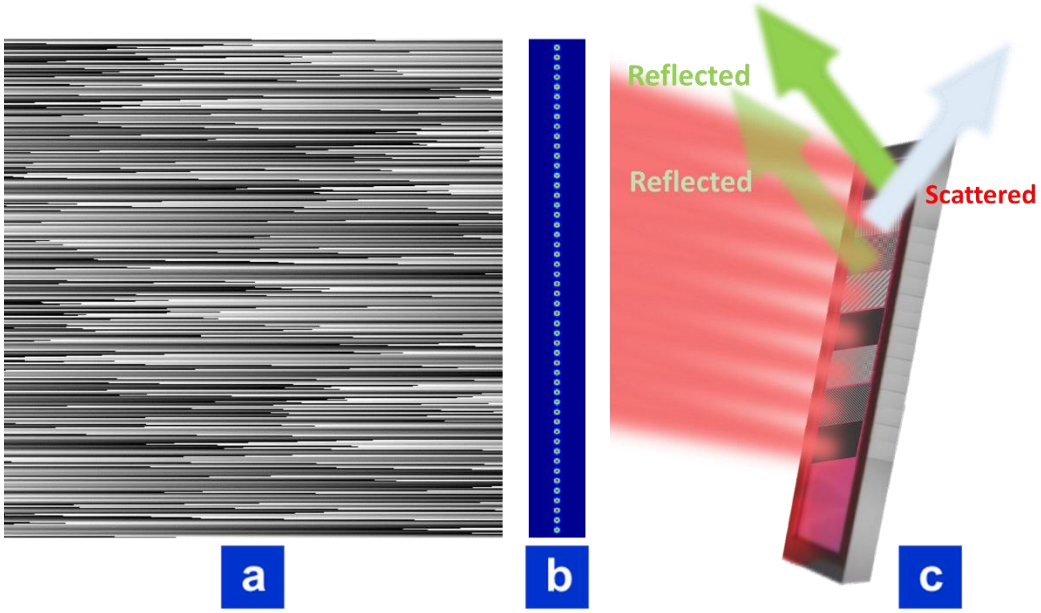

Figure 7.29 (a) Hologram for the phase mask. (b) Simulated intensity profile. (c) Schematic drawing of a line of beams irradiating on the SLM.

The writing setup for this approach is similar to the setup in Figure 7.26, except a phase mask with newly designed hologram and a SLM with narrow screen. This spots array is produced by the hologram (Figure 7.29 (a)) generated based on GSW algorithm. The simulation results show a column of isotropic beam spots separated by a same distance (Figure 7.29 (b)). And the screen of the EASLM is divided into 100×1 separate square areas (Figure 7.29 (c)). Each area operates in the same manner as in the previous setup (Figure 7.27).

Based on Equation7-1, the writing speed can reach 150Mbit/s by using the system in Figure 7.28:

$$S = D \times N_s \times N_e$$
$$= 150\ Mbit/s$$

D, 6 bits per spot (4 states for polarization states and 16 states of retardance).

N_s, equals to 25 (100 spots divided by four states). The multiple beam approach is implemented in order to increase the writing speed.

N_e, The ultrashort laser oscillators operating at megahertz and only single pulse is required for generating sufficient birefringent signal.

Four laser writing setups have been illustrated in this section and can be summarized as follows:

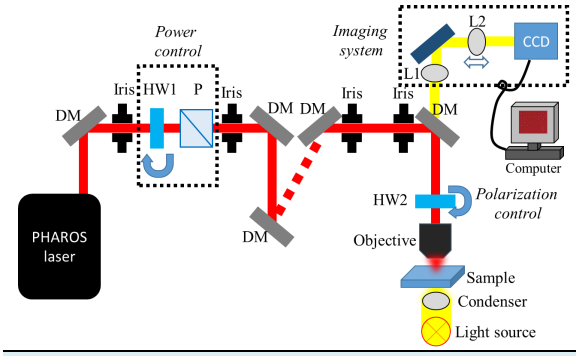	**1. Direct-writing setup** Conventional intensity and polarization control using polarization optics is relatively slow. The writing speed is less than 1 bits/s.
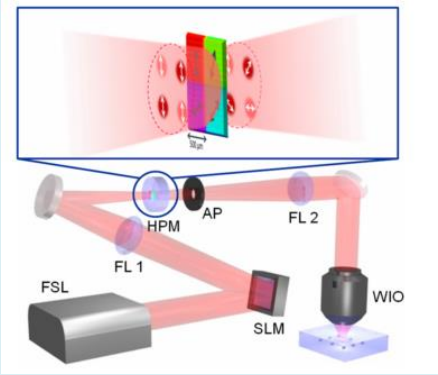	**2. EASLM and half-wave plate matrix** The current speed is subject to the synchronization of stage, laser and EASLM. The maximum speed (6KB/s) is limited by the refresh rate of EASLM.
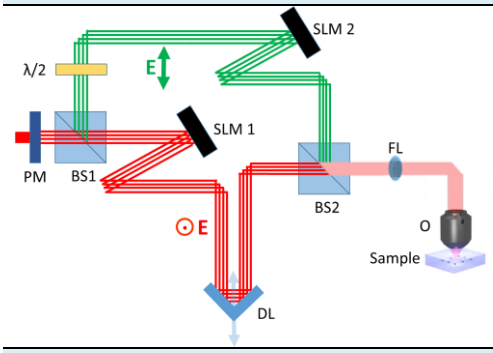	**3. Two orthogonal polarizations** The maximum speed is around $800\,Kbit/s$, which is limited by the movement of translation stage.
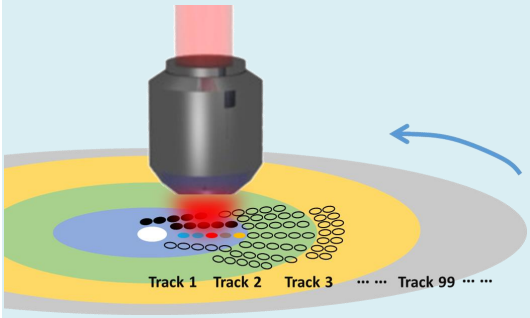	**4. Rotary writing** Assuming single laser pulse is enough to introduce birefringent spot in fused silica. The maximum speed is about $150\,Mbit/s$, which is limited by the repetition rate of the ultrafast laser.

Table 2 Schematic illustrations of four writing setups.

7.6.2 Readout system

The Abrio birefringence measurement system in our lab was demonstrated in Section 2.2 (Setup for the birefringence measurements). However, like many commercialized birefringence measurement systems, it requires electrically controlled retarders and several intensity images to retrieve the birefringence distribution. Therefore, it is not suitable for memory readout system, where a high sampling rate is essential.

To overcome this problem, we need a system enables real-time birefringence measurements. And the system proposed by T.Onuma and Y.Otani [166] is suitable for such purpose (Figure 7.30). The core device in this system is a matrix of four linear polarizers with their optical axes oriented at 0˚, 45˚, 90˚ and 135˚ respectively. Similar to a Bayer mask used in colour-sensitive camera with four independent colour filters assembled into one pixel, the matrix operates as a linear polarizer with four separate orientations. In addition, by applying the technology based on ultrafast laser nanostructuring, the analysers of tens of micrometres size with different orientations were fabricated [104]. The half-wave plates oriented at 0˚, 22.5˚, 45˚, 67.5˚ and a linear polarizer are equivalent to the four linear polarizers as required. Each polarizer matches each pixel of the CCD matrix one by one (Figure 7.30).

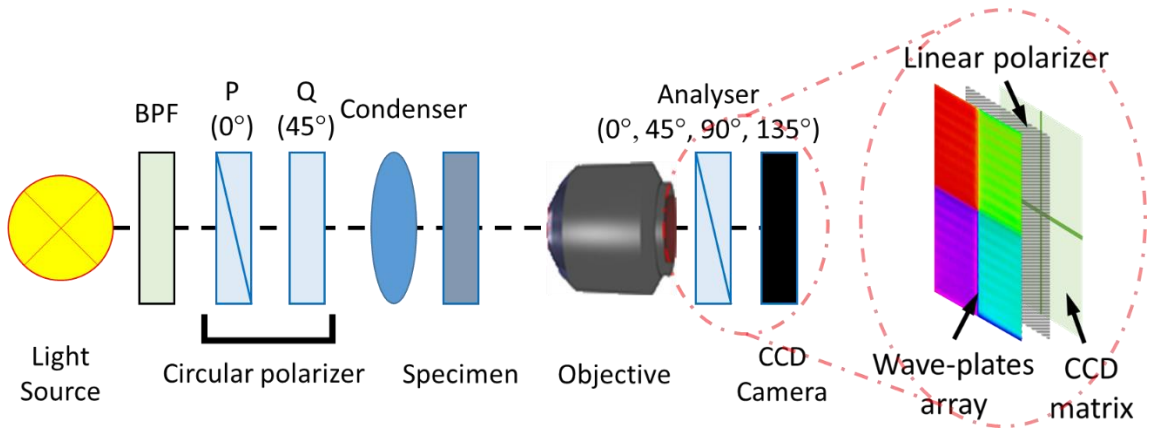

Figure 7.30 Schematic drawing of fast birefringence measurement system. BPF, band-pass filter for 546nm; P, linear polarizer; Q, quarter-wave plate. The colours of the wave-plates array indicate different slow axis orientations.

Assuming S and S' are the Stokes parameter for the incident and outgoing light, then the stokes parameter for all components on the path can be expressed as [166–168]:

Linear polarizer with zero degree angle,

$$P_0 = \frac{1}{2}\begin{bmatrix} 1 & 1 & 0 & 0 \\ 1 & 1 & 0 & 0 \\ 0 & 0 & 0 & 0 \\ 0 & 0 & 0 & 0 \end{bmatrix} \quad \text{Equation 7-5}$$

Quarter-wave plate with 45 degree angle,

$$Q_{45} = \begin{bmatrix} 1 & 0 & 0 & 0 \\ 0 & 0 & 0 & -1 \\ 0 & 0 & 1 & 0 \\ 0 & 1 & 0 & 0 \end{bmatrix} \quad \text{Equation 7-6}$$

Sample with unknown azimuthal orientation $'\gamma'$ and phase retardance $'\delta'$,

$$X_{\gamma,\delta} = \begin{bmatrix} 1 & 0 & 0 & 0 \\ 0 & cos^2(2\gamma) + sin^2(2\gamma) * \cos(\delta) & \sin(2\gamma)\cos(2\gamma)(1-\cos(\delta)) & -\sin(2\gamma)\sin(\delta) \\ 0 & \sin(2\gamma)\cos(2\gamma)(1-\cos(\delta)) & sin^2(2\gamma) + cos^2(2\gamma) * \cos(\delta) & \cos(2\gamma)\sin(\delta) \\ 0 & \sin(2\gamma)\sin(\delta) & \cos(2\gamma)\sin(\delta) & \cos(\delta) \end{bmatrix} \quad \text{Equation 7-7}$$

Linear polarizer with its optical axis set at θ,

$$A_\theta = \frac{1}{2}\begin{bmatrix} 1 & \cos(2\theta) & \sin(2\theta) & 0 \\ \cos(2\theta) & cos^2(2\theta) & \sin(2\theta)\cos(2\theta) & 0 \\ \sin(2\theta) & \sin(2\theta)\cos(2\theta) & sin^2(2\theta) & 0 \\ 0 & 0 & 0 & 0 \end{bmatrix} \quad \text{Equation 7-8}$$

The Stoke parameters of the incident and outgoing light follow:

$$S' = A_\theta \, X_{\gamma,\delta} \, Q_{45} \, P_0 \, S \quad \text{Equation 7-9}$$

Therefore,

$$\begin{bmatrix} S'_0 \\ S'_1 \\ S'_2 \\ S'_3 \end{bmatrix} = \frac{1}{2}\begin{bmatrix} (S_0 + S_1)[1 - \sin(2\gamma)\sin(\delta)\cos(2\theta) + \cos(2\gamma)\sin(\delta)\sin(2\theta)] \\ (S_0 + S_1)[\cos(2\theta) - \sin(2\gamma)\sin(\delta)\, cos^2(2\theta) + \cos(2\gamma)\sin(\delta)\sin(2\theta)\cos(2\theta)] \\ (S_0 + S_1)[\sin(2\theta) - \sin(2\gamma)\sin(\delta)\sin(2\theta)\cos(2\theta) + \cos(2\gamma)\sin(\delta)\, sin^2(2\theta)] \\ 0 \end{bmatrix} \quad \text{Equation 7-10}$$

$$S'_0 = \frac{1}{2}(S_0 + S_1)[1 - \sin(2\gamma)\sin(\delta)\cos(2\theta) + \cos(2\gamma)\sin(\delta)\sin(2\theta)]$$ Equation 7-11

I_1, I_2, I_3, I_4 are intensities of light measured after the linear polarizers oriented at 0°, 45°, 90° and 135° respectively. Therefore, the phase retardance $'\delta'$ and azimuthal orientation $'\gamma'$ can be delivered:

$$\gamma = \frac{1}{2}\arctan\left(\frac{I_3 - I_1}{I_2 - I_4}\right)$$ Equation 7-12

$$\delta = sin^{-1}\frac{2\sqrt{(I_3 - I_1)^2 + (I_2 - I_4)^2}}{I_1 + I_2 + I_3 + I_4}$$ Equation 7-13

The range of azimuthal orientation $'\gamma'$ is ±90° and that of phase retardance $'\delta'$ is quarter-wave of the wavelength of the light (136.5nm).

There is no restriction to fabricating half wave-plates segments the same size as pixels in normal CCD detector [104]. Therefore, the resolution of the measurements would not be limited. In addition, the sampling rate of the system can reach 1.3MHz by applying high-speed image sensor technique [166]. Therefore, assuming each birefringent spot contains data of 8bits and only one 2×2 pixels analyser is employed, then the readout speed would achieve 10.4Mbit/s. Such speed is equivalent to the readout speed of a normal DVD (10.5Mbit/s (1×)). For high speed readout (100Mbit/s), multiple birefringent spots can be measured simultaneously by applying more analysers.

7.7 Conclusions

Successful implementation of recording and readout of the 5D multiplexed optical data storage in silica glass was demonstrated. 11664 bits data were recorded in three layers and only 42 bits errors were obtained (0.36% error rate). The polarization dependence of retardance strength, due to spatio-temporal distortion of the laser pulse, was observed and resulted in some repeated errors during data retrieve. The calibration was implemented and reduced the error rate from 0.36% to 0.22%. A new set of experiment was performed demonstrating the optimization process and meanwhile increasing the capacity four times to 72GB/disc.

We proved unambiguously the viability of fused quartz as high-density and, assuming the scaling of Arrhenius plot holds, long-lifetime storage medium. The storage allows hundreds of terabytes per disc data capacity, thermal stability up to 1000˚C and nearly unlimited lifetime at room temperature. We believe 5D optical memory, due to its green characteristics, high capacity and long lifetime, is the ideal data storage solution for the future. Although the current recording/readout speed is relatively slow comparing with the techniques on the market, I have proposed some promising solutions to achieve a reasonable recording/readout speed.

Chapter 8: Conclusions and future work

In this thesis, I have reported my work related to polarization sensitive ultrafast laser material interactions: material interaction with longitudinal electric field, anisotropic local field enhancement on crystalline silicon, nanogratings and 5D optical data storage. We believe that optical data storage, well known for its green characteristics, will be the mainstream technique for data archiving in the near future. Therefore, one ultimate task of this thesis was to find out a high density optical data recording technology based on polarization sensitive ultrafast laser modification.

The holograms for the SLM were generated in order to manipulate beam intensity profile either in free space or in the focal plane. Algorithms such as the weighted Gerchberg-Saxton and its adapted form were illustrated. These algorithms were applied for longitudinal electric field generation and 5D optical data recording. The adapted algorithm could be employed for optical tweezers and parallel laser writing.

We noticed that the radially polarized beam with an annular intensity profile could generate a stronger longitudinal electric field compared to the beam with a Gaussian intensity distribution. The annular shaped radially polarized beam can be generated by combining an EASLM with an S-waveplate. Theoretically, the ratio of the generated longitudinal and transverse light intensities in an immersion medium is around 0.58 for 0.65 NA dry objective and 2.5 for 1.2 NA water immersion objective lens. The materials interaction with the longitudinal electric field was later inspected. The second harmonic generation in the z-cut lithium niobate crystal was experimentally demonstrated. The SH patterns were observed for both focused radially and azimuthally polarized beams with annular shaped intensity distribution, while the pronounced longitudinal component in the radially polarized beam results in ~70% higher SH power in comparison with that produced by the azimuthally polarized beam. Based on the theoretical analysis, the difference in the generated SH patterns originated from the longitudinal component of the first harmonic light field. The experimental SH patterns matched well with the simulation results based on second order susceptibility tensor.

In fused silica, the nanogratings induced form birefringence was applied to map the complex polarization state of focused light in three dimensions. The form birefringence with a slow axis oriented perpendicular to the longitudinal field was observed. This observation also indicated the existence of the longitudinal field component.

However, the evidence of the longitudinal field was not found in single pulse experiments with amorphous silicon film and crystalline silicon when we were trying to map the profile of the field intensity. This phenomenon was due to a refractive index mismatch at the interface, strongly affecting the light field that oscillates perpendicular to the surface. We experimentally and theoretically proved that the longitudinal electric field is not effective for modifying flat surfaces of materials with high refractive index when irradiating from a low index medium. The ratio of the longitudinal components in the first and second medium should equal to a factor of $\varepsilon 2/\varepsilon 1$ (~7.4 for water/silicon interface), where $\varepsilon 1$ and $\varepsilon 2$ are the dielectric constants of the medium on each side of the interface. Whereas, the experimental and theoretical results revealed that the transverse electric field propagated through the interface without significant amplitude changes.

A nanopillar structure was formed on crystalline silicon after the single pulse irradiation of tightly focused radially polarized beam. The induced nanopillar, which emerged along the beam propagation direction, showed a height of around 400nm above the crater's surface. The nanostructure was subsequently ablated during the second pulse irradiation due to the enhanced transmission of the longitudinal field along the distorted interface. Therefore, this observation indicated that revealing of the longitudinal electric field requires needle shaped structures that have fewer surfaces perpendicular to the beam propagation direction.

By investigating ultrafast laser modifications induced by single and double linearly polarized pulse on crystalline silicon, we have noticed that isotropic crater structures were generated by the single pulse irradiation. The generated structure with its smooth surface could be implemented as an optical microreflector with a focal length of 1.345 ± 0.04 μm. An array of multiple microreflectors was implemented as a wavefront sensor. After estimating the

position of the geometrical focus, the map indicating the wavefront of illumination light source was extracted.

Unexpectedly, a completely different polarization sensitive anisotropic structure was observed after double pulse irradiation. The size and orientation of the anisotropic structure can be independently controlled by energy and polarization of the pulse. The formation mechanism of the anisotropic structures may be explained on the basis of an anisotropic near-field distribution dominated for different regions of structure within the surface-wave modes and the field coupling to the waveguided modes of the aperture. If implementing this polarization sensitive structuring on silicon for data storage applications, a CD-sized disc with the capacity of 36GB could be achieved.

However, the planar technology is limited in the number of multiplexing dimensions and consequently restricts the data capacity. The laser-induced nanogratings, which lead to form birefringence, were explored for the optical recording of information beyond three spatial coordinates. Our experimental results indicated that short pulse durations (280fs), 400 pulses and high NA immersion objectives are more suitable for 5D optical recording. The stress-induced birefringence was observed around the modification spot after laser irradiation. The slow axis orientation of stress-induced birefringence was parallel to the direction of stress. Different shapes of stress-induced birefringence were observed and explained by material expansion at different conditions depending on laser energy and number of pulses.

The writing speed for 5D optical data storage was less than 1bit/s due to the conventional intensity and polarization control using polarization optics. Therefore, we designed a new writing setup involving an EASLM and a half-wave plate matrix. This setup, which enabled motion-free polarization and intensity control, eventually increased the data writing speed by almost 2 orders of magnitude. By implementing this setup with a unique writing procedure, 11664 bits data were recorded in three modification layers and only 42 bits errors were obtained (0.36% error rate). The readout procedure of the recorded data was simultaneously demonstrated. The polarization dependence of retardance strength, due to spatio-temporal distortion of the laser pulse, was observed and resulted in some repeated errors during data retrieve. The birefringent spots could have significant different values of retardance by same energy when the

incident polarizations were different. Additionally, the ratio of the strength of phase retardance between two energy levels ranged from about 2:1 to 4:1 depending on slow axis orientation. A new set of experiments was performed demonstrating the optimized readout process. During the new readout process, predefined retardance reference values were set differently according to the slow axis orientations. Therefore, the error rate was ultimately reduced from 0.36% to 0.22%. Meanwhile, a body-centered cubic arrangement of the birefringent dots leads to less stress and eventually an increase in the capacity by four times to 72GB/disc.

We proved unambiguously the viability of fused quartz as high-density and, assuming the scaling of Arrhenius plot holds, long-lifetime storage medium. The storage allows hundreds of terabytes per disc data capacity, thermal stability up to 1000°C and nearly unlimited lifetime at room temperature. It could be applied for cloud computing and long-term data storage, where vast amount of data need to be stored in a limited and reliable medium. The ultimate capacity of 5D optical data storage could be achieved by employing a laser with shorter wavelength and an objective lens with higher NA. We could obtain 360 TB for 5D storage in 1200 layers for a typical disc with 1.2 mm thickness. The ultra-long-focal-depth laser writing could be realized by adding the Fresnel lens's phase pattern to the existing holograms.

Although the recording/readout speed was relatively slow in comparison with the techniques on the market, this writing setup was only a prototype under experimental conditions. Some solutions were proposed in order to achieve a reasonable recording speed up to possible 150Mbit/s. The method of multiple beam spots parallel writing must be employed for the purpose of reducing the influence of low repetition rate. The polarization manipulation could be achieved by controlling the intensity distributions of two orthogonal polarizations or by a half-wave plate matrix. The fast manipulation of light intensity could be realized by combining a phase mask and an SLM with higher refresh rate. Two motion systems, namely, a 3D translation system and a rotary system, were introduced and could be implemented into the writing setup at different conditions. The high cost and hard to operate femtosecond laser source could be an obstacle for commercializing 5D data storage in the near future. Whereas, an ultrafast fiber

laser system with its low cost and easy operational features are promising for 5D optical data storage system.

A real time readout system with a speed of 100Mbit/s was illustrated. The core of this system is a ultrafast laser written micro-waveplate array. Multiple birefringent spots can be measured simultaneously by applying this system.

In order to turn the 5D optical memory into a commercially viable technology, the future work should focus on three main directions: 1. To reduce number of pulses required for generating birefringent spots. 2. To build an upgraded data recording setup involving parallel laser writing and rotary stage. 3. To build, test and implement the setup for real-time readout.

Our major breakthroughs consisted of:

- Demonstration of an adapted weighted Gerchberg-Saxton algorithm for 5D optical data recording.
- Theoretical demonstration of longitudinal electric field generation by tightly focused annular shaped radially polarized beam.
- Demonstration of the existence of longitudinal electric field by second harmonic generation in Lithium niobate.
- Experimental and theoretical proof of the discontinuity of longitudinal field at the high-index-contrast interfaces.
- Demonstration of a wavefront sensor by imprinting an array of micro-craters.
- Observation, characterization and explanation of a new type of anisotropic structure on silicon produced by the linearly polarized femtosecond double pulses.
- Determined the laser writing parameters for 5D optical data storage. Attempted to explain the stress-induced birefringence observed during the writing process.
- Demonstration of 5D optical memory based on laser induced nanogratings. Demonstration of the writing and readout process of 5D optical storage.
- Observed the polarization dependence of retardance strength and reduced the error rate by additional calibration procedures.

Appendix A

Appendix A contains all example codes for hologram generation and data writing: Fourier transform, Fourier propagation, Adapted weighted Gerchberg-Saxton algorithm for optical memory application and Aerotech translation stage NView software.

Fourier transform:

```
% Main code for the function of Fourier transform
function result = fun_FT_Objective(input,n,fl, ql)
if n ==1
result = fftshift(fft2(input));
elseif n ==-1
result = ifft2(ifftshift(input));
end;
```

Fourier propagation:

```
% Main code for the function of Fourier propagation
function u1 = fun_fpropagation(u0,H)
U = fft2(u0);
shiftU = fftshift(U).*H;
U = ifftshift(shiftU);
u1 = ifft2(U);
```

Adapted weighted Gerchberg-Saxton algorithm for optical memory application:

```
% This is only some segments of the code
% Open the file and read it
fid = fopen('postdeadline.pdf');
F_nums = fread(fid, 1113701);
fclose(fid);

% define a minimum writing matrix: 10*10 dots, each dot contains
3bits,total number of layer is three
width = 10;
bitperspot = 3;
bitpermatrix = width*width*bitperspot;
binstring=dec2bin(F_nums,8);
[sizex,sizey] = size(binstring);
totalsizeofbin = sizex*sizey;
numberoflayer = 3;
layer =3;
numberofmatrix = ceil(totalsizeofbin/(bitpermatrix*numberoflayer));

% To find out the total amount of the writing matrix
```

```
numberofmatrix = ceil(sqrt(numberofmatrix))^2;
stringbin=dec2bin (zeros(bitpermatrix*numberofmatrix,1));


% Encrypt the data into intensity and polarization information, and
assign the values into 'intmatrix' and 'polmatrix'
for i = 1:(numberofmatrix*bitpermatrix/bitperspot)
        if stringbin((bitperspot*(i-1)+1))=='1';
    t = mod(i,datawidth);
    if t ==0;
        t=datawidth;
    end;
  intmatrix(ceil(i/datawidth),t) =firstvalue;
elseif stringbin((bitperspot*(i-1)+1))== '0';
 t = mod(i,datawidth);
    if t ==0;
        t=datawidth;
    end;
  intmatrix(ceil(i/datawidth),t) =secondvalue;
end;

polstate=str2num(stringbin((bitperspot*(i-1)+2):(bitperspot*(i-
1)+bitperspot)));
polmatrix(ceil(i/datawidth),t)=1+polstate(2)*1+polstate(1)*2;
end;
imagesc(intmatrix);

intmatrix_cal =
double(uint8(secondvalue*zeros(datawidth+width*1,datawidth+width*1)));
polmatrix_cal = ceil(4*zeros(datawidth+width*1,datawidth+width*1))*1;

% Make two brand new matrixes as there are empty edges.
intmatrix_cal((width*1/2+1):datawidth+width*1/2,(width*1/2+1):datawidt
h+width*1/2)=intmatrix;
polmatrix_cal((width*1/2+1):datawidth+width*1/2,(width*1/2+1):datawidt
h+width*1/2)=polmatrix;

% define the polarization matrix as the half-wave plate matrix
% implemented in writing setup.
polmatrix_set =zeros(width,width);
for i = 1:width
if i <= width/2
polmatrix_set(i,:)= [1 1 1 1 1 2 2 2 2 2];
elseif i>=width/2
polmatrix_set(i,:)= [3 3 3 3 3 4 4 4 4 4];
end;
end;

% Define the parameters in order to construct a target
% intensity distribution profile for generating holograms
seperation = 12;
totalspotperline = 10;
linepixel = (totalspotperline-1)*seperation+1;
meanvaluetarget=1.2e+8;

% Define the total iteration time of inner and outer iteration.
outeriterationtime =
(sqrt(numberofmatrix)*2+1)*(sqrt(numberofmatrix)*2+1);
inneriterationtime =100;
```

```
peakaverage = zeros(0,outeriterationtime);
gratings = zeros(slmscale,scale);

% Create a gratings hologram to remove the reflection from the EASLM
for g = 1:792
gratings(:,g)=1- mod(g/8,1);
end;
for outeriteration =11:outeriterationtime
str = num2str(outeriteration);
% tempi and tempj are the x, y coordinates for the specific holograms
    tempi = mod(outeriteration,sqrt(outeriterationtime));
    tempj = ceil(outeriteration/sqrt(outeriterationtime));
    if tempi ==0
    tempi = sqrt(outeriterationtime);
    end;
temppolmatrix = polmatrix_cal((tempi-
1)*width/2+1:(tempi+1)*width/2,(tempj-
1)*width/2+1:(tempj+1)*width/2)./polmatrix_set;
[rowpol,colpol] = find(temppolmatrix==1);
% if the hologram is empty it will generates an empty hologram.
if sum(rowpol)=0
    peakaverage(outeriteration) = meanvaluetarget;
imwrite(gratings,strcat('third layer/',strcat(str,'.bmp')));
elseif sum(rowpol)>0

% the main trick of the algorthim is to store couple matrixes of
% coefficient responsible to every single targeted intensity
distribution
% different values of the target intensities should be stored in
seperate matrx.

% coefficient of the first intensity value
[row,col] = find(aimage ==firstvalue);
[numberrow,~]=size(row);
tempmatrix = zeros(1,(numberrow));
coef_1stvalue = ones(1,numberrow);

% coefficient of the second intensity value
[row2,col2] = find(aimage ==secondvalue);
[numberrow2,~]=size(row2);
tempmatrix2= zeros(1,(numberrow2));
coef_2ndvalue = ones(1,numberrow2);

% another trick of the algorthim is to move extra energy into the
% background. this is done by creating a uniform background intensity
% distribution in traget intensity profile

% coefficient of the background intensity value
[rowbackground,colbackground] = find(aimage ==backgroundintensity);
[numberrowbackground,numbercolbackground]=size(rowbackground);
tempmatrixbackground = zeros(1,numberrowbackground);
coef_bgvalue = ones(1,numberrowbackground);
% the inner iteration is used for generating one hologram
corresponding to one specific matrix
for m = 1:inneriterationtime
ang (1:(totalscale-slmscale)/2,:)=0;
ang(((totalscale+slmscale)/2+1):totalscale,:)=0;
ang (:,1:(totalscale-scale)/2)=0;
ang(:,((totalscale+scale)/2+1):totalscale)=0;
```

```
% asign the phase 'ang' to the Gaussian profile beam
afterslm = exp(1i*ang).*sqrgaussian;
buffer2= afterslm ;

% do the Fourier transform
afterlens1 =fun_FT_Objective(buffer2,1,lambda,focalLength);
temp = afterlens1;
afterlens3=temp.^2;
afterlens2 = afterlens3;

if (numberrow >2)||((numberrow ==2)&&(numberrow2 >3)) ||((numberrow
==1)&&(numberrow2 >6))
% based on the coordinates from the targeted intensity profile, find
out
% the current intensity level
for indexn1 = 1:numberrow
    tempmatrix( indexn1) =  afterlens2(row(indexn1),col(indexn1));
end;
tempresult = (abs(tempmatrix));
meanvalue =  mean2(tempresult);
for indexn2 = 1:numberrow2
    tempmatrix2( indexn2) =  afterlens2(row2(indexn2),col2( indexn2));
end;

%set the coefficient of the first and second value.
 coef_1stvalue =
coef_1stvalue./((abs(tempmatrix)./meanvalue).^(1.098/2));
coef_2ndvalue =
coef_2ndvalue./((abs(tempmatrix2)./(meanvalue*secondvalue/firstvalue))
.^(1.098/2));

% find the current intensity value in the background area, where the
ultra
% intensity is deposited.
for indexnbg = 1:numberrowbackground
    tempmatrixbackground( indexnbg) =
afterlens2(rowbackground(indexnbg),colbackground( indexnbg));
end;
%set the coefficient of the background value.
coef_bgvalue =(max(meanvalue/meanvaluetarget,0.5))^2.*coef_bgvalue;


 % assign all coefficients value into a matrix the same size as the
 % targeted intensity profile. If the intensity level at one position
 % equals to the target, the coefficient will be one; if it`s smaller
the
 % coefficient will be increased. All coefficients are iterated until
the
 % get the best suitable hologram.
for  indexnbg = 1:numberrowbackground
    wmbuffer(rowbackground(indexnbg),colbackground(indexnbg)) =
coef_bgvalue(indexnbg);
end;

for  indexn1 = 1:numberrow
    wmbuffer(row(indexn1),col(indexn1)) = coef_1stvalue(indexn1);
end;
```

```
for  indexn2 = 1:numberrow2
    wmbuffer(row2(indexn2),col2(indexn2)) = coef_2ndvalue(indexn2);
end;
 ang = angle(temp);

result = exp(1i*ang).*wmbuffer./max(max(wmbuffer)).*sqraimage;

% do the inverse fourier transform
beforelens =fun_FT_Objective(result,-1,lambda,focalLength);
 ang = angle(beforelens);
end;

hologram = mod(angle(afterslm),(2*pi))./(2*pi);

image= hologram(((totalscale-
slmscale)/2+1):(totalscale+slmscale)/2,((totalscale-
scale)/2+1):((totalscale+scale)/2));
% holograms saved into a specifi folder
imwrite(image,strcat('layer/',strcat(str,'.bmp')));
end;
```

Aerotech translation stage NView software:

```
;this is the code for movement of Aerotech translation stage
;declare some variables
DVAR $MoveDistx
DVAR $MoveDisty
DVAR $MoveDistz
DVAR $MoveVel
DVAR $Temp
DVAR $Total

;declare moving distance along x axis
$MoveDistx = X_distance

; declare moving distance along y axis
$MoveDisty = Y_distance

; declare moving distance along z axis
$MoveDistz = Z_distance

; declare moving speed
$MoveVel = 0.5
$Temp = 1;
$Total = 1

; open the exe file for writing a mark
EXE "WriteMark.exe"
PSOCONTROL X RESET
; set the parameters for laser and fire
PSOPULSE X TIME 1000 500
PSOCONTROL X FIRE CONTINUOUS
LINEAR Y ($MoveDistx * 18)  F $MoveVel*5
LINEAR X ($MoveDistx * -18)
LINEAR Y ($MoveDistx * -18)
LINEAR X ($MoveDistx * 18)
```

```
PSOCONTROL X RESET
DWELL 4
LINEAR Y ($MoveDistx * 2)  F $MoveVel*2
LINEAR X ($MoveDistx * -2)

; starts to writing the memory
WHILE ($Total<sequence)
WHILE ($Temp<sequence)

; Execute Fast.exe to refresh the hologram on SLM.
EXE "C:\A3200\FAST.exe"
DWELL Certaintime

; Reset the PSO and fire the laser
PSOCONTROL X RESET
PSOPULSE X TIME Number Number
PSOCONTROL X FIRE

; Move to a new location
LINEAR X $MoveDistx*-1.5
LINEAR Y $MoveDistx*-1.5
LINEAR Z -0.000
```

Appendix B

Appendix B contains all example codes for calculating the filed distribution in the focal plane of a tightly focused cylindrical vector beams and the corresponding second harmonic generated in $LiNbO_3$.

Azimuthally polarized beam:

```
% below is the main code for calculating the beam distribution of a
focused azimuthally polarized beam

% alpha and belta are angles for annular shaped beams
angle3 = alpha;
angle4 = belta;

% integration of the transverse field
d_transverse =@(alpha)  A* sqrt(cos(alpha)).*
sin(alpha).*besselj(besselkindp,kfactor*sin(alpha).*z(k)).*exp(1i*kfac
tor .*cos(alpha)*z(l)).*beam_intensity_distribution(alpha);

E_transverse (k,l) = 2*(- integral(d_transverse,  angle3, angle4));
```

Radially polarized beam:

```
% below is the main code for calculating the beam distribution of a
focused radially polarized beam

% alpha and belta are angles for annular shaped beams
angle3 = alpha;
angle4 = belta;

% integration of the transverse field
d_transverse =@(alpha)  A* sqrt(cos(alpha)).*
sin(2*alpha).*besselj(besselkindp,kfactor*sin(alpha).*z(k)).*exp(1i*kf
actor .*cos(alpha)*z(l)).*gau(alpha);

E_transverse (k,l) =+integral(d_transverse,angle3,angle4);

% integration of the longitudinal field
d_longitudinal =@(alpha)  A* sqrt(cos(alpha)).*
(sin(alpha).^2).*besselj(besselkindz,kfactor*sin(alpha).*z(k)).*exp(1i
*kfactor .*cos(alpha)*z(l)).*gau(alpha);

E_longitudinal (k,l) =2*1i*(+integral(d_longitudinal,angle3,angle4));
```

SHG in Lithium Niobate:

```
% Below is part of the main code for SHG in Lithium Niobate
% calculation


%Assign values from second order susceptibility equation
d22 = 2.7;
d31 = 4.5;
d33 = 28.5;
A = [0 0 0 0 d31 -d22; -d22 d22 0 d31 0 0; d31 d31 d33 0 0 0];

% Define the size for the simulation matrix
scale = A_certain_Number;
n_x = scale ;
n_y = scale ;
n_z = scale ;
f_x = linspace(-1,1,n_x);
f_y = linspace(-1,1,n_y);
[X,Y] = meshgrid(f_x,f_y);
Z= Y./X;

% The value of EX, EY and EZ are derived from the simulation results
% of focused radially and azimuthally polarized beam respectively
Column_1= [EX.^2];
Column_2= [EY.^2];
Column_3 = [EZ.^2];
Column_4= [2*EY.*EX];
Column_5=[2*EX*EZ];
Column_6=[2*EX*EY];

I(1,:,:)= [Column_1];
I(2,:,:)= [Column_2];
I(3,:,:)= [Column_3];
I(4,:,:)= [Column_4];
I(5,:,:)= [Column_5];
I(6,:,:)= [Column_6];

% Px, Py and Pz are calculated
for m = 1:scale
    for n = 1:scale
        Px(m,n)
=A(1,:)*[I(1,m,n);I(2,m,n);I(3,m,n);I(4,m,n);I(5,m,n);I(6,m,n);];
        Py(m,n)
=A(2,:)*[I(1,m,n);I(2,m,n);I(3,m,n);I(4,m,n);I(5,m,n);I(6,m,n);];
        Pz(m,n)
=A(3,:)*[I(1,m,n);I(2,m,n);I(3,m,n);I(4,m,n);I(5,m,n);I(6,m,n);];
    end;
end;
```

Appendix B

Appendix C

In Appendix C, the MATLAB code of reading raw data from Abrio Birefringence image is given below:

```
% Open the bmp file of birefringent retardance
Raw_retardance_profile = ((rgb2gray(imread('the path of phase
retardance profile is given here'))));
% rotate and crop the raw image.
imageangle=imrotate(Raw_retardance_profile,-0.5);
temp_Retardance = imageangle(245:765,410:930,:);

% Open the bmp file of birefringent slow axis orientation
Raw_slowaxis_profile = (((imread('the path of slow axis profile is
given here'))));
% rotate and crop the raw image.
azimthalanglue=imrotate(Raw_slowaxis_profile,-0.5);
temp_Slowaxis  = azimthalanglue(245:765,410:930,:);

% readout the birefringent signal by finding X Y corrdinates of the
highest retardance value
% in target area
for i = 1:Matrix_size
    for j =1:Matrix_size
    tempmatrix = (temp_Retardance(Y(i,j)-4:Y(i,j)+4,X(i,j)-
4:X(i,j)+4));
    [row,col] = find(tempmatrix == max(max(tempmatrix )));
resultre(i,j) = mean(mean((temp_Retardance(Y(i,j)+row(1)-temp-
temp2:Y(i,j)+row(1)-temp+temp2,X(i,j)+col(1)-temp-temp2:X(i,j)+col(1)-
temp+temp2))));
resultsa(i,j) = mean(mean(temp_Slowaxis(Y(i,j)-temp+row(1)-
temp3:Y(i,j)-temp+row(1)+temp3,X(i,j)-temp+col(1)-temp3:X(i,j)-
temp+col(1)+temp3)));
end;
end;

% uniform the phase retardance value
for i = 1:Matrix_size
    for j =1:Matrix_size
resultfn((i-1)*b+1:i*b,(j-1)*b+1:j*b) =resultre((i-1)*b+1:i*b,(j-
1)*b+1:j*b)./max(max(resultre((i-1)*b+1:i*b,(j-1)*b+1:j*b)));
    end;
end;


% determine the retardance strength level of each spot
for i = 1:Matrix_size
    for j =1:Matrix_size
if resultfn (i,j)>Here_is_the_value_determine_the_levels_of_retardance
    result_Retardance(i,j) =1;
else
    result_Retardance(i,j)=0;
end;
    end;
end;
```

Appendix C

```
% determine the slow axis orientation level of each spot
for i = 1:36
    for j =1:36
if (resultsa (i,j)>=0.014)&&(resultsa (i,j)<0.32) %    5 2
    result_Slowaxis(i,j)=2;
    elseif (resultsa (i,j)>0.32)&&(resultsa (i,j)<0.5)
    result_Slowaxis(i,j)=1;
    elseif (resultsa (i,j)>0.5)&&(resultsa (i,j)<0.8)
    result_Slowaxis(i,j)=3;
    elseif (resultsa (i,j)>0.8)&&(resultsa (i,j)<=1.0)||((resultsa
(i,j)>=0)&&(resultsa (i,j)<0.014))
    result_Slowaxis(i,j)=4;
end;
    end;
end;
% result_Retardance and result_Slowaxis are two matrixes contain
% the readout raw data, they can be decrypted into binary data and
% later compared with the original data.
```

List of Publications

Journal publications

[1] **J. Zhang**, R. Drevinskas, M. Beresna, P. G. Kazansky
Polarization sensitive anisotropic structuring of silicon by ultrashort light pulses
Applied Physics Letters, 107 (4), 041114, (2015)

[2] R. Drevinskas, **J. Zhang**, M. Beresna, M. Gecevičius, A. G. Kazanskii, Y.P. Svirko, P. G. Kazansky
Laser Material Processing with Tightly Focused Cylindrical Vector Beams
Applied Physics Letters, 108 (22), 221107, (2016)

[3] **J. Zhang,** M. Gecevičius, M. Beresna, P. G. Kazansky
Seemingly unlimited lifetime data storage in nanostructured glass
Physical review letters, 112 (3), 033901,(2014)

[4] M. Gecevičius, M. Beresna, **J. Zhang**, W. Yang, H. Takebe, P. G. Kazansky
Extraordinary anisotropy of ultrafast laser writing in glass
Optics express, 21 (4), 3959-3968, (2013)

Conference publications

[1] **J. Zhang**, A. Čerkauskaitė, R. Drevinskas, A. Patel, M. Beresna, P. G. Kazansky
Eternal 5D data storage by ultrafast laser writing in glass
SPIE. Photonics West, 9736-29 (2016) (Invited Paper)

[2] **J. Zhang**, R. Drevinskas, M. Beresna, M. Gecevičius, P. G. Kazansky
Silicon Microreflector Created by Single Ultrafast Laser Pulse
CLEO: Applications and Technology, San Jose, JTh2A. 138 (2014)

[3] **J. Zhang**, R. Drevinskas, M. Beresna, M. Gecevičius, P. G. Kazansky
Polarization-Sensitive Cats Eye Structuring of Silicon by Ultrashort Light Pulses
CLEO: Science and Innovations, San Jose, STh1J. 3 (2014)

[4] P. G. Kazansky, **J. Zhang**, M Gecevičius, M Beresna

Recent advances in ultrafast laser nanostructuring: S-waveplate and eternal data storage
CLEO: Applications and Technology, San Jose, AM3L. 3 (2014)

[5 **J.Zhang**, M.Gecevičius, M.Beresna, P.G.Kazansky
5D data storage by ultrafast laser nanostructuring in glass
CLEO/QELS, San Jose, CTh5D.9 (2013) (Postdeadline)

[6] **J.Zhang**, M.Gecevičius, M.Beresna, A.G.Kazanskii, P.G.Kazansky
Anomalous interaction of longitudinal electric field with hydrogenated amorphous silicon films
CLEO/QELS, San Jose, CM4H.7 (2013)

[7] **J.Zhang**, M.Gecevičius, M.Beresna, P.G.Kazansky
Modification of transparent materials by tightly focused annular, radially and azimuthally polarized ultrafast laser beams
CLEO/Europe-IQEC, Munich (2013)

[8] **J.Zhang**, M.Gecevičius, M.Beresna, A.G.Kazanskii, P.G.Kazansky
The puzzle of longitudinal electric field interaction with transparent media
Progress in ultrafast laser modifications of materials, Corsica (2013)

[9] P.G.Kazansky, M.Beresna, M.Gecevičius, **J.Zhang**, A.Patel, R.Drevinskas, A.Kazanskii
Recent progress in ultrafast laser nanostructuring: from two-plasmon decay to longitudinal field puzzle
Nonlinear Optics, Kohala Coast, Hawaii, USA, NF2A.4 (2013)

[10] M.Gecevičius, M.Beresna, **J.Zhang**, P.G.Kazansky
Polarization dependence of area scanning ultrafast laser machining
CLEO/QELS, San Jose, CM4K.6 (2012)

Bibliography

1. T. H. Maiman, "Stimulated Optical Radiation in Ruby," Nature **187**, 493–494 (1960).
2. D. E. Spence, P. N. Kean, and W. Sibbett, "60-fsec pulse generation from a self-mode-locked Ti:sapphire laser.," Opt. Lett. **16**, 42–44 (1991).
3. U. Keller, D. a Miller, G. D. Boyd, T. H. Chiu, J. F. Ferguson, and M. T. Asom, "Solid-state low-loss intracavity saturable absorber for Nd:YLF lasers: an antiresonant semiconductor Fabry-Perot saturable absorber.," Opt. Lett. **17**, 505–507 (1992).
4. K. M. Davis, K. Miura, N. Sugimoto, and K. Hirao, "Writing waveguides in glass with a femtosecond laser.," Opt. Lett. **21**, 1729–1731 (1996).
5. A. H. Zewail, "Laser femtochemistry.," Science **242**, 1645–53 (1988).
6. W. Denk, J. Strickler, and W. Webb, "Two-photon laser scanning fluorescence microscopy," Science **248**, 73–76 (1990).
7. R. Birngruber, C. a. Puliafito, A. Gawande, W. Z. Lin, R. W. Schoenlein, and J. G. Fuiimoto, "Femtosecond laser-tissue interactions: Retinal injury studies," IEEE J. Quantum Electron. **23**, 1836–1844 (1987).
8. C. D'Amico, A. Houard, M. Franco, B. Prade, A. Mysyrowicz, A. Couairon, and V. T. Tikhonchuk, "Conical forward THz emission from femtosecond-laser-beam filamentation in air," Phys. Rev. Lett. **98**, 8–11 (2007).
9. Y. Shimotsuma, P. G. Kazansky, J. Qiu, and K. Hirao, "Self-Organized Nanogratings in Glass Irradiated by Ultrashort Light Pulses," Phys. Rev. Lett. **91**, 247405 (2003).
10. M. Shribak and R. Oldenbourg, "Techniques for fast and sensitive measurements of two-dimensional birefringence distributions.," Appl. Opt. **42**, 3009–3017 (2003).
11. S. B. Mehta, M. Shribak, and R. Oldenbourg, "Polarized light imaging of birefringence and diattenuation at high resolution and high sensitivity," J. Opt. **15**, 94007 (2013).
12. A. Jesacher, G. D. Marshall, T. Wilson, and M. J. Booth, "Adaptive optics for direct laser writing with plasma emission aberration sensing: erratum.," Opt. Express **18**, 15399 (2010).
13. E. Schonbrun, R. Piestun, P. Jordan, J. Cooper, K. Wulff, J. Courtial, and M. Padgett, "3D interferometric optical tweezers using a single spatial light modulator," Opt. Express **13**, 3777–3786 (2005).
14. H. Chen, Z. Zheng, B.-F. Zhang, J. Ding, and H.-T. Wang, "Polarization structuring of focused field through polarization-only modulation of incident beam," Opt. Lett. **35**, 2825–2827 (2010).
15. M. Bock, S. K. Das, and R. Grunwald, "Ultrashort highly localized wavepackets," Opt. Express **20**, 12563 (2012).
16. M. Zhao and X. Xie, "Generation of arbitrary vector beams with a spatial light modulator," 14th Int. Conf. Electron. Mater. Packag. EMAP 2012 **32**, 3549–3551 (2012).

17. G. Sinclair, P. Jordan, J. Leach, M. J. Padgett, and J. Cooper, "Defining the trapping limits of holographical optical tweezers," J. Mod. Opt. **51**, 409–414 (2004).

18. R. Di Leonardo, F. Ianni, and G. Ruocco, "Computer generation of optimal holograms for optical trap arrays," Opt. Express **15**, 1913–1922 (2007).

19. X. Li, Q. Zhang, X. Chen, and M. Gu, "Giant refractive-index modulation by two-photon reduction of fluorescent graphene oxides for multimode optical recording.," Sci. Rep. **3**, 2819 (2013).

20. X. Li, T.-H. Lan, C.-H. Tien, and M. Gu, "Three-dimensional orientation-unlimited polarization encryption by a single optically configured vectorial beam.," Nat. Commun. **3**, 998 (2012).

21. M. R. Beversluis, L. Novotny, and S. J. Stranick, "Programmable vector point-spread function engineering.," Opt. Express **14**, 2650–6 (2006).

22. M. Meier, V. Romano, and T. Feurer, "Material processing with pulsed radially and azimuthally polarized laser radiation," Appl. Phys. A **86**, 329–334 (2006).

23. K. Venkatakrishnan and B. Tan, "Interconnect microvia drilling with a radially polarized laser beam," J. Micromechanics Microengineering **16**, 2603–2607 (2006).

24. Y. Liu, D. Cline, and P. He, "Vacuum laser acceleration using a radially polarized CO2 laser beam," Nucl. Instruments Methods Phys. Res. Sect. A Accel. Spectrometers, Detect. Assoc. Equip. **424**, 296–303 (1999).

25. Q. Zhan, "Trapping metallic Rayleigh particles with radial polarization," Opt. Express **12**, 3377 (2004).

26. D. P. Biss and T. G. Brown, "Polarization-vortex-driven second-harmonic generation," Opt. Lett. **28**, 923 (2003).

27. R. Dorn, S. Quabis, and G. Leuchs, "Sharper Focus for a Radially Polarized Light Beam," Phys. Rev. Lett. **91**, 233901 (2003).

28. B. Hao and J. Leger, "Experimental measurement of longitudinal component in the vicinity of focused radially polarized beam.," Opt. Express **15**, 3550–6 (2007).

29. L. Yang, X. Xie, S. Wang, and J. Zhou, "Minimized spot of annular radially polarized focusing beam," Opt. Lett. **38**, 1331–1333 (2013).

30. R. R. Gattass and E. Mazur, "Femtosecond laser micromachining in transparent materials," Nat. Photonics **2**, 219–225 (2008).

31. T. Bauer, S. Orlov, U. Peschel, P. Banzer, and G. Leuchs, "Nanointerferometric amplitude and phase reconstruction of tightly focused vector beams," Nat. Photonics **8**, 23–27 (2013).

32. G. M. Lerman and U. Levy, "Effect of radial polarization and apodization on spot size under tight focusing conditions," Opt. Express **16**, 4567 (2008).

33. D. Biss and T. Brown, "Cylindrical vector beam focusing through a dielectric interface," Opt. Express **9**, 490 (2001).

34. K. Kitamura, K. Sakai, and S. Noda, "Sub-wavelength focal spot with long depth of focus generated by radially polarized, narrow-width annular beam.," Opt. Express **18**, 4518–4525 (2010).

35. X. Li, Y. Cao, and M. Gu, "Superresolution-focal-volume induced 3.0 Tbytes/disk capacity by focusing a radially polarized beam," Opt. Lett. **36**, 2510–2512 (2011).

36. K. Youngworth and T. Brown, "Focusing of high numerical aperture cylindrical-vector beams," Opt. Express **7**, 77–87 (2000).

37. W.-C. Kim, Y.-J. Yoon, H. Choi, N.-C. Park, and Y.-P. Park, "Effects of optical variables in immersion lens-based near-field optics," Opt. Express **16**, 13933 (2008).

38. C. Hnatovsky, V. Shvedov, W. Krolikowski, and A. Rode, "Revealing Local Field Structure of Focused Ultrashort Pulses," Phys. Rev. Lett. **106**, 123901 (2011).

39. C. Hnatovsky, V. G. Shvedov, N. Shostka, A. V Rode, and W. Krolikowski, "Polarization-dependent ablation of silicon using tightly focused femtosecond laser vortex pulses," Opt. Lett. **37**, 226–228 (2012).

40. F. Brunel, "Not-so-resonant, resonant absorption," Phys. Rev. Lett. **59**, 52–55 (1987).

41. H. Iwase, S. Kokubo, S. Juodkazis, and H. Misawa, "Suppression of ripples on ablated Ni surface via a polarization grating.," Opt. Express **17**, 4388–96 (2009).

42. G. D. Boyd, R. C. Miller, K. Nassau, W. L. Bond, and A. Savage, "LiNbO3: An efficient phase matchable nonlinear optical material," Appl. Phys. Lett. **5**, 234–236 (1964).

43. D. a. Roberts, "Simplified characterization of uniaxial and biaxial nonlinear optical crystals: A plea for standardization of nomenclature and conventions," IEEE J. Quantum Electron. **28**, 2057–2074 (1992).

44. P. Kazansky, H. Inouye, T. Mitsuyu, K. Miura, J. Qiu, K. Hirao, and F. Starrost, "Anomalous Anisotropic Light Scattering in Ge-Doped Silica Glass," Phys. Rev. Lett. **82**, 2199–2202 (1999).

45. B. Poumellec, M. Lancry, A. Chahid-Erraji, and P. G. Kazansky, "Modification thresholds in femtosecond laser processing of pure silica: review of dependencies on laser parameters," Opt. Mater. Express **1**, 766–782 (2011).

46. J. Ouyang, W. Perrie, O. J. Allegre, T. Heil, Y. Jin, E. Fearon, D. Eckford, S. P. Edwardson, and G. Dearden, "Tailored optical vector fields for ultrashort-pulse laser induced complex surface plasmon structuring," Opt. Express **23**, 12562 (2015).

47. A. V Emelyanov, A. G. Kazanskii, M. V Khenkin, P. A. Forsh, P. K. Kashkarov, M. Gecevičius, M. Beresna, and P. G. Kazansky, "Visible luminescence from hydrogenated amorphous silicon modified by femtosecond laser radiation," Appl. Phys. Lett. **101**, 81902 (2012).

48. R. Drevinskas, M. Beresna, M. Gecevičius, M. Khenkin, A. G. Kazanskii, I. Matulaitienė, G. Niaura, O. I. Konkov, E. I. Terukov, Y. P. Svirko, and P. G. Kazansky, "Giant birefringence and dichroism induced by ultrafast laser pulses in hydrogenated amorphous silicon," Appl. Phys. Lett. **106**, 171106 (2015).

49. A. Borowiec, M. MacKenzie, G. C. C. Weatherly, and H. K. K. Haugen, "Transmission and scanning electron microscopy studies of single

femtosecond- laser-pulse ablation of silicon," Appl. Phys. A Mater. Sci. Process. **76**, 201–207 (2003).

50. E. N. Glezer, M. Milosavljevic, L. Huang, R. J. Finlay, T. H. Her, J. P. Callan, and E. Mazur, "Three-dimensional optical storage inside transparent materials.," Opt. Lett. **21**, 2023–2025 (1996).
51. A. P. P. Joglekar, H. Liu, G. J. J. Spooner, E. Meyhöfer, G. Mourou, A. J. J. Hunt, "A study of the deterministic character of optical damage by femtosecond laser pulses and applications to nanomachining," Appl. Phys. B Lasers Opt. **77**, 25–30 (2003).
52. P. Zijlstra, J. W. M. Chon, and M. Gu, "Five-dimensional optical recording mediated by surface plasmons in gold nanorods.," Nature **459**, 410–3 (2009).
53. J. Zhang, M. Gecevičius, M. Beresna, and P. G. Kazansky, "Seemingly Unlimited Lifetime Data Storage in Nanostructured Glass," Phys. Rev. Lett. **112**, 33901 (2014).
54. M. Beresna, M. Gecevičius, and P. G. Kazansky, "Polarization sensitive elements fabricated by femtosecond laser nanostructuring of glass," Opt. Mater. Express **1**, 783 (2011).
55. Y. Bellouard, A. Said, M. Dugan, and P. Bado, "Fabrication of high-aspect ratio, micro-fluidic channels and tunnels using femtosecond laser pulses and chemical etching.," Opt. Express **12**, 2120–9 (2004).
56. J. Wang, M. S. Gudiksen, X. Duan, Y. Cui, and C. M. Lieber, "Highly polarized photoluminescence and photodetection from single indium phosphide nanowires.," Science **293**, 1455–7 (2001).
57. F. H'dhili, R. Bachelot, G. Lerondel, D. Barchiesi, and P. Royer, "Near-field optics: Direct observation of the field enhancement below an apertureless probe using a photosensitive polymer," Appl. Phys. Lett. **79**, 4019 (2001).
58. J.-M. M. Guay, A. Villafranca, F. Baset, K. Popov, L. Ramunno, and V. R. Bhardwaj, "Polarization-dependent femtosecond laser ablation of poly-methyl methacrylate," New J. Phys. **14**, 85010 (2012).
59. C. Hnatovsky, V. G. Shvedov, and W. Krolikowski, "The role of light-induced nanostructures in femtosecond laser micromachining with vector and scalar pulses.," Opt. Express **21**, 12651–6 (2013).
60. G. D. Tsibidis, M. Barberoglou, P. a. Loukakos, E. Stratakis, and C. Fotakis, "Dynamics of ripple formation on silicon surfaces by ultrashort laser pulses in subablation conditions," Phys. Rev. B **86**, 115316 (2012).
61. D. Wortmann, J. Gottmann, N. Brandt, and H. Horn-Solle, "Micro- and nanostructures inside sapphire by fs-laser irradiation and selective etching," 2008 Conf. Quantum Electron. Laser Sci. Conf. Lasers Electro-Optics, CLEO/QELS **16**, 197–200 (2008).
62. J. Bonse and J. Krüger, "Pulse number dependence of laser-induced periodic surface structures for femtosecond laser irradiation of silicon," J. Appl. Phys. **108**, 34903 (2010).
63. J. Bonse, J. Krüger, S. Höhm, and a. Rosenfeld, "Femtosecond laser-induced periodic surface structures," J. Laser Appl. **24**, 42006 (2012).

64. M. Huang, F. Zhao, Y. Cheng, N. Xu, and Z. Xu, "Origin of laser-induced near-subwavelength ripples: interference between surface plasmons and incident laser.," ACS Nano **3**, 4062–70 (2009).

65. S. Höhm, a. Rosenfeld, J. Krger, and J. Bonse, "Femtosecond laser-induced periodic surface structures on silica," J. Appl. Phys. **112**, 14901 (2012).

66. G. a Martsinovskii, G. D. Shandybina, D. S. Smirnov, S. V Zabotnov, L. a Golovan, V. Y. Timoshenko, and P. K. Kashkarov, "Ultrashort excitations of surface polaritons and waveguide modes in semiconductors," Opt. Spectrosc. **105**, 67–72 (2008).

67. A. Borowiec and H. K. Haugen, "Subwavelength ripple formation on the surfaces of compound semiconductors irradiated with femtosecond laser pulses," Appl. Phys. Lett. **82**, 4462–4464 (2003).

68. F. Liang, R. Vallée, and S. Chin, "Mechanism of nanograting formation on the surface of fused silica," Opt. Express **20**, 4389–4396 (2012).

69. G. Obara, H. Shimizu, T. Enami, E. Mazur, M. Terakawa, and M. Obara, "Growth of high spatial frequency periodic ripple structures on SiC crystal surfaces irradiated with successive femtosecond laser pulses," Opt. Express **21**, 26323 (2013).

70. S. K. Sundaram and E. Mazur, "Inducing and probing non-thermal transitions in semiconductors using femtosecond laser pulses," Nat. Mater. **1**, 217–224 (2002).

71. J. Bonse, S. Baudach, J. Krüger, W. Kautek, and M. Lenzner, "Femtosecond laser ablation of silicon-modification thresholds and morphology," Appl. Phys. A Mater. Sci. Process. **74**, 19–25 (2002).

72. Y. Jin, O. J. Allegre, W. Perrie, K. Abrams, J. Ouyang, E. Fearon, S. P. Edwardson, and G. Dearden, "Dynamic modulation of spatially structured polarization fields for real-time control of ultrafast laser-material interactions," Opt. Express **21**, 25333–25343 (2013).

73. R. W. Boyd, *Nonlinear Optics* (Academic Press, 2008).

74. D. Milam, "Review and assessment of measured values of the nonlinear refractive-index coefficient of fused silica.," Appl. Opt. **37**, 546–550 (1998).

75. L. Sudrie, a. Couairon, M. Franco, B. Lamouroux, B. Prade, S. Tzortzakis, and a. Mysyrowicz, "Femtosecond Laser-Induced Damage and Filamentary Propagation in Fused Silica," Phys. Rev. Lett. **89**, 186601 (2002).

76. L. V. Keldysh, "Ionization in the field of a string electromagnetic wave," J. Exp. Theor. Phys. **20**, 1307–1314 (1965).

77. B. Stuart, M. Feit, S. Herman, A. Rubenchik, B. Shore, and M. Perry, "Nanosecond-to-femtosecond laser-induced breakdown in dielectrics," Phys. Rev. B **53**, 1749–1761 (1996).

78. C. Corbari, A. Champion, M. Gecevičius, M. Beresna, Y. Bellouard, and P. G. Kazansky, "Femtosecond versus picosecond laser machining of nano-gratings and micro-channels in silica glass," Opt. Express **21**, 3946 (2013).

79. K. Miura, J. Qiu, H. Inouye, T. Mitsuyu, and K. Hirao, "Photowritten optical waveguides in various glasses with ultrashort pulse laser," Appl. Phys. Lett. **71**, 3329–3331 (1997).

80. C. Hnatovsky, R. S. Taylor, P. P. Rajeev, E. Simova, V. R. Bhardwaj, D. M. Rayner, and P. B. Corkum, "Pulse duration dependence of femtosecond-laser-fabricated nanogratings in fused silica," Appl. Phys. Lett. **87**, 14104 (2005).

81. L. Sudrie, M. Franco, B. Prade, and A. Mysyrowicz, "Writing of permanent birefringent microlayers in bulk fused silica with femtosecond laser pulses," Opt. Commun. **171**, 279–284 (1999).

82. Y. Shimotsuma, K. Hirao, J. Qiu, and P. G. Kazansky, "Nano-modification inside transparent materials by femtosecond laser single beam," Mod. Phys. Lett. B **19**, 225–238 (2005).

83. S. Richter, C. Miese, S. Döring, F. Zimmermann, M. J. Withford, A. Tünnermann, and S. Nolte, "Laser induced nanogratings beyond fused silica - periodic nanostructures in borosilicate glasses and ULE," Opt. Mater. Express **3**, 1161–1166 (2013).

84. F. Zimmermann, A. Plech, S. Richter, A. Tünnermann, and S. Nolte, "Ultrashort laser pulse induced nanogratings in borosilicate glass," Appl. Phys. Lett. **104**, 11–16 (2014).

85. W. J. Yang, E. Bricchi, P. G. Kazansky, J. Bovatsek, and A. Y. Arai, "Self-assembled periodic sub-wavelength structures by femtosecond laser direct writing," Opt. Express **14**, 10117–10124 (2006).

86. M. Beresna, M. Gecevičius, and P. G. Kazansky, "Polarization sensitive elements fabricated by femtosecond laser nanostructuring of glass [Invited]," Opt. Mater. Express **1**, 10117–10124 (2011).

87. V. Bhardwaj, E. Simova, P. Rajeev, C. Hnatovsky, R. Taylor, D. Rayner, and P. Corkum, "Optically Produced Arrays of Planar Nanostructures inside Fused Silica," Phys. Rev. Lett. **96**, 57404 (2006).

88. M. Lancry, B. Poumellec, J. Canning, K. Cook, J.-C. Poulin, and F. Brisset, "Ultrafast nanoporous silica formation driven by femtosecond laser irradiation," Laser Photon. Rev. **7**, 953-962 (2013).

89. H. Misawa and S. Juodkazis, *3D Laser Microfabrication: Principles and Applications* (John Wiley & Sons, Weinheim, 2006).

90. P. G. Kazansky, E. Bricchi, Y. Shimotsuma, and K. Hirao, "Self-assembled nanostructures and two-plasmon decay in femtosecond processing of transparent materials," Conf. Lasers Electro-Optics, 2007, CLEO 2007 13–15 (2007).

91. R. Buividas, L. Rosa, R. Sliupas, T. Kudrius, G. Slekys, V. Datsyuk, and S. Juodkazis, "Mechanism of fine ripple formation on surfaces of (semi)transparent materials via a half-wavelength cavity feedback.," Nanotechnology **22**, 55304 (2011).

92. M. Beresna, M. Gecevičius, P. G. Kazansky, T. Taylor, and A. V. Kavokin, "Exciton mediated self-organization in glass driven by ultrashort light pulses," Appl. Phys. Lett. **101**, 53120 (2012).

93. D. Grojo, M. Gertsvolf, S. Lei, T. Barillot, D. M. Rayner, and P. B. Corkum, "Exciton-seeded multiphoton ionization in bulk SiO2," Phys. Rev. B - Condens. Matter Mater. Phys. **81**, 212301 (2010).

94. P. Martin, S. Guizard, P. Daguzan, G. Petite, P. D'Oliveira, P. Meynadier, and M. Perdrix, "Subpicosecond study of carrier trapping dynamics in wide-band-gap crystals," Phys. Rev. B **55**, 5799–5810 (1997).

95. J. Canning, M. Lancry, K. Cook, A. Weickman, F. Brisset, and B. Poumellec, "Anatomy of a femtosecond laser processed silica waveguide," Opt. Mater. Express **1**, 998 (2011).

96. L. Bressel and D. De Ligny, "Observation of O2 inside voids formed in GeO2 glass by tightly-focused fs-laser pulses," Opt. Mater. Express **1**, 416–424 (2011).

97. A. Champion and Y. Bellouard, "Direct volume variation measurements in fused silica specimens exposed to femtosecond laser," Opt. Mater. Express **2**, 789 (2012).

98. R. S. Taylor, C. Hnatovsky, E. Simova, P. P. Rajeev, D. M. Rayner, and P. B. Corkum, "Femtosecond laser erasing and rewriting of self-organized planar nanocracks in fused silica glass," Opt. Lett. **32**, 2888–2890 (2007).

99. E. Bricchi and P. G. Kazansky, "Extraordinary stability of anisotropic femtosecond direct-written structures embedded in silica glass," Appl. Phys. Lett. **88**, 111113–111119 (2006).

100. E. Bricchi, B. G. Klappauf, and P. G. Kazansky, "Form birefringence and negative index change created by femtosecond direct writing in transparent materials," Opt. Lett. **29**, 119–121 (2004).

101. E. Bricchi, J. D. Mills, P. G. Kazansky, B. G. Klappauf, and J. J. Baumberg, "Birefringent Fresnel zone plates in silica fabricated by femtosecond laser machining.," Opt. Lett. **27**, 2200–2202 (2002).

102. M. Beresna, M. Gecevičius, P. G. Kazansky, and T. Gertus, "Radially polarized optical vortex converter created by femtosecond laser nanostructuring of glass," Appl. Phys. Lett. **98**, 201101–201103 (2011).

103. M. Gecevičius, M. Beresna, R. Drevinskas, and P. G. Kazansky, "Airy beams generated by ultrafast laser-imprinted space-variant nanostructures in glass," Opt. Lett. **39**, 6791 (2014).

104. M. Gecevičius, M. Beresna, and P. G. Kazansky, "Polarization sensitive camera by femtosecond laser nanostructuring.," Opt. Lett. **38**, 4096–9 (2013).

105. A. Champion, M. Beresna, P. Kazansky, and Y. Bellouard, "Stress distribution around femtosecond laser affected zones: effect of nanogratings orientation," Opt. Express **21**, 24942–24951 (2013).

106. B. Poumellec, L. Sudrie, M. Franco, B. Prade, and A. Mysyrowicz, "Femtosecond laser irradiation stress induced in pure silica.," Opt. Express **11**, 1070–1079 (2003).

107. L. a. Fernandes, J. R. Grenier, P. R. Herman, J. S. Aitchison, and P. V. S. Marques, "Stress induced birefringence tuning in femtosecond laser fabricated waveguides in fused silica," Opt. Express **20**, 24103 (2012).

108. M. Beresna and P. G. Kazansky, "Femtosecond laser induced vortex anisotropy," Lasers Electro-Optics Quantum Electron. Laser Sci. Conf. (QELS), 2010 Conf. 10–11 (2010).

109. M. Gu, X. Li, and Y. Cao, "Optical storage arrays: a perspective for future big data storage," Light Sci. Appl. **3**, e177 (2014).

110. A. Hylick, R. Sohan, A. Rice, and B. Jones, "An analysis of hard drive energy consumption," in 2008 IEEE International Symposium on Modeling, Analysis and Simulation of Computer and Telecommunication Systems, MASCOTS, 1-10 (2008).

111. J. Gantz and D. Reinsel, "The Digital Universe in 2020: Big Data, Bigger Digital Shadows, and Biggest Growth in the Far East.," <http://www.emc.com/leadership/digital-universe/index.htm/>.

112. F. Gan and Y. Wang, *Data Storage at the Nanoscale* (Taylor &Francis Group,LLC, 2015).

113. M. Guzman, A. M. Hein, and C. Welch, "Eternal memory: long-duration storage concepts for space," In IAC 66th International Astronautical Congress (2015).

114. G. M. Church, Y. Gao, and S. Kosuri, "Next-generation digital information storage in DNA.," Science **337**, 1628 (2012).

115. J. De Vries, D. Schellenberg, and L. Abelmann, "Towards Gigayear Storage Using a Silicon-Nitride/Tungsten Based Medium," arXiv preprint arXiv:1310.2961.,1–19 (2013).

116. Norsam Technologies, “HD-RosettaTM and Related Processes,” <http://www.norsam.com/rosetta.html/>.

117. Rosetta, “The Rosetta Project,” <http://rosettaproject.org/>.

118. S.-S. Yao, C. Weinberg, S. Bangalore, and F. a Chaudhry, "The changing paradigm of stress echocardiography: risk stratification, prognosis, and future directions.," Hosp. Pract. (1995) **38**, 26–39 (2010).

119. Panasonic, "Panasonic Develops freeze-ray Optical Disc-Based Data Archive System for Data Centers in Collaboration with Facebook," <http://news.panasonic.co.uk/news/panasonic-develops-freeze-ray-optical-disc-based-data-archive-system-for-data-centers-in-collaboration-with-facebook-144740/>

120. R. Goyal, K. Son, A. H. Torkaman, J. Nam, K. Pang, and R. Sharpe, "Optical disc library system and methods," U.S. Patent No. 8,385,163., (2012).

121. M. Gu and X. Li, "The Road to Multi-Dimensional Bit-by-Bit Optical Data Storage," Opt. Photonics News **21**, 28 (2010).

122. Z. Gan, Y. Cao, R. a Evans, and M. Gu, "Three-dimensional deep sub-diffraction optical beam lithography with 9 nm feature size.," Nat. Commun. **4**, 2061 (2013).

123. S. Wu, S. Duan, Z. Lei, W. Su, Z. Zhang, K. Wang, and Q. Zhang, "Supramolecular bisazopolymers exhibiting enhanced photoinduced birefringence and enhanced stability of birefringence for four-dimensional optical recording," J. Mater. Chem. **20**, 5202–5209 (2010).

124. G. Cipparrone, P. Pagliusi, C. Provenzano, and V. P. Shibaev, "Polarization Holographic Recording in Amorphous Polymer with Photoinduced Linear and Circular Birefringence," J. Phys. Chem. B **114**, 8900–8904 (2010).

125. H. Ditlbacher, B. Lamprecht, A. Leitner, and F. R. Aussenegg, "Spectrally coded optical data storage by metal nanoparticles," Opt. Lett. **25**, 563–565 (2000).

126. K. Miura, J. Qiu, S. Fujiwara, S. Sakaguchi, and K. Hirao, "Three-dimensional optical memory with rewriteable and ultrahigh density using the valence-state change of samarium ions," Appl. Phys. Lett. **80**, 2263–2265 (2002).

127. A. Royon, K. Bourhis, M. Bellec, G. Papon, B. Bousquet, Y. Deshayes, T. Cardinal, and L. Canioni, "Silver clusters embedded in glass as a perennial high capacity optical recording medium.," Adv. Mater. **22**, 5282–5286 (2010).

128. A. Podlipensky, A. Abdolvand, G. Seifert, and H. Graener, "Femtosecond laser assisted production of dichroitic 3D structures in composite glass containing Ag nanoparticles," Appl. Phys. A Mater. Sci. Process. **80**, 1647–1652 (2005).

129. J. Heanue, M. Bashaw, and L. Hesselink, "Volume holographic storage and retrieval of digital data," Science **265**, 749–752 (1994).

130. M. Hedstrom, "Digital preservation: a time bomb for digital libraries," Comput. Hum. **31**, 189–202 (1997).

131. K. H. Lee, O. Slattery, R. Lu, X. Tang, and V. McCrary, "The state of the art and practice in digital preservation," J. Res. Natl. Inst. Stand. Technol. **107**, 93 (2002).

132. D. Eigler and E. Schweizer, "Positioning single atoms with a scanning tunnelling microscope," Nature **344**, 524–526 (1990).

133. G. E. Begtrup, W. Gannett, T. D. Yuzvinsky, V. H. Crespi, and A. Zettl, "Nanoscale Reversible Mass Transport for Archival Memory," Nano Lett. **9**, 1835–1838 (2009).

134. M. Irie and Y. Okino, "Statistical Analysis of Lifetime Distribution for Optical Recordable Disks," Jpn. J. Appl. Phys. **45**, 1460–1462 (2006).

135. O. Slattery, R. Lu, J. Zheng, F. Byers, and X. Tang, "Stability Comparison of Recordable Optical Discs-A study of error rates in harsh conditions," J. Res. Natl. Inst. Stand. Technol. **109**, 517–524 (2004).

136. Z. Sun, J. Zhou, and R. Ahuja, "Unique Melting Behavior in Phase-Change Materials for Rewritable Data Storage," Phys. Rev. Lett. **98**, 55505 (2007).

137. Y. Shimotsuma, M. Sakakura, P. G. Kazansky, M. Beresna, J. Qiu, K. Miura, and K. Hirao, "Ultrafast Manipulation of Self-Assembled Form Birefringence in Glass," Adv. Mater. **22**, 4039–4043 (2010).

138. J. H. Strickler and W. W. Webb, "Three-dimensional optical data storage in refractive media by two-photon point excitation.," Opt. Lett. **16**, 1780–1782 (1991).

139. M. Watanabe and S. Juodkazis, "Transmission and photoluminescence images of three-dimensional memory in vitreous silica," Appl. Phys. Lett. **74**, 3957–3959 (1999).

140. J. Squier and M. Müller, "Third-harmonic generation imaging of laser-induced breakdown in glass," Appl. Opt. **38**, 5789–5794 (1999).

141. M. Shiozawa, T. Watanabe, E. Tatsu, M. Umeda, T. Mine, Y. Shimotsuma, M. Sakakura, M. Nakabayashi, K. Miura, and K. Watanabe, "Simultaneous multi-bit recording in fused silica for permanent storage," Jpn. J. Appl. Phys. **52**, 1–4 (2013).

142. T. Watanabe, M. Shiozawa, E. Tatsu, S. Kimura, M. Umeda, T. Mine, Y. Shimotsuma, M. Sakakura, M. Nakabayashi, K. Miura, and K. Watanabe, "A driveless read system for permanently recorded data in fused silica," Jpn. J. Appl. Phys. **52**, (2013).

143. M. Gecevičius, M. Beresna, J. Zhang, W. Yang, H. Takebe, and P. G. Kazansky, "Extraordinary anisotropy of ultrafast laser writing in glass.," Opt. Express **21**, 3959–68 (2013).

144. S. Lee, T. Kim, K. Kim, and J. Kim, "Lifetime Management of Flash-Based SSDs Using Recovery-Aware Dynamic Throttling," Fast, (2012).

145. N. Mielke, H. P. Belgal, A. Fazio, Q. Meng, and N. Righos, "Recovery effects in the distributed cycling of flash memories," in *IEEE International Reliability Physics Symposium Proceedings* (2006), 29–35., (2006).

146. A. R. Olson and D. J. Langlois, "Solid State Drives Data Reliability and Lifetime Floating Gate Flash Memory Cells," Imation White Pap. 1–27 (2008).

147. M-Disc, "Millenniata-M-Disc," <http://www.mdisc.com/>.

148. T. Watanabe, T. Shintani, K. Ono, and T. Mine, "A digital-data-preservation system featuring LED-light computer tomography," IEICE Electron. Express **6**, 1569–1575 (2009).

149. X. Yu, X. Rong, and X. Leng, "Lifetime of thermally fixed holograms and gratings in Zn:Fe:LiNbO3 crystals," Opt. - Int. J. Light Electron Opt. **126**, 784–787 (2015).

150. A. L. Lacaita, "Phase change memories: State-of-the-art, challenges and perspectives," Solid. State. Electron. **50**, 24–31 (2006).

151. S. Quabis, R. Dorn, M. Eberler, O. Glöckl, and G. Leuchs, "Focusing light to a tighter spot," Opt. Commun. **179**, 1–7 (2000).

152. H. Wang and F. Gan, "High focal depth with a pure-phase apodizer.," Appl. Opt. **40**, 5658–5662 (2001).

153. H. Ren, H. Lin, X. Li, and M. Gu, "Three-dimensional parallel recording with a Debye diffraction-limited and aberration-free volumetric multifocal array," Opt. Lett. **39**, 1621 (2014).

154. J. E. Curtis, B. A. Koss, and D. G. Grier, "Dynamic holographic optical tweezers," Opt. Commun. **207**, 169–175 (2002).

155. R. Wood, "Future hard disk drive systems," J. Magn. Magn. Mater. **321**, 555–561 (2009).

156. S. L. M. S. L. Min and E. H. N. E. H. Nam, "Current trends in flash memory technology," Asia South Pacific Conf. Des. Autom. 2006. (2006).

157. D. Sarid and B. H. Schechtman, "A Roadmap for Optical Data Storage Applications," Opt. Photon. News **18**, 32–37 (2007).

158. Y. Shiroishi, K. Fukuda, I. Tagawa, H. Iwasaki, S. Takenoiri, H. Tanaka, H. Mutoh, and N. Yoshikawa, "Future options for HDD storage," in *IEEE Transactions on Magnetics* (2009), Vol. 45, 3816–3822 (2009).

159. L. L. Erskine, A. a Heikal, S. M. Kuebler, M. Rumi, X. Wu, S. R. Marder, and J. W. Perry, "Two-photon polymerization initiators for three- dimensional optical data storage and microfabrication," Solid State Phys. **398**, 51–54 (1999).

160. M. Wuttig and N. Yamada, "Phase-change materials for rewriteable data storage.," Nat. Mater. **6**, 824–832 (2007).

161. K. Aoshima, N. Funabashi, K. Machida, Y. Miyamoto, K. Kuga, T. Ishibashi, N. Shimidzu, and F. Sato, "Submicron Magneto-Optical Spatial Light Modulation Device for Holographic Displays Driven by Spin-Polarized Electrons," Disp. Technol. J. **6**, 374–380 (2010).

162. S. V Marchese, C. R. E. Baer, a G. Engqvist, S. Hashimoto, D. J. H. C. Maas, M. Golling, T. Südmeyer, and U. Keller, "Femtosecond thin disk laser oscillator with pulse energy beyond the 10-microjoule level.," Opt. Express **16**, 6397–407 (2008).

163. F. Wang, "Utility transforms of optical fields employing deformable mirror," Opt. Lett. **36**, 4383 (2011).

164. M. Reicherter, T. Haist, E. U. Wagemann, and H. J. Tiziani, "Optical particle trapping with computer-generated holograms written on a liquid-crystal display.," Opt. Lett. **24**, 608–610 (1999).

165. J. a. Davis, D. M. Cottrell, J. Campos, M. J. Yzuel, and I. Moreno, "Encoding Amplitude Information onto Phase-Only Filters," Appl. Opt. **38**, 5004–5013 (1999).

166. T. Onuma and Y. Otani, "A development of two-dimensional birefringence distribution measurement system with a sampling rate of 1.3 MHz," Opt. Commun. **315**, 69–73 (2014).

167. E. Collett, "Measurement of the four Stokes polarization parameters with a single circular polarizer," Opt. Commun. **52**, 77–80 (1984).

168. B. D. Cameron, "Noninvasive birefringence compensated sensing polarimeter," U.S. Patent No. 7,245,952., (2007).